

AD-A058 364

WEIDLINGER ASSOCIATES NEW YORK
COMPARISON OF PRE-SHOT RESPONSE PREDICTIONS WITH AVCO REVERSE B--ETC(U)
NOV 77 J M MCCORMICK

F/G 19/4

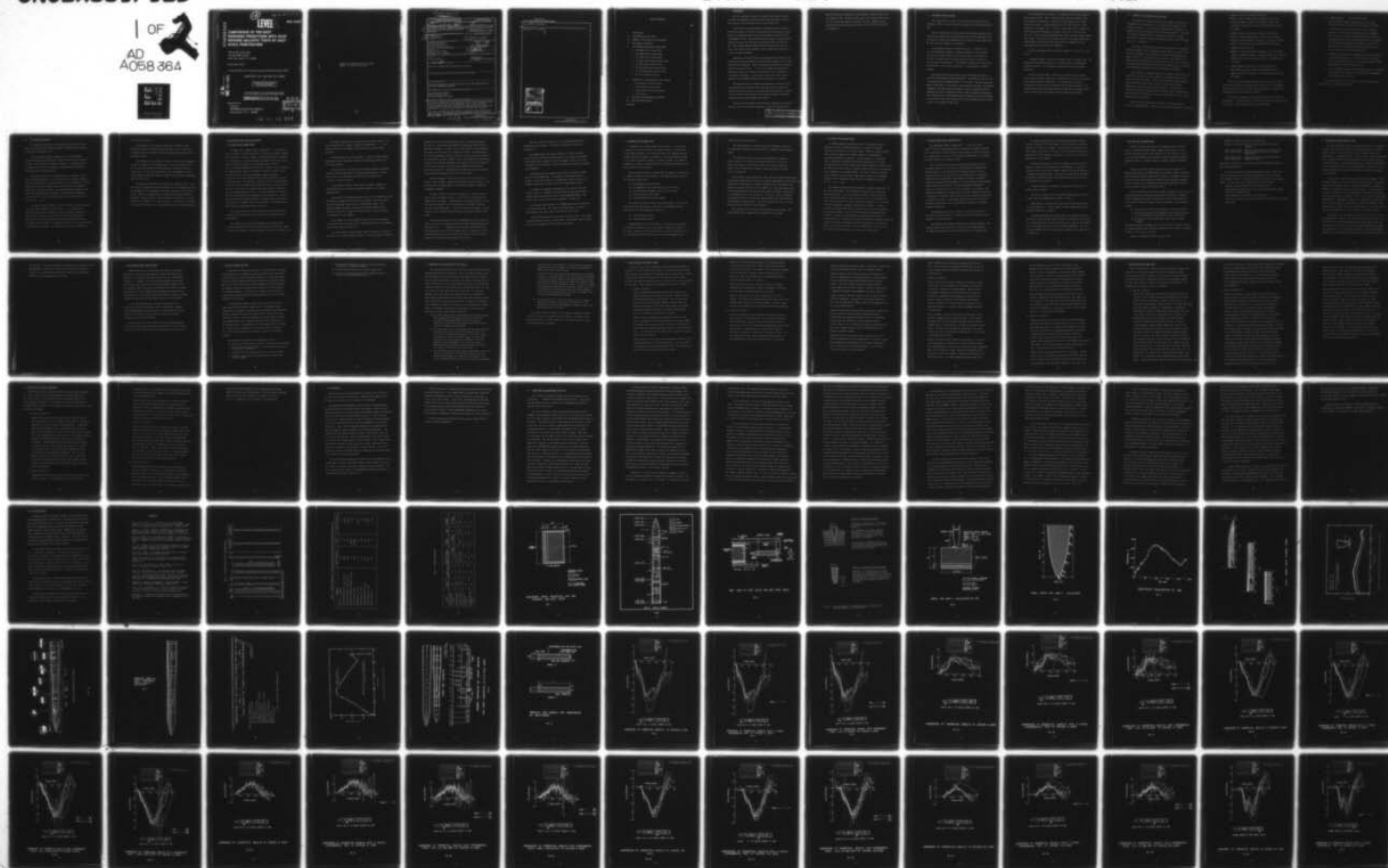
DNA001-76-C-0353

UNCLASSIFIED

DNA-4482T

NL

1 OF 2
AD
A058 364





ADA 058364

(12)

AD-E 300 303

LEVEL

DNA 4482T

**COMPARISON OF PRE-SHOT
RESPONSE PREDICTIONS WITH AVCO
REVERSE BALLISTIC TESTS OF HALF-
SCALE PENETRATORS**

Weidlinger Associates
110 East 59th Street
New York, New York 10022

November 1977

Topical Report for Period August 1976—November 1977

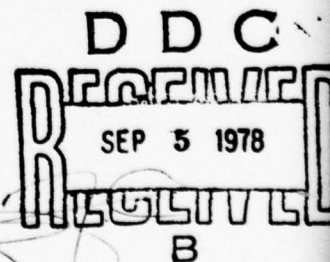
CONTRACT No. DNA 001-76-C-0353

APPROVED FOR PUBLIC RELEASE;
DISTRIBUTION UNLIMITED.

THIS WORK SPONSORED BY THE DEFENSE NUCLEAR AGENCY
UNDER RDT&E RMSS CODE B34407T464 Y99QAXSB04827 H2590D.

ORIGINAL CONTAINS COLOR PLATES: ALL DDC
REPRODUCTIONS WILL BE IN BLACK AND WHITE

Prepared for
Director
DEFENSE NUCLEAR AGENCY
Washington, D. C. 20305



78 07 18 011

ID No. _____
UDC FILE COPY

Destroy this report when it is no longer
needed. Do not return to sender.



(18) DNA, SBIE

UNCLASSIFIED

SECURITY CLASSIFICATION OF THIS PAGE (When Data Entered)

(19) REPORT DOCUMENTATION PAGE		READ INSTRUCTIONS BEFORE COMPLETING FORM
1. REPORT NUMBER	2. GOVT ACCESSION NO.	3. RECIPIENT'S CATALOG NUMBER
DNA 4482T 3 AD-E300 343		(9)
4. TITLE (and Subtitle)		5. TYPE OF REPORT & PERIOD COVERED
COMPARISON OF PRE-SHOT RESPONSE PREDICTIONS WITH AVCO REVERSE BALLISTIC TESTS OF HALF-SCALE PENETRATORS.		Topical Report for Period Aug 76-Nov 77
7. AUTHOR(s)		6. PERFORMING ORG. REPORT NUMBER
(10) J. M. McCormick		
9. PERFORMING ORGANIZATION NAME AND ADDRESS		8. CONTRACT OR GRANT NUMBER(s)
Weidlinger Associates 110 East 59th Street New York, New York 10022		DNA 001-76-C-0353
11. CONTROLLING OFFICE NAME AND ADDRESS		10. PROGRAM ELEMENT, PROJECT, TASK AREA & WORK UNIT NUMBERS
Director Defense Nuclear Agency Washington, D. C. 20305		(16) (17) Subtask Y99QAXSB048-27
14. MONITORING AGENCY NAME & ADDRESS (if different from Controlling Office)		12. REPORT DATE
(12) 132p.		November 1977
		13. NUMBER OF PAGES
		132
		15. SECURITY CLASS (of this report)
		UNCLASSIFIED
		15a. DECLASSIFICATION/DOWNGRADING SCHEDULE
16. DISTRIBUTION STATEMENT (of this Report)		
Approved for public release; distribution unlimited.		
17. DISTRIBUTION STATEMENT (of the abstract entered in Block 20, if different from Report)		
627044		
18. SUPPLEMENTARY NOTES		
This work sponsored by the Defense Nuclear Agency under RDT&E RMSS Code B34407T464 Y99QAXSB04827 H2590D.		
19. KEY WORDS (Continue on reverse side if necessary and identify by block number)		
Earth Penetrating Weapons Reverse Ballistic Tests Pre-shot Response Predictions		
20. ABSTRACT (Continue on reverse side if necessary and identify by block number)		
This report compares eight theoretical pre-shot predictions with the results of two reverse ballistic tests performed by AVCO in the late summer of 1976. The test setup and the tests are described. Each of the theoretical approaches (which used many different modeling techniques, from simple wave transmission to complex finite elements) is discussed and evaluated. The report concludes that the theoretical predictions were consistent and quite accurate. The agreement with the experimental results is generally		

DD FORM 1 JAN 73 1473 EDITION OF 1 NOV 65 IS OBSOLETE

UNCLASSIFIED

SECURITY CLASSIFICATION OF THIS PAGE (When Data Entered)

373 459
78

07 18 011

UNCLASSIFIED

SECURITY CLASSIFICATION OF THIS PAGE(When Data Entered)

20. ABSTRACT (Continued)

excellent whenever the latter results are sufficiently redundant and self-consistent to be credible.

A

ACCESSION for	
NTIS	Index Section <input checked="" type="checkbox"/>
DDC	Index Section <input type="checkbox"/>
UNANNOUNCED	<input type="checkbox"/>
JUSTIFICATION	
BY	
DISTRIBUTION/AVAILABILITY CODES	
Dist. AVAIL. and/or SPECIAL	
A	

UNCLASSIFIED

SECURITY CLASSIFICATION OF THIS PAGE(When Data Entered)

TABLE OF CONTENTS

	<u>Page</u>
I INTRODUCTION	3
II THE REVERSE BALLISTIC TESTS	5
III SUMMARY OF THE THEORETICAL CALCULATIONS	7
IV THE LOADING CALCULATION	10
V THE RESPONSE CALCULATIONS (PREDICTIONS)	12
1. The HONDO Finite Element Model	12
2. The NONSAP Finite Element Model	16
3. The DTVIS2 Finite Element Model	18
4. The SHELL SHOCK Lumped Parameter Model	19
5. The DAMS Lumped Parameter Model	21
6. The Thin Shell Modal Analysis Model	23
7. The Belytschko Modal Analysis Model	25
8. The Wave Transmission Model	26
VI COMPARISON OF CALCULATIONS WITH TEST RESULTS	28
1. Strain Gages on Outside Casing	30
2. Strain Gages on Inner Lining	35
3. Strain Gages on Internal Components	38
4. Accelerometers	41
VII CONCLUSIONS AND OBSERVATIONS (PRE-SHOT)	43
VIII POST-SHOT MODIFICATIONS	52
REFERENCES	53

I INTRODUCTION

This is a preliminary report on a Defense Nuclear Agency project to assess the capability of various calculational approaches to predict the results of reverse ballistic tests of earth penetrators.

In particular, seven investigators used eight different models to predict the results of two half scale penetrator reverse ballistic tests, which were performed by AVCO at Otis Air Force Base on August 26, 1976 and September 9, 1976. The predictions from the eight calculations were submitted to DNA by June 1976 and were available before the tests were run. This document compares these pre-shot predictions with the two sets of test results and an attempt is made to assess the usefulness of each of the eight approaches.

Experience with similar previous investigations has shown that the interaction between the penetrator response and the dynamics of the target material may be neglected. Thus the penetration problem may be uncoupled into two successive actions. In the first problem, the penetrator is regarded as rigid and the forces on the penetrator are calculated as it penetrates the target. In the second stage, these forces are then applied to the deformable penetrator and its response is determined.

CRT performed the first analysis and supplied the predicted loads on the penetrator to contractors who used these forces to predict the deformation of the penetrator, using eight different approaches ranging from very detailed finite element code calculations down to simplified estimates based on wave transmission principles.

These structural response predictions were completed and made available well before two half-scale penetrators, built and instrumented by

Sandia Laboratories, Albuquerque, were successfully tested by AVCO in the late summer of 1976. The body of this report first describes those tests, then the loading and response predictions, and then compares the predictions with the test results, and finally, puts forth some conclusions and suggestions.

II THE REVERSE BALLISTIC TESTS

The reverse ballistic tests of a half-scale earth penetrator were performed by AVCO at Otis Air Force Base on August 26, 1976 and September 9, 1976.

The tests consisted of firing a large block of Dakota sandstone from a gun in such a manner that the sandstone struck the earth penetrator (with zero angle of attack and no obliquity) with a velocity of about 1800 ft/sec. The two tests were intended to be identical.

Each sandstone projectile consisted (see Fig. 1, from Ref. [8]) of a 14 inch diameter cylinder of sandstone encased in a thin aluminum can having an outside diameter of 15.18 inches and a wall thickness of .09 inch. The gap between the sandstone and the can was filled with a Portland cement matching grout. Each sandstone cylinder was 9 inches long and rested on a 1 inch layer of sand and a 1.5 inch backplate of 6061-T6 aluminum.

The targets were half scale models of an earth penetrator which were built and instrumented by Sandia Laboratories. The models (see Fig. 2) were 32 inches long with a maximum diameter of 3.35 inches. The outer casing was made of 9-4-20 steel. The ballast in the nose was D 38 uranium. The internal components of the penetrator were modeled in 6061-T6 aluminum, TI-6AL-4V titanium, 4340 steel, and MICA-50 potting. These components were assembled into individual cans of 250 maraging steel and these cans were then connected to each other by steel bolting rings and the entire assembly was then locked in place by an aluminum closing ring.

The instrumentation consisted of 5 accelerometers and 36 strain gages on each penetrator model. Table 1 (from Ref. [8]) shows the location of each strain gage and accelerometer. There were 18 strain gages on the outside casing of the shell at various meridians (0° , 90° , 180° and 270°). These consisted of four gages at Sta. 4 (near the nose), eight at Sta. 9 (where the ballast ends and the component can begins), four at Sta. 19.5 and two at Sta. 27.3. Ten of these gages measured axial strain, the other eight recorded hoop strains. The other 18 strain gages consisted of ten gages (eight axial and two hoop) on the inside of the steel liner of the component can, and eight gages (all axial) on various components.

The five accelerometers were located at stations 7.2, 14.75, 19.5, 27.8, and 32.

A schematic drawing of test setup is shown in Fig. 3 (from Ref. [8]). The penetrator was suspended by two wires in front of the gun containing the sandstone projectile. The sandstone was then fired into the stationary projectile.

The tests were successful. There were 41 channels of data recorded from each test (36 strain gages and 5 accelerometers) and only 4 of the total of 82 channels failed to provide data. The measured media projectile velocities for the two tests were 1920 fps and 1770 fps respectively. The time histories from the tests were reported by AVCO and are included in this report only where they are compared with the theoretical predictions.

III SUMMARY OF THE THEORETICAL CALCULATIONS

The objective of the calculations was to predict the motion and deformation of the penetrator as it was impacted and engulfed by the sandstone projectile. This requires an approach which considers the dynamics of both the sandstone projectile and the penetrator. But since the interaction between these two systems was expected to be minor, the decision was made to uncouple the problem into two separate analyses (see Fig. 4 , from Ref. 1).

The first of these analyses treated the penetrator as a rigid body impacting normally upon the sandstone cylinder backed by a layer of sand and one of aluminum. The calculation, performed by CRT, employed the WAVE-L code, and is described in the next section. The loading on the penetrator was determined and the time histories of the radial and tangential loading were calculated and later made available to each of the seven contractors who participated in the second phase of the analysis.

This second set of analyses consisted of detailed calculations of the response of the penetrator, now assumed to be deformable, using the CRT force time histories as input. The seven investigators chosen performed eight calculations, which ranged from nearly back-of-the-envelope approaches to large code finite element solutions. The object was to determine what useful information could be derived from each approach and what was the cost (in terms of time, talent, possibility of error, computer charges) of that information.

Each of the eight approaches is reported in a separate section, but they are summarized here. There were four general purpose code calculations:

1. A HONDO calculation by Sandia Laboratories.

HONDO is a finite element computer program for the large deformation dynamic response of axisymmetric solids. The calculation reported here used about 2100 nodes (4200 degrees of freedom).

2. A DTVLS2 calculation by Lawrence Livermore Laboratories.

DTVLS2 is a general purpose finite element code for dynamic analysis of three dimensional structures. The results reported herein are from a model that used 870 nodes and 730 zones.

3. A NONSAP calculation by CRT.

NONSAP is a structural analysis program for static and dynamic response of nonlinear systems. The model used for the calculation reported herein used 160 elements, 500 nodes, and 1000 degrees of freedom.

4. A SHELL SHOCK calculation also by Sandia Laboratories.

SHELL SHOCK is a general purpose lumped parameter code for dynamic analysis of structures. The model used contained only 80 elements.

All of the four codes mentioned above are general finite element codes and are used for solving many types of structures. No development was done on these codes for this project; the penetrator was modeled, the loading adapted, and the codes were executed.

The other four approaches were devised specifically for penetrator applications. In some cases they are analyses developed for this particular set of tests. These four specialized calculations were:

1. A lumped parameter calculation by AVCO, which used a nonlinear, damped, lumped parameter axial system. The model consisted of 83 masses with 83 degrees of freedom.
2. A modal analysis based on a thin shell code by Weidlinger Associates. This analysis used modes generated by BOSOR4 (Ref. 2) which is a finite difference program for the stress, stability, and vibration of branched thin shells of revolution. The calculation used 30 modes from BOSOR4 to represent the outside casing of the penetrator and one spring and one mass to represent all the internal configuration.
3. A modal analysis based on an elementary model by the University of Illinois, Chicago Circle. The calculations were obtained from a linear superposition of the first eight modes of a model consisting of one rigid mass and two rods.
4. A wave propagation analysis by the Georgia Institute of Technology. This analysis used a solution for transmission of axisymmetric waves through conical sections.

A detailed analysis of each of these calculational approaches is given in later sections of this report.

IV THE LOADING CALCULATION

The analytical prediction of the loading on the penetrator due to impact and penetration into Dakota sandstone at 1800 ft/sec was provided by CRT and is described in Ref. 1.

This calculation utilized the WAVE-L code, a two-dimensional code which integrates the equations of motion for elastic-plastic bodies through a finite difference Lagrangian technique. A sliding interface, in conjunction with a friction model, was used between the rigid penetrator body and the sandstone media.

The target consisted of a layered cylinder, as indicated in Fig. 5. For the loading calculation, it was assumed that the sandstone extended to the outer free surface of the test assembly, i.e. to a diameter of 15.18 in. The details of the grout annulus and the can walls were not considered significant and were not modeled. The nominal properties assumed for the three target materials (Dakota sandstone, sand and 6061-T6 aluminum) are listed in Table 2. The constitutive models used for these materials are given in Ref. 1 and 6.

The assumed problem conditions for the calculation of the penetration test into Dakota sandstone are shown in Fig. 5. For calculational efficiency, the problem was conducted with the penetrator impacting an initially-at-rest target, rather than in the reverse ballistic mode. Only the nose section of the penetrator was specifically modeled since the contact area was limited to the nose during the portion of the penetration calculated in this solution. The periphery of the nose was represented

by 57 points (see Fig.6).

Time histories of the axial and radial forces applied to each penetrator point were recorded and made available to each of the seven contractors who used the eight calculational approaches described in the following sections.

These time histories presented the radial and axial force components on each line segment of the penetrator ogive. Plots were generated for the 37 nose points which were loaded during the calculation, which was carried out to a time of 465 microseconds. This corresponds to a penetration depth of 9.86 inches which is complete penetration of the sandstone layer by the nose tip.

The deceleration history of the penetrator is shown in Fig.7 . This plot gives the computed projectile deceleration for each computational cycle (no smoothing or time averaging has been done). There was a total of 1454 cycles. Based on a smoothed plot, the maximum deceleration was 6850 g's, reached at a time of 188 μ sec. The deceleration then decreases at a nearly uniform rate to 2900 g's, at a time of 414 μ sec. It then rose to 4100 g's at the end of the solution, as the penetrator neared the aluminum backplate.

V THE RESPONSE CALCULATIONS (PREDICTIONS)

1. THE HONDO FINITE ELEMENT MODEL

The HONDO finite element computer program (Ref. 4) was used by Peter P. Stirbis of Sandia Laboratories to determine the dynamic response of the penetrator to the CRT loading. The program, developed by Samuel W. Key, is designed to calculate the large deformation elastic and inelastic transient dynamic response of two dimensional solids and employs a four noded isoparametric quadrilateral element. The accelerations are computed at the nodes of each element, and then by using a central difference operator, they are integrated to obtain velocities at the nodes. The code continuously monitors the step size to keep the calculation stable. The gradients of the velocities are then determined at the center of each element which provide the rates of stretching and rotation. Stress rates are computed using the constitutive equations and then integrated forward in time. The stress components are used to find new accelerations at the beginning of the next time step. The program contains eight material subroutines covering elastic, viscoelastic, elastic-plastic, crushable foam, and soil behavior. The program accepts normal pressure loadings and initial velocities.

The initial velocity for this problem was zero, and pressures as a function of time were applied to various elements along the ogive of the penetrator.

The response of the model was determined for 500 microseconds. The problem used 2700 time steps and 7900 seconds on the CDC 6600 computer. The complete development of the model required 17.5 hours of computer time.

The finite element model of the penetrator is shown in Fig. 8. The mesh was generated by a computer program called QMESH (Ref. 5). The model consisted of 1559 elements, 2097 nodal points, and 9 different materials.

In designing the finite element model, a tradeoff was made between maximizing accuracy (many small elements) and minimizing computer time (few large elements).

In the outer case (.45 thick), three elements through the thickness were used, which was sufficient to describe bending response. A square aspect ratio is also desirable, which resulted in elements about .15 inch x .15 inch in the case.

In the support structure (.075 thick), one element through the thickness was used since membrane response was judged to be of primary importance here.

There was an air gap modeled between the case and the support structure and between the support structure and the components. This was to allow relative displacements which will occur during normal impact. The interface between the ballast and the outer case was assumed to be in contact and not slide or separate because the ballast and the case have an interference fit at assembly.

Four elements were used through the radius of the solid components. This was done to provide some detail in modeling the passive accelerometers and the steel slugs at Station 19.5.

The single degree of freedom (SDF) systems at Station 12 and Station 26 consist of a cylindrical mass (.306 lb), a .375 inch diameter x .500 inch

long post, two .25 inch thick end plates, and a .2 inch thick cylinder (see Fig. 2). Both systems were modeled as homogeneous solids with the appropriate densities to result in the correct weight for these components. The purpose for doing this was to simplify the model. The justification was that the longitudinal natural frequency of the mass and post oscillator was calculated to be about 15,000 Hz. This is much higher than the natural frequency of the SDF system mounted to the support structure at Station 12 or the natural frequency of the SDF system supported by the potting material at Station 26. This means that the SDF oscillators will respond as rigid bodies with respect to the rest of the system.

The two rectangular steel slugs at Station 19.5 were modeled as a single circular cylinder, symmetric about the axis of the penetrator. This was done since the normal impact of the penetrator produces essentially axisymmetric responses.

The short cylinder at Station 31.25 applies the 1000 lb preload to the aft end of the support structure. The cylinder is compressed about .00004 inches at assembly. (During impact, the preload decreases to zero, and a gap is developed.) Due to this action, the cylinder is omitted from the finite element model. If it were retained in the model, it would develop a tensile load which would produce an unrealistic response of the system.

The material properties used in the HONDO model are those listed in Table 3. The static and dynamic properties of MICA-50 potting compound are described in Ref. 6. Although the yield strength does increase with increasing strain rate, the yield strength value of 17,900 psi used in the calculation was above the stress actually developed in the model, and the response of the potting was essentially linear elastic.

(The slots, grooves, cutouts, etc., in the potting material and components were not modeled. The system was assumed to be perfectly axisymmetric.)

Since HONDO accepts only normal pressures, the axial and radial forces provided by CRT were resolved normal to the surface of the element and the pressure was computed for each line segment, based on the R and Z coordinate of its end points. The shear stress on the element was assumed to be negligible.

In addition, the line segments used by CRT did not match the mesh size used in the HONDO model. A matching of corresponding elements was done to obtain the loading on the HONDO model, which resulted in 22 elements being loaded for the 4.5 inch axial length along the ogive.

A straight line segmented approximation to the CRT plot was used as shown in Fig. 9. Although a force data computer tape was available, a manual digitizing process was quicker than programming HONDO to read the data tape, particularly due to the mismatch in element size.

Each element along the ogive of the HONDO model was then loaded with a time varying pressure. The pressure loading was made to "arrive" at each element at the proper time, as dictated by the CRT data.

The CRT loading prediction was used to 465 microseconds. The loading was then assumed to unload in an additional 5 microseconds, and then remain at zero for the remainder of the response calculations.

2. THE NONSAP FINITE ELEMENT MODEL

The NONSAP finite element computer program (Ref. 3) was used by Y. Marvin Ito of CRT to determine the dynamic response of the penetrator to the loading developed by his own organization. The program, developed by Bathe, Wilson, and Iding, is intended as a structural analysis program for the static and dynamic response of nonlinear systems. The program is designed for a general incremental solution of nonlinear problems, but can also be used for linear analysis.

The structural systems to be analyzed may be composed of combinations of a number of different finite elements. The program presently contains the following element types:

- (a) three-dimensional truss element
- (b) two-dimensional plane stress and plane strain element
- (c) two-dimensional axisymmetric shell or solid element
- (d) three-dimensional solid element
- (e) three-dimensional thick shell element

The nonlinearities may be due to large displacements, large strains, and nonlinear material behavior. The material descriptions presently available for the three-dimensional elements are:

- (a) isotropic linear elastic
- (b) curve description model

Program NONSAP has an in-core solver. The capacity of the program is essentially determined by the total number of degrees of freedom in the system. However, all structure matrices are stored in compacted form, i.e. only nonzero elements are processed, resulting in maximum system

capacity and solution efficiency.

The system response is calculated using an incremental solution of the equations of equilibrium with the Wilson θ or Newmark time integration scheme.

The incremental solution scheme used corresponds to a modified Newton iteration. To increase the solution efficiency, the user can specify an interval of time steps in which a new effective stiffness matrix is to be formed and an interval in which equilibrium iterations are to be carried out.

The CRT results (both nonlinear and linear material response analyses were performed for comparison) were based on a detailed (isoparametric) finite (Fig. 10) element model (1100 degrees of freedom) representation of the one-half scale penetrator using the CRT version of the NONSAP code. The nodal spacing along the nose exactly matched the lattice spacing used in the Phase I calculation for the applied forces on the penetrator. In order to filter out numerical oscillations, the force histories were smoothed before input and the Wilson time integration scheme was used. The cutoff frequency for the 2 μ sec time step used in the analyses was about 60,000 Hz.

CRT found that only the uranium yielded during the calculations. The high strength steels remained elastic throughout the calculation.

3. THE DTVIS2 FINITE ELEMENT MODEL

The DTVIS2 computer program was used by its developer, Gerald L. Goudreau of Lawrence Livermore Laboratories, to predict the dynamic response of the penetrator to the CRT loading. DTRIS2 is a general purpose finite element program for the dynamic response of two-dimensional (including axisymmetric) structures. The main element is a four-noded linear isoparametric quadrilateral (which may degenerate to a triangle, if needed), but the code also allows certain other elements (not used for this penetrator model) such as a thin-shell element which uses a Grafton-Stong cubic polynomial in an uncommon fashion. The material model is nonlinear elastic isotropic so only plastic loading may be modeled - not unloading. An implicit time integration scheme, based on the Newmark beta method ($\beta = \frac{1}{4}$, $\gamma = \frac{1}{2}$), is used.

Two models were investigated using DTVIS2. Each had roughly (Fig. 11) 730 zones and 870 nodes. The two models were classified as interacting and non-interacting. In the non-interacting model the space between the outside casing and internal can was taken as a void. In the interacting model, this space was filled with a selastic-like material, i.e. a material with great compressive strength and minimal shear strength. In those sections of the model where there is no taper, the only effect transmitted by the selastic zones is one of differential Poisson expansion, but where the model is tapered, the selastic zones transmit bearing between the casing and the can. The mesh used for these two models was designed so that the forward nose points correspond to the CRT loading points on a one-to-one basis, but the grid in the aft of the nose became coarser so that each two CRT loading points corresponded to one node on the DTVIS2 model.

4. THE SHELL SHOCK LUMPED PARAMETER MODEL

The SHELL SHOCK computer program (Ref. 7) was also used by Peter P. Stirbis of Sandia Laboratories, to determine the dynamic response of the penetrator to the CRT loading. This was done to compare the results of a simpler model to those of the more detailed HONDO model. The loading for SHELL SHOCK was also simpler to input.

This code performs a frequency analysis and determines the static and dynamic response of any structure represented by mass, damping, and stiffness matrices. The matrices may be formed directly by the user, formed internally by the code from a finite element model, or formed by a combination of the two methods. SHELL SHOCK is primarily intended for analyzing three-dimensional axisymmetric structures modeled using structural elements generated by the code. The three-dimensional axisymmetric structure is reduced, by the use of Fourier harmonics, to a series of two-dimensional problems, which significantly reduces the computations required, if few modes are required. Three types of structural elements are generated internally by the code: linear beams, shells, and solids of revolution. Non-linear beam elements are also available and included in the dynamic response calculations.

The program accepts forces, pressures, and initial velocities as a function of time and location. A single axial force was applied to this problem as a function of time.

The response of the model was determined for 500 microseconds. The problem used 285 time steps and 114 seconds on the CDC 6600 computer. The complete development of the model required 1 hour of computer time.

The lumped parameter model of the penetrator is shown in Fig.12. The model consisted of 55 shell elements, 12 solid elements, and 6 beam elements for a total of 73 elements. The outer case was modeled with 31 shell elements, each about 1 inch long. The inner support structure was modeled with 17 shell elements, each about 1 inch long. The ballast was modeled with 3 solid elements.

The model was designed to allow the component support structure to displace relative to the penetrator case during impact. The preload cylinder of the aft end of the component support structure was modeled as a compression-only beam element. This allows a gap to open during impact, and develop a compressive load during rebound when the load on the nose of the penetrator is released.

The SDF oscillators are modeled as a beam and a mass tied to the hollow circular cylinder.

The material properties used in the SHELL SHOCK model are the same as those used in the HONDO model and shown in Table 3.

SHELL SHOCK is a linear elastic code and will not handle inelastic or large deformations. In some loading situations, SHELL SHOCK may not accurately describe the responses.

The SHELL SHOCK model was loaded simply. The rigid body penetrator deceleration versus time plot shown in Fig.13 was multiplied by the weight of the penetrator (48.5 lb in the CRT calculation). This was then applied, as a time varying force, to the nose of the SHELL SHOCK model. The force curve was represented with nine straight line segments and a maximum force of 330,000 lb.

5. THE DAMS LUMPED PARAMETER MODEL

The model developed and utilized by D. Henderson and R.D. Pepe of Avco is a non-linear, damped, lumped parameter axial system. It is an explicit code which features short running (~ 15 min.) and direct access to all structural members thereby permitting rapid evaluation of modeling assumptions such as: loadpaths, damping, coupling, loading environments, etc.

The basic structural dynamics model used by Avco to generate the impact response data is the DAMS computer code (Dynamic Analysis of Missile Structures) which underwent significant alteration to encompass the special needs of this particular problem. The DAMS code was originally configured to solve a linear set of simultaneous second order differential equations with an arbitrary forcing function time history.

For this problem the utilization of DAMS was changed to permit the use of nonlinear structural stiffness and damping matrices in order to represent several phenomena which could be important for accurate representation of the P2 vehicle under severe impact loading environments. These phenomena include:

- (1) Nonlinear stress/ strain relationships of structural material.
- (2) Nonlinear load paths of both components and secondary structure (e.g. coupling between inner and outer shell at the taper).
- (3) Uncoupling of the pre-loads when pre-load levels have been exceeded.

The stress/strain relationships used for this study are tri-linear in form. The lumped parameter model developed to represent the P2 vehicle is presented in Fig. 14. Referring to the figure:

Elements 1 through 23 represent the outer shell.

Elements 24 through 36 represent the inner shell.

Elements 37 through 83 represent the potting material and inner components.

3/37, 5/38, 7/39 and 14/28, 15/29, 16/30 represent coupling between the ballast/outer shell and inner/outer shell at the taper, respectively.

43/46, 46/48, 51/53, 66/64, 66/68, 70/71 represent initial preload coupling between component sections.

This model was subjected to the simulated loading environment provided by CRT and described earlier.

In all, the code was exercised approximately 30 times. Some of the runs were associated with the usual code development process, but most were conducted in order to investigate possible variations in the modeling itself. Of this latter type, there were runs which considered:

Complete uncoupling between the inner and outer shell.

uncoupling of the ballast to the outer shell except through elements 3/37- (i.e. through the nose).

Total "Slaving" of the ballast to the outer shell.

Slaving of the inner shell to the outer shell in the vicinity of the taper.

No pre-load.

6. THE THIN SHELL MODAL ANALYSIS MODEL

The model developed and used by Weidlinger Associates (J. McCormick) consists of two parts: the outside casing was represented by a certain number of modes from thin shell theory and the inside structure was represented by a spring-mass system. The main purpose of this investigation was to determine how much useful information could be obtained from such an elementary model. Secondary objectives were to develop an approach that could be extended directly to the non-normal impact cases and to use the loading information as supplied by CRT without intermediate calculations or curve-fitting.

The modes of the outside casing were obtained from BOSOR4, a finite difference program for the stress, stability and vibrations of segmented, ring-stiffened, branched shells of revolution developed by D. Bushnell of Lockheed. The program is based on thin shell theory. The program finds the modes of vibration for any circumferential wave number, so once the data is prepared for the axisymmetric case, it is trivial to find the modes required for the non-symmetric analysis. The program has an input option which allows the input of a general shell of arbitrary thickness. This option was used to model the nose of the penetrator. The after body of the penetrator was modeled as cones and cylinders of constant thickness.

The spacing of the nose points was chosen so that the CRT load tape was used directly. The force data from the CRT tape was copied to a file and this file was used without modification or enhancement (except for one obviously out-of-range) as input to the program MEGAN which computed the time histories of the generalized coordinates using the BOSOR4 modes combined with a spring-mass system representing the internal structure of

the penetrator. These time histories were subsequently processed by a program RESPON to calculate the strain and accelerations at any desired locations. Only minor modifications will be required to use MEGAN and RESPON for the non-axisymmetric calculations.

7. THE BELYTSCHKO MODAL ANALYSIS MODELS

A modal analysis of two simple models was used by T. Belytschko (University of Illinois, Chicago Circle) to predict the motion of the penetrator. The two models are shown in Fig.15 and are called Model 2 and Model 3. In Model 2, the two rods which represent the outer and inner cases are not connected at the back end, whereas in Model 3 they are connected. Model 3 was used for the pretest calculations. The first eight modes of each of the models were determined and the motions were calculated from a linear, modal superposition analysis, using as a forcing function the total CRT force time history, applied to the rigid mass.

It was mentioned above that the results using Model 3 were submitted as the pretest predictions and are reported here. However, Belytschko subsequently observed (see Ref. 12 and Section VIII of this report) that the results from his Model 2 agreed better with the experiments than did those of Model 3.

While plotting his results against the tests, Belytschko found he had to shift the starting times of the test results by 150 μ sec for Test 1 and 80 μ sec for Test 2 (See discussion of starting times in Section VI.).

8. THE WAVE TRANSMISSION MODEL

A traveling wave analysis was used by L.W. Rehfield and S.V. Hanagud (Georgia Institute of Technology) to predict the motion of the penetrator. Their objective was to retain the basic simplicity of a beam-like model, thereby providing economical predictions suitable for preliminary design, and then to correct these predictions by superposition of other solutions that might be needed for accurate stress estimation in critical regions of stiffness transition. The intent was to account for such effects as radial motion and Poisson expansion mismatches which result in localized bending of the shell wall.

The investigators sought to present their results in the form of simple equations which would be highly useful in preliminary design. Consequently, they modeled the penetrator as bar segments that transmitted primarily longitudinal stress waves and then later corrected for three-dimensional effects. They then attempted to track the various reflected and transmitted waves for a complete reflection of the primary wave in the penetrator body. An important step in their approach was the finding of a solution for the propagation of an arbitrary pulse in a tapered bar. This solution served as the keystone of their wave transmission approach.

The Georgia Tech approach may be summarized as follows:

- a) represent the penetrator as a series of interconnected bar elements.
- b) assume that the primary response is a plane uniaxial stress wave in any typical bar element.
- c) determine input wave characteristics for a given bar element.
- d) calculate transmitted wave characteristics as output from a given bar element.

- e) determine wave transmission and reflection characteristics at boundaries of dissimilar elements.
- f) perform sequential analysis for desired elapsed time.
- g) correct the plane wave predictions by approximate means to account for three-dimensional effects.

VI COMPARISON OF CALCULATIONS WITH TEST RESULTS

The test results from the reverse ballistic tests were satisfactorily redundant and usually self-consistent. There were almost always at least two experimental results (because only a few channels failed to deliver data) for each station where calculations were made because there were two nearly identical tests, but at many stations there were four experimental results (0° and 180° for each test) and at some locations there were eight test results (0° , 90° , 180° , and 270° for each test). For the most redundant cases, then, there were sixteen results to be compared for a given strain, eight theoretical calculations and eight experimental results. Since the curves do oscillate (rather wildly at times), it was thought to be impractical to show all the curves for a given location on a single figure. Accordingly, three figures are presented for most locations.

These figures contain the following information:

- (1) the first figure for each strain gage location contains as many of the eight theoretical calculations as were reported by June 1976, several months before the tests took place. A different key is used for each calculation and these keys are invariant throughout the presentation.
- (2) the second figure for each strain gage location shows exactly the same theoretical curves as the first figure, but one "best" test result is included for comparison. All the test results are plotted on the third and fourth figures for each strain gage location but these figures are sometimes a little too crowded for easy comparisons so one of the test results is arbitrarily chosen (as being fairly representative of all the test results) and plotted on the second figure.
- (3) the third figure for each strain gage location shows all the test results at 0° and 180° for both tests (as many as four test results) plotted against the theoretical calculations. The first test (August) plotted in red and the second test (September)

plotted in blue. The results at 0° are plotted as solid curves while those for 180° are dashed. The curves are discontinued whenever they begin to go off-scale.

The starting time of the theoretical calculations was the instant of impact. The starting times of the test results were estimated by AVCO and are shown in Table 1, but results plotted using these starting times sometimes had initial significant signals at times very different from the theoretical results. In such cases (where the experimental results had the same initial shape as the calculated results but a different starting time), the experimental curves have been shifted along the time axis so the times of the initial signals approximately coincide.

- (4) the fourth figure for a given strain gage location is present whenever test results are available for 90° and 270° . The presentation of plots on these figures is similar to that of the third figures (for 0° and 180°).

Each figure includes a diagram of the penetrator showing the location of the strain gage or accelerometer being considered. The radius to the gage and a description of the location, e.g. "on outside surface of case", are indicated below each diagram.

1. STRAIN GAGES ON THE OUTSIDE CASING

These were seven strain calculation items (axial and hoop strains at locations 4, 9, and 19.5; only axial strains at location 27.3) on the outside steel casing of the penetrator to be compared with a possible 36 test results (0° , 90° , 180° , and 270° at Station 9; 0° and 180° at the other three stations; axial and hoop strains, except at location 27.3, at each orientation for each test). These comparisons are presented in the next 23 figures:

a) Strains at Station 4

Figures 16-18 present the results for the axial strain on the outside casing just four inches from the nose. Figure 16 shows the theoretical results at this location. All six calculators reporting find the same general response, a single compressive pulse with a duration of about half a millisecond. The maximum millistrains predicted are about 2.3 by SLA/S, SLA/H and WA; about 2.7 by CRT and LLL; and about 3.5 by AVCO.

Figure 17 shows a representative experimental result, 0° from Test 2, superposed on the theoretical results. The gage, being on the outside of the casing and close to the nose, is destroyed by debris from the enveloping sandstone projectile shortly before 300 μ sec. Up to that time the test result agrees well with the general trend of the calculations.

Figure 18 shows all four axial strain experimental results at this station superposed on the theoretical results. The test results are reasonably self-consistent and agree well with the predictions until all four gages are destroyed by the target.

Figures 19-21 present the hoop strains at this forward location on the nose of the penetrator. Figure 19 shows the theoretical results at this location. Once again, all six calculators reporting find the same general response, a single tensile pulse with a duration of about half a millisecond. The maximum millistrains predicted vary from about .9 to about 1.1.

Figure 20 shows the 0° result from Test 1 (chosen as typical) superposed on the predictions. Again, the agreement is excellent until the gage is destroyed shortly after 200 μ sec.

Figure 21 shows all the test results superposed on the calculations. No result was recorded from the gage at 180° in Test 1 and the 180° result from Test 2 is clearly suspect. The two 0° gages agree with one another and the calculators until they are destroyed.

b) Strains at Station 9

Figures 22-25 present the axial strains on the outside casing at a point just aft of the location where the nose ballast ends and the inner liner begins. Figure 22 shows the theoretical results at this location. Most of the calculators reporting again find the same general shape, a compressive pulse of about 400 μ sec duration followed by a much smaller tensile pulse of perhaps 100 μ sec. The peak compressive strains cluster around millistrain values of 2. The maximum tensile strains have values of about .5 millistrain.

Figure 23 shows that the typical result, 0° from Test 2, agrees very well with the predictions until after the compressive peak.

Figure 24 shows the axial strain results for both tests, for 0° and 180° , superposed on the calculated results. The test results are less consistent among themselves than are the calculated results. The Test 1 results show more oscillation and much longer signals than the Test 2 results. The Test 1 results show a significant departure from axisymmetry after about 250 μsec .

Figure 25 shows the same test results as Fig. 24, but for the 90° and 270° orientations. Once again the test results agree very well with the predictions as long as they are self-consistent, up to a time of about 250 μsec .

Figures 26-29 show the hoop strains at this location. Again, most of the calculators reporting find the same general shape, a tensile pulse with maximum millistrain of about .5 and duration of about 400 μsec , followed by a brief compressive phase.

A Test 2 result, at 0° , is chosen as the typical result and Fig. 27 shows that it agrees very well with the calculations until it begins to oscillate strongly.

Figure 28 shows the hoop strain results for both tests, for 0° and 180° , superposed on the calculated results. The Test 1 results show stronger early oscillations, but the overall impression of the test results is that they would average to a value fairly close to the average of the calculations.

Figure 29 shows the same results for orientations of 90° and 270° . The oscillations are stronger than those shown on Fig. 28, but the general trend is discernible and follows the consensus of the predictions.

c) Strains at Station 19.5

Figures 30-32 present the axial strains on the outside casing at a point just aft of the middle of the penetrator, a point where the section is flaring to a larger diameter. Figure 30 shows the remarkable agreement in the predictions of the seven contractors of a compressive pulse averaging 16 millistrain and 300 μ sec duration followed by a much smaller tensile phase. The Test 2 result at 0° is shown in Fig. 31 as typical of the experimental results. It is seen to agree remarkably well with the predictions.

Figure 32 shows the axial strain results for both tests, for 0° and 180° , superposed on the calculated results. The 0° results from both tests are very consistent and agree very well with the average values of the calculators. The 180° test results are less useful. The Test 2 result at 180° has extreme early oscillation and goes off scale around 300 μ sec, while the Test 1 result at 180° is unreliable from the start.

Figures 33-35 show the hoop strains at this location. Four of the calculators agree on a prediction of a 300 μ sec duration tensile pulse averaging about .4 millistrain, followed by a short compressive phase, but LLL predicts a longer, stronger all-compressive pulse. This result is directly traceable to the model used by LLL for the results shown here. That model assumed interaction between the

outside casing and the inner liner at this point, It was mentioned earlier that LLL calculated with several models in addition to the one reported here. One of those models assumed no interaction, i.e. that the air gap between the casing and the liner never closed, and the results from that model are quite similar to those of the majority of calculators at this point. Once again Test 2 at 0° is chosen as the typical test result (Fig. 34). Its correlation with the calculations is excellent. Figure 35 shows the hoop strain results for both tests, for 0° and 180° , superposed on the calculated results. Once again, the test results at 0° are much more consistent and agree better with the calculations. The 180° results show the same behavior as did their axial counterparts: Test 2 goes off scale at about 300 μsec and Test 1 is suspect from the beginning.

d) Strains at Station 27.3

Figures 36-38 present the axial strains on the outside casing at this point near the tail of the penetrator, close to the station where the single degree of freedom internal component is located. The seven calculators are in reasonable agreement in predicting a compressive pulse of about 200 μsec duration followed by a smaller, shorter tensile phase, but their predictions of the maximum strain values and the nature of the intermediate oscillations vary widely. The 0° result from Test 1 has the longest duration and it is plotted in Fig. 37 as the typical result.

Figure 38 shows the experimental results for this gage. The 180° gage for Test 1 is suspect from the start but the other three test results (despite large pre-arrival time oscillations) agree with the predictions on the approximate magnitude of the first pulse.

2. STRAIN GAGES ON THE INNER LINER

There were three strain calculation items on the inside surface of the steel liner or can which contained the internal components. These three predictions (axial strains at stations 9 and 19.5, and hoop strains at station 19.5) may be compared with a possible 16 experimental results (0° , 90° , 180° and 270° at station 9; 0° and 180° at station 19.5). The comparisons are presented in the next 11 figures.

a) Strains at Station 9

Figures 39-42 present the axial strains on the inside surface of the steel liner at a point very near the forward end of the liner. Figure 39 shows the theoretical results at this location. The calculators reporting agree, except for UICC, on a single compressive phase but disagree strongly on its magnitude or its duration. UICC predicts a successor tensile phase and AVCO agrees with UICC on the shape of most of the compressive phase. These are the approaches which use the fewest degrees of freedom of those calculators reporting results for this location. The next coarsest approach, SLA/S with SHELL SHOCK, turns up next while the three detailed finite element calculations, SLA/H, LLL, and CRT, seem to indicate the longer and stronger compressive phases. Test 2, 0° , chosen as the typical result, is plotted in Fig. 40. The experiment agrees well with the consensus of the more detailed codes, and particularly well with SLA/H. The results for 0° and 180° are given in Fig. 41. The test results are fairly consistent and they all agree with the predictions for early times. But, for longer times it is evident that the detailed finite element codes (SLA/H, LLL, and CRT) give better predictions than do the coarser models. Figure 42 shows the results for 90° and 270° at this station, and

the results are even more consistent than those reported for 0° and 180° . In fact, all eight gages at this location are reasonably consistent and redundant which indicates that the two tests were indeed nearly identical and axisymmetric. The inconsistent experimental results noted at other gage locations seem to have been due to local recording inaccuracies rather than an overall weakness in the tests themselves.

b) Strains at Station 19.5

Figures 43-45 present the axial strains on the inside surface of the steel liner at a point just beyond the middle of the penetrator. Both the outer casing and the inner liner are flaring to larger diameters at this location and it is here that the assumption of non-interaction of the liner with the outside casing becomes critical. Figure 43 shows that the calculators all predict a single compressive phase but they disagree widely on its duration and the maximum strain values. The pattern of the results is similar to that detected in the analysis of the strains in the liner at station 9. Once again, the more detailed codes predict the longer and stronger signals but there are two major variations to this theme. First, SLA/S predicts a slightly stronger signal than SLA/H and second, the LLL model reported here (which assumes liner-casing interaction) predicts a weaker signal than the models which assume no interaction (SLA/S, SLA/H, CRT and LLL's non-interaction model). See the previous discussion of the hoop strain in the outer casing at this station. The 180° curve from Test 1 is plotted as the typical axial strain curve in Fig. 44. It is seen to agree well with both SLA calculations and with CRT. Again, the LLL model reported here assumed liner-casing interaction. The LLL results which assumed no interaction agree better with these test results.

Figure 45 presents all of the experimental axial strains at this mid-point station. Once again the test results are remarkably consistent and redundant, showing that the tests were identical and axisymmetric. The test results agree well with the predictions and, once again, the correlation is better with the more detailed finite element codes than it is with the coarser models.

Figures 46-48 present the hoop strains on the inside surface of the liner at this station and the effect of the interaction assumption manifests itself again. The four models which assume no interaction all predict a single long tensile phase while LLL, which assumes liner-casing interaction, predicts major compressive strain. The non-interaction LLL model predicts a signal similar to the other four predictions for this gage. The 180° result from Test 2 is taken as the typical result and it is plotted in Fig. 47. Once again the good agreement between this result and the SLA HONDO calculation should be noted. Figure 48 shows the four test results and once again they are reasonably consistent and their average agrees very well with the average of the predictions (except for the LLL results shown - the interaction assumption again. See Fig. 64 to see how the opposite assumption brings the LLL results into agreement with both the tests and other predictors).

3. STRAIN GAGES ON INTERNAL COMPONENTS

There were four strain calculation items on various internal components, one on the column of each SDF (single-degree-of-freedom) system, one on the outside surface of the potting, and one on the inside surface of the steel cylinder at station 27.3. Calculations at these four locations may be compared with a possible 16 test results (0° and 180° from each test at each of the four locations).

a) Strains at Station 12

Figures 49-51 present the axial strains on the column of the SDF system located at station 12. Figure 49 shows that four calculators reporting all predict a similar three phase motion: a compressive pulse with an amplitude of about 1 millistrain and a duration of about 250 μ sec, followed by a shorter, weaker tensile pulse, followed by a second compressive pulse which three of the calculators predicted would give the maximum strain in the signal, a value around 1.4 millistrain. The good agreement between prediction and experiment is evident in Fig. 50, where the 180° curve from Test 1 is shown as the typical result. This result agrees remarkably well with the predictions in both phasing and magnitude. All of the test results at station 12 are shown in Fig. 51. The 0° result from Test 1 quickly went off scale but all four results showed a pattern similar to the predictions and the other three results agreed well with the predictions.

b) Strains at Station 16

Figures 52-54 present the axial strains on the outside surface of the potting at station 16. The predictions of the six calculators

are shown in Fig. 52. The weakest pulse is predicted by LLL, again a direct consequence of the assumption of liner-casing interaction in the model reported here.

Figure 53, where the 0° result from Test 1 is plotted as typical, illustrates the good agreement between the experiment and the predictions. The fine agreement with the NONSAP calculation, by CRT, deserves special mention. All the test results at station 16 are presented in Fig. 54. Once again all four test results are reasonably consistent and agree well with the predictions.

c) Strains at Station 26.7

Figures 55-57 present the axial strains on the column of the SDF system at station 26.7. The four theoretical predictions are shown in Fig. 55. They agree on a single compressive pulse with a half period of about 400 μ sec. The three large finite element codes (LLL, SLA/S, and CRT) all agree rather closely, with AVCO predicting slightly higher strains. The experimental results are shown in Fig. 57. Only Test 1 results seem consistent and the 180° result is plotted in Fig. 56 as the typical result. It agrees remarkably well with the three finite element code results. The 0° result from Test 1 agrees better with the AVCO calculation.

d) Strains at Station 27.3

Figures 58-60 present the axial strains on the inside surface of the steel cylinder at station 27.3. The theoretical predictions are shown in Fig. 58. All four predictions show a single compressive pulse of half-period 400 μ sec, but the predicted maximum strains vary widely. The experimental results are plotted in Fig. 60 and they are seen to be quite hashy. This station is quite far back

on the vehicle and the gages seem to be shaking appreciably long before the initial signal should arrive. The most reliable test result seems to be 0° from Test 1 and that is plotted as typical in Fig. 59. It agrees very well with three of the predictions.

4. ACCELEROMETERS

There were five active accelerometers (at Stations 7.20, 14.75, 19.5, 27.8 and 32.0) in each of the two tests. Predictions were made for each of these five locations by at least some of the calculators.

Unfortunately, the experimental records from the accelerometers were much more hashy than the records from the strain gages. There was little correlation between the two tests and not much agreement among the predictions. The best results were those from Stations 19.5 and 32. These are shown in Figs. 61-62. Figure 61 shows the axial accelerations (both experimental results and all predictions) on a steel block embedded in the potting at Station 19.5. There is little agreement among the six predictions which differ considerably from one another in both phasing and magnitude. The predictions of LLL, SLA/S, and CRT all predict a first peak of about 9 kg at a time of about 150 μ sec. AVCO and SLA/H predict a first peak of about 11 kg at 225 μ sec and UICC predicts 16 kg at 300 μ sec. Test 1 shows a first peak of about 13 kg at 275 μ sec, while Test 2 shows a first peak of 8 kg at 200 μ sec followed by a second peak of 10 kg at 300 μ sec. It is very difficult to draw any conclusions from the crowded Fig. 61 and those results are the best of the five accelerometers.

The other results presented here are those for the accelerometer at the outside edge at the rear of the outer casing. These are shown in Fig. 62. Once again, it is hard to draw useful information from these results. The seven predictions vary greatly in both magnitude and phasing and the two experimental results do not agree at all.

Because of the lack of consensus among the predictions, the test results were not shifted at all. It is perhaps worth noting that some correlation between the predictions and Test 1 could be obtained by shifting Test 1 to the left by about 50 μ sec. In that case, the predictions by AVCO, CRT, and WA of both the first peak (about 20 kg at about 180 μ sec) and the onset of the negative phase (at about 350 μ sec) would agree well with Test 1. But the failure of Test 2 to even approximately resemble Test 1 at this station tends to discourage us from being too pleased with these predictions.

The strain gage data from these tests was much more useful than the results from the accelerometers.

VII CONCLUSIONS AND OBSERVATIONS (PRE-SHOT)

The following conclusions are drawn only from an analysis of the calculations completed and presented before the tests. Some results that were generated after an analysis of the experimental results are reported in the next section.

The first conclusion is that the theoretical predictions were in remarkably close agreement at many stations, so close that the test results can not be used to indicate any preference for one method over the others in most cases. The reason for this is simply that the test results, as fine as they are, are not as consistent among themselves as the various calculations generally are. As an example look again at Fig. 32 where the results for the station 19.5 axial strains are shown. There were four test results (0° and 180° for each of two tests) and they were intended to be identical. But, the 180° gages for each test are suspect (even though one of them gave a good signal from 100 to 200 μsec) while the gages at 0° responded well during the entire test and agree rather well with each other. Based on the Test 2, 0° , result alone the WA prediction would seem to be closest but the Test 1, 0° , result agrees slightly better with the predictions of the AVCO and LLL calculations (as well as those of SLA/S and UICC). A similar set of contradictory conclusions can be drawn from Fig. 35 showing the hoop strains at station 19.5. Again, the 180° gages for each test are suspect while the Test 1, 0° , gage seems to agree best with LLL while the Test 2, 0° , agrees better with every calculator reporting except LLL. Thus, it may be seen that the test results are not sufficiently reproducible to be able to use them to indicate a clear superiority for one of the approaches over the others.

A second conclusion is that, in these tests, there was not much interaction between the outside casing and the interior package. This conclusion is based on the excellent predictions that were made by some calculators using very simple models. The WA prediction, for example, was based on a relatively small number of modes from an analysis of the outer casing using elastic thin shell theory. The entire contents (the liner and all the interior components) were represented by a single mass attached by a spring to the nose of the penetrator. Yet the WA predictions (for both axial and hoop strains) agree very well with the predictions of the more detailed models and with the test results at each of the stations along the outer casing. Such an elementary model would not have yielded such excellent results if there was considerable interaction between the outside casing and the interior structure. Thus, it seems clear that the outer casing is driving the interior structure and a further uncoupling (similar to the uncoupling in which the loading on the penetrator was assumed to be independent of the response of the penetrator) of this problem is feasible. Thus, a three step procedure may be suggested for this problem (normal penetration): 1) Calculate the loading on the penetrator as though it were rigid; 2) Apply this loading to the outer shell of the penetrator (modeling the interior very simply) and determine the motions of the casing; then 3) Apply these motions to the internal structure (now modeled with whatever detail is required) at the points where there is a connection between the casing and the internal structure and determine the motion of the internal structure.

Examination of the UICC results supports the argument that there is little interaction between the casing and the internal structure. The UICC model is even simpler than the WA model. It contains only two rods

connected to a mass. This model predicted axial strains at stations 9 and 19.5 which again agree very well with the other predictions and the test results. This simple model gives no predictions on the hoop strains.

A third conclusion is that the loading prediction by CRT was very good. This supports both the validity of the CRT calculation and the major original assumption that the loading on the penetrator was independent of its response. This conclusion is based on the good agreement, for the full 500 μ sec, between the average of the predictions and the test results (like those at station 19.5 on the casing) which gave a reliable signal for 500 μ sec.

A fourth observation is that all the calculators can respond very quickly to a given problem with two major exceptions: 1) accepting input generated external to their programs, and 2) providing results in a form suitable for automatic comparison with other predictions and test results. An examination of the time spent on various tasks by each contractor suggests that the modeling of the structure and the determination of the response of the structure were quite routine for all of them even though the structure was quite complex (a set of very detailed parts drawings was sent to each calculator) and it was not uncommon for each calculator to thoroughly investigate as many as four different models of the structure. But the calculators are familiar with the modeling of complex structures and with the interpretation of their response and this task usually took only a few weeks. But they all had difficulties using the input generated for them. It was not uncommon for a calculator to spend a month making the CRT loading compatible with his code. In fact, of the seven calculators, only WA used the loading tape generated by CRT. Even CRT didn't use their own loading tape in their response calculation. They digitized, as did everyone else but WA, the

plots of the loading which were provided by CRT along with the loading tape. This process of digitizing the plots of the loading took much time because there were plots of both radial and axial forces at as many as 39 stations to be processed. The usual reason given by most of the calculators for preferring to digitize each curve individually was that it was a familiar task whose completion within a certain time (albeit as long as six weeks) could be guaranteed whereas if they had trouble processing the magnetic tape (and many of them had such troubles in the past) they might be delayed months and miss the deadline when the predictions were due, a date about three months in the future when the contractors made the decision not to automate the loading. So they chose the safe, if tedious, solution since that way they could guarantee results. Since WA was trying to cover areas not covered by the other calculators, they used the load tape as generated by CRT. There were no technical difficulties in doing this. The load tape proved reliable, except for one easily recognized out-of-range value, and easy to process. It took WA only a few hours to prepare a routine that read the load tape and supplied the loads to the response program. It is desirable to be able to use the load tape as generated and immediately find the response of a model. Thus, in the future, a routine should be distributed with the loading tape which processes the tape and provides the values of the forces at any location at any time. Such a general routine is not simple to create and the difficulties of developing such a routine, under deadline pressures, clearly discouraged most of the calculators from attempting to process the tape directly. But, if the need for such a routine is recognized in advance, it can be developed at the same time that the loading is being determined and the structure is being modeled. Then, when the loading is available there is no delay in applying it to the model.

The experience of WA in developing such a routine leads to the following observations. The load tape represented a rather large file. There were 1452 time cycles, for the 465 μ sec covered, with both axial stresses and forces and radial stresses and forces for as many as 39 stations for each cycle plus certain redundant indices. It was quite feasible to process such a large file, on tape, for one or two response calculations but it was too big for repeated processing. So WA created a much smaller file, that could be conveniently stored on a disk, by eliminating the stresses and the redundant indices. Even this file was too large to be pulled into central memory during execution of small core codes, so the load processing routine would process about 30 time cycles until a later time was required, then replace the 20 oldest cycles with 20 new cycles allowing 10 cycles to remain since certain integrating routines, e.g. the Runge-Kutta approach, periodically sample the forcing function at a half step earlier than the then current value of the time parameter. The WA routine interpolated in time between CRT time cycles to find the proper values of the forces but did not interpolate in space because WA chose its mesh spacing on the nose to correspond to the CRT load points. But the more general routine required by the other contractors would probably require interpolation in both space and time.

The other task that some of the calculators found to be less than routine was the presentation of the output in a form suitable for comparison with the other predictions and with the test results. The best way to accomplish these objectives would have been for each calculator to deliver their results stored on a magnetic tape. Then the results could have been drawn to any scale and cross-plotted against each other and the test results in any fashion that might have been desired. But delivering results in such a mode is not yet a familiar and error-free procedure for many calculators, so they were asked to submit plots instead. But then time and amplitude

scales for these plots were specified, so that they might be overlayed, and most of the calculators had some difficulty in providing the plots with exactly the right scales. In general, the plotting to specified scales required some modifications to the codes. Thus, the tasks of modeling and solving the structure were more routine for most of the calculators than were the tasks of automatically processing externally produced input and automatically supplying output to certain specifications. It would seem desirable, in the future, to encourage the calculators to be as efficient in their pre- and post-processing efforts as they are in their modeling and problem-solving.

A fifth conclusion is that the day of the repeatable penetrator experiment, the test that provides consistent and redundant results, has not yet dawned. By any reasonable standard, and especially when compared with previous penetrator tests, this Sandia-AVCO effort was a remarkable success. The two tests were nearly identical; both had no serious flaw; only a few of the channels failed to provide useful data; and the experimental results look very much like the theoretical predictions say they should look. But when an effort is made to use the redundant test results to decide which of the predictions is the "best", it is quickly realized that the experimental results are not redundant enough for this purpose; in fact, the scatter among the experimental results generally is far greater than the differences among the predictions. The tests were designed to provide as many as eight identical signals at four different gage locations: axial and hoop strains on the outside casing and on the inner liner, all at station 9. At none of these four locations is there general agreement among the eight "redundant" records. As an example, consider the seven maximum millistrains recorded by the seven (90°, Test 1, provided no signal) axial strain gages on the outer casing (all values in tension): 1.8, 3.0, 2.5, 2.6, 2.0, 2.0, 2.8.

A sixth, and related, observation is that there was considerable noise in many of the experimental records. The traces reproduced in this report all begin at "zero" but the raw data from each gage begins 500 μ sec or so earlier and these pre-impact records, which should show no motion at all, often contain signals of the same order of magnitude as the eventual maximum disturbances. Taking the magnitude of these pre-existing oscillations into account casts further doubt on the wisdom of using the experimental results to indicate a preference for one prediction over another.

A seventh observation is that it would be desirable if the experimental results could be delivered on a magnetic tape so that they can be automatically cross-plotted against each other and against various predictions. For this project, perhaps because of the same deadline pressures that inhibited the calculators from trying more automated pre- and post-processing, all the experimental results were plotted by hand. The plotting was done very carefully and no errors have been found, but it would have been a great help in the comparison studies if the test results had been made available in a form suitable for automatic processing.

An eighth observation indicates the more detailed codes can do a very effective job of handling rather complicated load paths and hence predict motions of the internal components even when there are several possible ways in which the internal and external systems can be coupled. An excellent demonstration of this was provided by the LLL analyses, all finished preshot. One of the effects investigated by LLL was the consequences of whether or not the model allowed the inner liner to interact with the outer casing. Four figures [Figs 63-66] from the LLL report Ref. [6] are reproduced here to show the effects of two different models of the gap between the inner liner and the outer case. When the liner is allowed to

bear on the case, the compression in the liner is reduced by only about 10% as may be seen from Fig. 63 . But LLL observes that perhaps the most significant effect of the interacting liner can be seen in the hoop strain of the liner along the taper (Fig. 64). When the liner does not interact with the case, tensile hoop strains develop due to a Poisson effect from the large axial compressive state. However, when the liner is allowed to interact with the case, compressive hoop strains develop since the liner is compressed radially by "wedging" itself along the taper.

The axial strains on the outside of the case are not influenced by the liner (Fig. 65). However, the hoop strains increase on the outside case since the liner is allowed to "push" radially on the case along the taper (Fig. 66). It is interesting, with this interaction effect in mind, to look again at the comparison of the hoop strains in liner at station 19.5, (Fig. 48). Notice that the LLL results presented there are those from the model allowing interaction. It is clear from Fig. 64 that the LLL results from the model without the interaction effect would plot very close to the average values reported by the other calculators, who did not assume such an interaction. Notice also that in the figure comparing hoop strains in the outer casing at station 19.5, Fig. 34 , LLL was higher, with their interacting sides model, than the other calculators, Fig. 66 clearly indicates that their non-interacting sides model gives results very close to those of the other calculators.

A ninth observation is that the effects of plastic material behavior on the results were not critical. Some early results from CRT support this conclusion. CRT performed two NONSAP analyses, one with linear material models and the other with nonlinear material response. Little yielding was observed except in the uranium ballast. This yielding in turn influenced

only the strains on the nose to any significant degree. Fig67 from the CRT data package Ref. [9] shows that the tensile hoop strain at the inner surface of the steel casing at station 4 was doubled by allowing the adjoining uranium to yield.

A tenth, and final, conclusion is that the state-of-the-art in calculations is sufficiently advanced, at this time, to adequately design for the response of a penetrator in a normal impact condition.

VIII POST SHOT RESULTS

The simplest model of the eight considered in this report was the wave transmission model of Georgia Tech. This model was used to predict peak strains before the tests. Since that time, Georgia Tech. has used their wave transmission model to calculate time histories as well. Typical results are shown in Figs. 68-69. Comparison of Fig. 68 with Fig. 22 shows that the results agree well with the other theoretical calculations for the outside casing at station 9. Similarly, Fig. 69 may be seen to agree well with the other theoretical calculations (see Fig. 39) for the inside of the liner at station 9.

The next simplest model considered in this report was the mass and the two rods model of Belytschko. (See Section V-7 for a brief description of the model.) Belytschko analyzed the experimental results and concluded that his results using his Model 2, in which the two rods (which represent the outer and inner case) are not connected at the back end of the vehicle, compared better with the experiments than did his Model 3 results which are reported here. His Model 3 had the two rods connected at the back.

Belytschko also noticed that his crude model gave strains in the outer case which compared better with the experiment than did his strains in the inner case, a fact he attributed to the fact that the simpler models homogenize the contents of the inhomogeneous inner case.

Belytschko also observed that the accelerations predicted by his simple model compared well with the experiment (see Figs. 61 - 62), perhaps due to the inherent filtering of the crude model.

REFERENCES

- 1 Wagner, M.H., Fulton, C.C., and Coerke, W.S., "Data Package, Calculation of Reverse Ballistic Test Into Dakota Sandstone at 1800 ft/sec", California Research and Technology, Inc., February 1976.
- 2 Bushnell, D., "Stress, Stability and Vibration of Complex Branched Shells of Revolution: Analysis and User's Manual for BOSOR4", LMSC-D243605, Lockheed Missiles and Space Company, Inc, March 1972.
- 3 Bathe, K., Wilson, E.L., and Iding, R.H., "NONSAP - A Structural Analysis Program for Static and Dynamic Response of Nonlinear Systems", Report No. UCSESM 74-3, University of California, Berkeley, February 1974.
- 4 Key S.W., "HONDO, A Finite Element Computer Program for the Large Deformation Dynamic Response of Axisymmetric Solids", SLA-74-0039, Sandia Laboratories, Albuquerque, April 1974.
- 5 Jones. R.E., "QMESH - A Self-Organizing Mesh Generation Program", Sandia Laboratories, SLA-73-1088, July 1974.
- 6 Dropak, R.K., Butters, S.W., and Jones, A.H., "Some Mechanical Properties of Mica-50 Potting Compound", Terratek Report, TR76-4, February 1976.
- 7 Grant, J.E., Gabrielson, V.K., "SHELL SHOCK Structural Code", Sandia Laboratories, SAND75-8013, August 1975.
- 8 Pepe, R.D. and Henderson, D., "P2 Structural Dynamics Response Analysis", AVCO Systems Division, Wilmington, Mass., May 1976.
- 9 Ito, Y.M., "Preliminary Result Package - One-Half Scale Penetrator Dynamic Structural Response Calculation", California Research and Technology, Inc., Woodland Hills, California, April 1976.
- 10 Sturbis, P., "Analytical Response of an Earth Penetrator", Sandia Laboratories, Albuquerque, New Mexico, February, 1977.
- 11 Alves, D.F., and Goudreau, G.L., "Structural Response Calculations For a Reverse Ballistics Test of an Earth Penetrator", Lawrence Livermore Laboratory, Livermore, California, August 1976.
- 12 Belytschko, T., "Semianalytic Methods for Axial Response Analysis of Penetrators", DNA 4044F, Defense Nuclear Agency, Washington, D.C., June 1976.

TABLE 1. REVERSE BALLISTIC TEST INSTRUMENTATION.

Channel number	Sensor type and number	Station (in)	Meridian (deg)	Orientation	Location	Band edge (°)	Tape trk. no.	PPSA-1		PPSA-2	
								Time to impact from scope sweep start (μs)	Time to impact from scope sweep start (μs)	Time to impact from scope sweep start (μs)	Time to impact from scope sweep start (μs)
1	S.G. S-1	9.0	0	Axial	10 Can	5K	1	504			390
2	S.G. S-2	9.0	90	Axial	10 Can	5K	1	504			390
3	S.G. S-3	9.0	180	Axial	10 Can	5K	1	504			390
4	S.G. S-4	9.0	270	Axial	10 Can	5K	1	504			390
5	S.G. S-5	12.0	0	Axial	Payload	2K	1	504			390
6	S.G. S-6	12.0	180	Axial	Payload	2K	2	428			314
7	S.G. S-7	16.0	0	Axial	00 Pot	10K	2	428			314
8	S.G. S-8	16.0	180	Axial	00 Pot	10K	2	428			314
9	S.G. S-9A	19.5	0	Axial	10 Can	6K	2	428			314
10	S.G. S-9H	19.5	0	Circ	10 Can	6K	2	428			314
11	S.G. S-10A	19.5	180	Axial	10 Can	6K	3	500			386
12	S.G. S-10H	19.5	180	Circ	10 Can	6K	3	500			386
13	S.G. S-11	26.25	0	Axial	Payload	3K	3	500			386
14	S.G. S-12	26.25	180	Axial	Payload	3K	3	500			386
15	S.G. S-13	27.3	0	Axial	10 Payload	1K	3	500			386
16	S.G. S-14	27.3	180	Axial	10 Payload	1K	4	424			310
17	S.G. S-15	31.5	0	Axial	10 Can	1K	4	424			310
18	S.G. S-16	31.5	180	Axial	10 Can	1K	4	424			310
19	S.G. S-17A	4.0	0	Axial	00 Shell	5K	4	424			310
20	S.G. S-17H	4.0	0	Circ	00 Shell	5K	4	424			310
21	S.G. S-18A	4.0	180	Axial	00 Shell	5K	5	502			388
22	S.G. S-18H	4.0	180	Circ	00 Shell	5K	5	502			388
23	S.G. S-19A	9.0	0	Axial	00 Shell	4K	5	502			388
24	S.G. S-19H	9.0	0	Circ	00 Shell	4K	5	502			388
25	S.G. S-20A	9.0	90	Axial	00 Shell	4K	5	502			388
26	S.G. S-20H	9.0	90	Circ	00 Shell	4K	6	432			318
27	S.G. S-21A	9.0	180	Axial	00 Shell	4K	6	432			318
28	S.G. S-21H	9.0	180	Circ	00 Shell	4K	6	432			318
29	S.G. S-22A	9.0	270	Axial	00 Shell	4K	6	432			318
30	S.G. S-22H	9.0	270	Circ	00 Shell	4K	6	432			318
31	S.G. S-23A	19.5	0	Axial	00 Shell	3K	7	494			380
32	S.G. S-23H	19.5	0	Circ	00 Shell	3K	7	494			380
33	S.G. S-24A	19.5	180	Axial	00 Shell	3K	7	494			380
34	S.G. S-24H	19.5	180	Circ	00 Shell	3K	7	494			380
35	S.G. S-25	27.3	0	Axial	00 Shell	2K	7	494			380
36	S.G. S-26	27.3	180	Axial	00 Shell	2K	8	430			316
37	ACC 1	7.20		Axial		50 Kg	9	490			376
38	ACC 2	14.75		Axial		30 Kg	10	430			316
39	ACC 3	19.5	90	Axial	Stl Comp	30 Kg	11	486			372
40	ACC 4	27.8		Axial	Aft Payload	40 Kg	14	428			314
41	ACC 5	32.0	0	Axial	End Shell	50 Kg	13	484			370

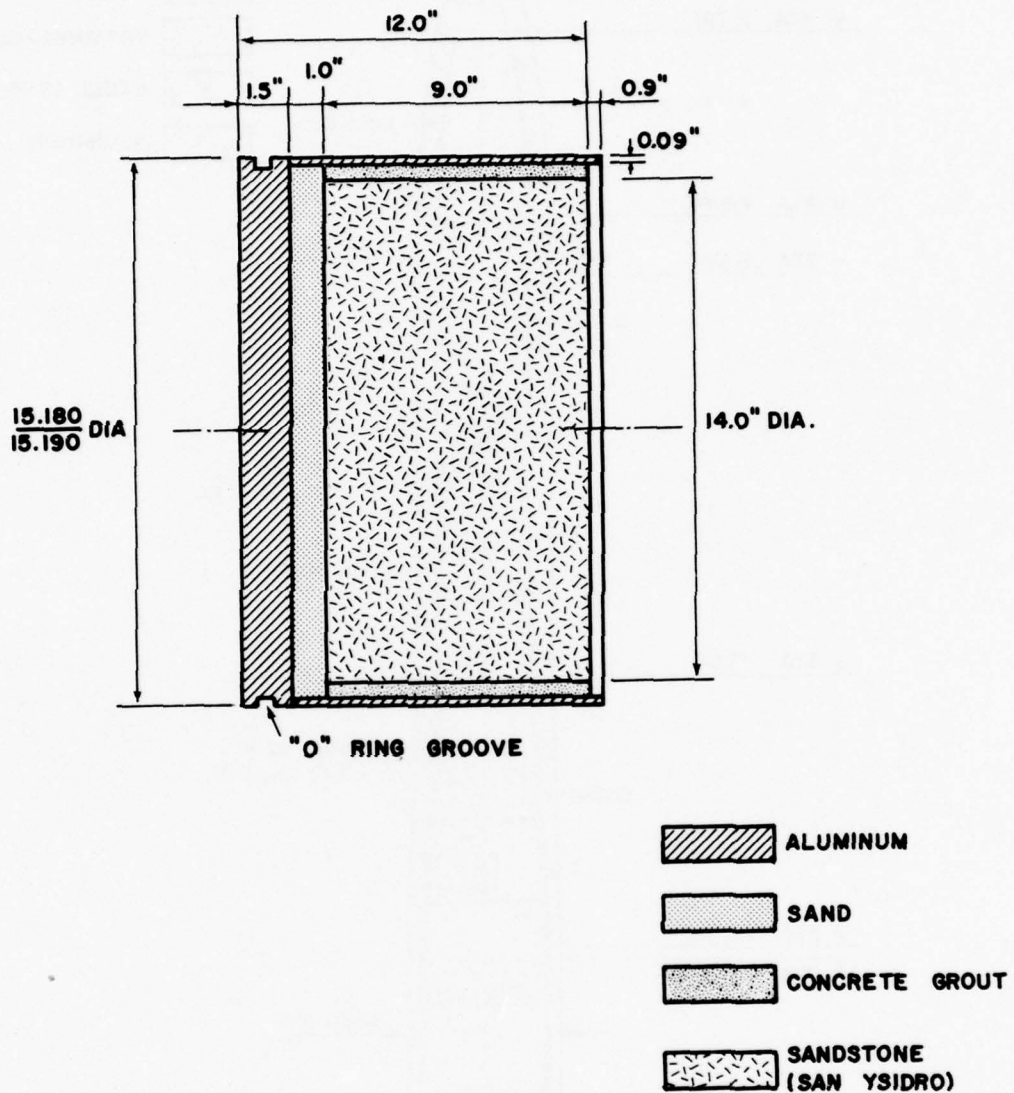
Media Projectile Velocity PPSA-1 Test = 1920 ft/s
Media Projectile Velocity PPSA-2 Test = 1770 ft/s

TABLE 2. NOMINAL PROPERTIES OF TARGET MATERIAL FOR CALCULATION OF REVERSE BALLISTIC TEST.

Property	Dakota Sandstone	Sand	6061-T6 Aluminum
Density, ρ_o (gm/cm ³)	2.02	1.6	2.7
Dilatational Velocity, $(c_p)_o$ (ft/sec)	3886	553	21,036
Shear Wave Velocity, $(c_s)_o$ (ft/sec)	2308	338	10,451
Unconfined Compressive Strength, Y_o (kb)	.23	.00199	2.92
Tensile Limit, T_o (kb)	.007	.000827	9
Bulk Modulus, K_o (kb)	15	.227	744.67
Shear Modulus, G_o (kb)	10	.170	274
Constrained Modulus, M_o (kb)	28.3	.454	1110
Young's Modulus, E_o (kb)	24.5	.409	732.2
Poisson's Ratio, ν_o	.227	.2	.336

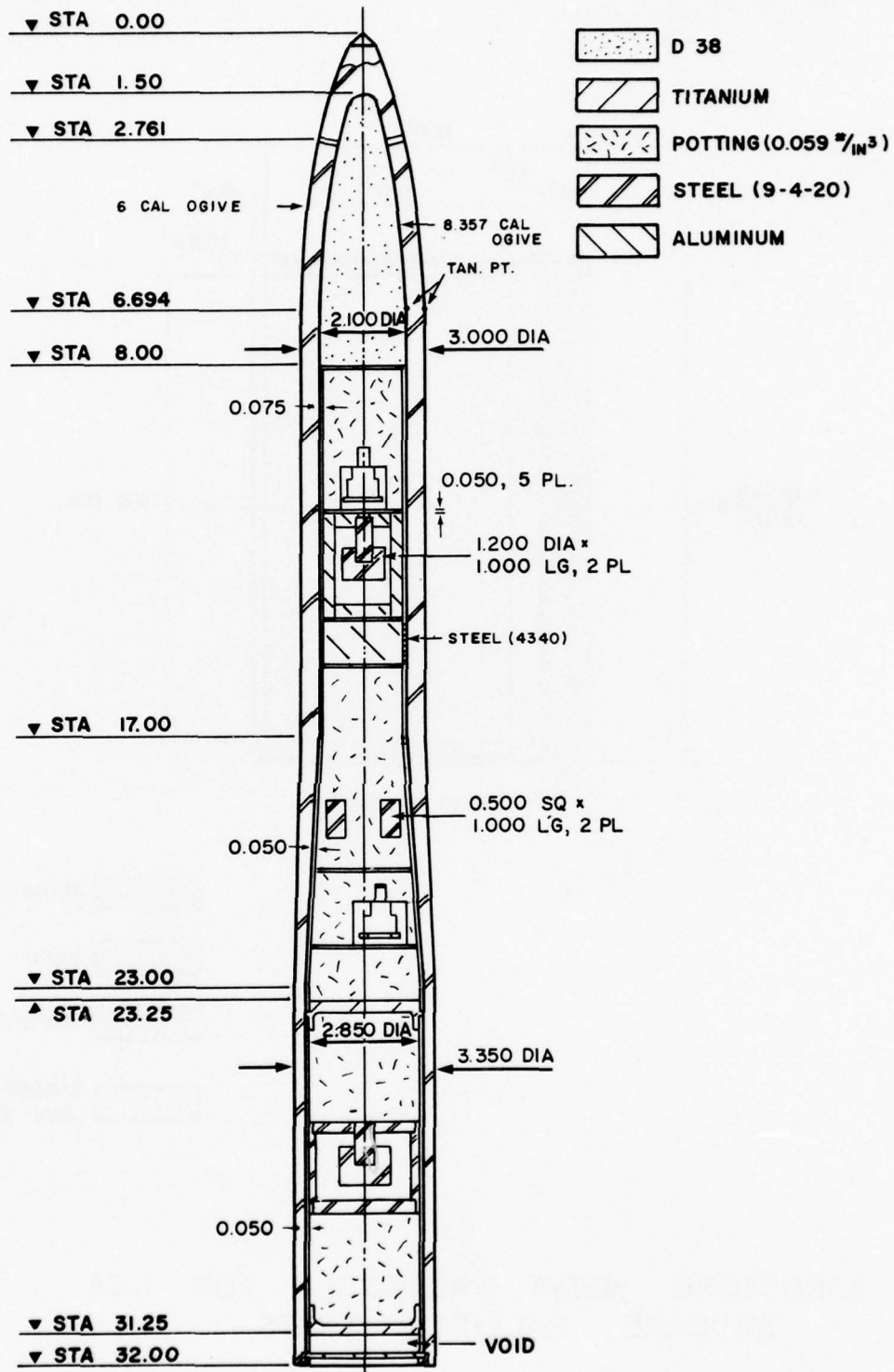
TABLE 3. MATERIAL PROPERTIES.

PROPERTY	9NI-4Co-.2C STEEL	250 MARAGING STEEL	DEPLETED URANIUM	6061-T6 ALUMINUM	MICA-50 POTTING	4340 STEEL	TI-6AL-4V TITANIUM
E -ELASTIC MODULUS $\times 10^6$ PSI	28.5	26.5	27.9	9.9 (TNSN) 10.1 (CPRSN)	1.19 (TNSN) 1.03 (CPRSN)	29	16 (TNSN) 16.4 (CPRSN)
μ -POISSON'S RATIO	0.296	0.3	0.23	0.33		0.32	0.31
ρ -DENSITY (LB/IN ³)	0.283	.289	0.686	0.098	0.059	0.283	0.160
σ_T -TENSION YIELD $\times 10^3$ PSI	185	250	30	36	7.7	132	145
σ_C -COMPRESSION YIELD $\times 10^3$ PSI	200	280	30	35	17.9	145	154



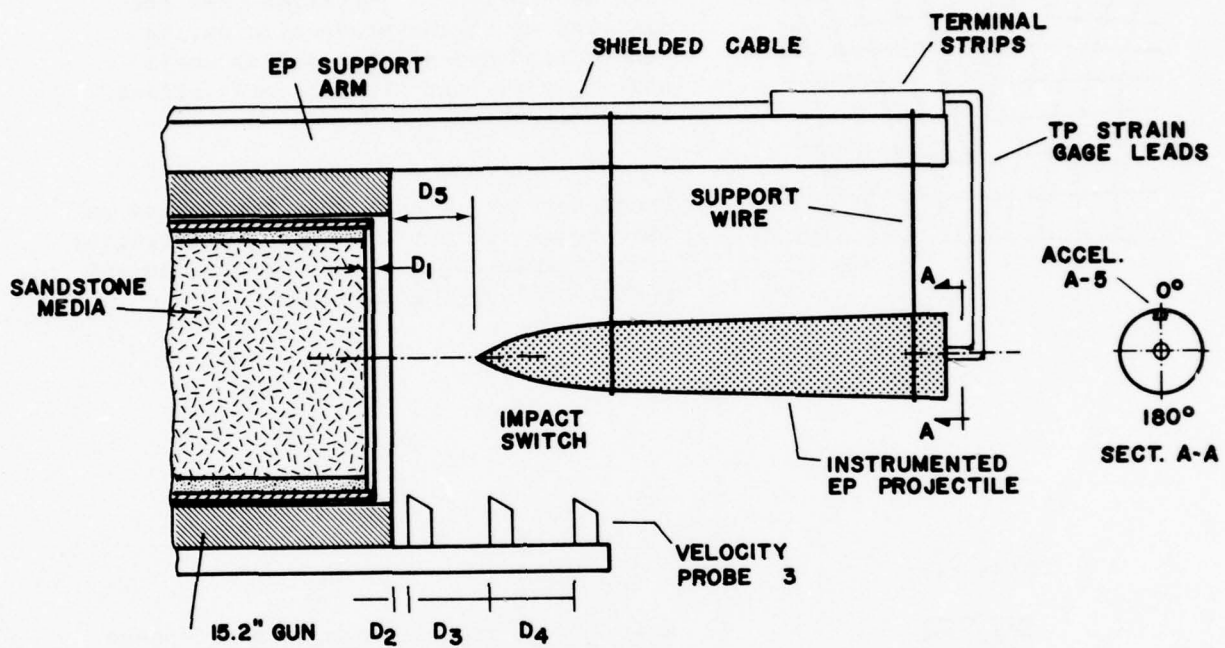
SANDSTONE MEDIA PROJECTILE FOR DNA
REVERSE BALLISTIC TESTS

FIG. 1



HALF SCALE MODEL

FIG.2

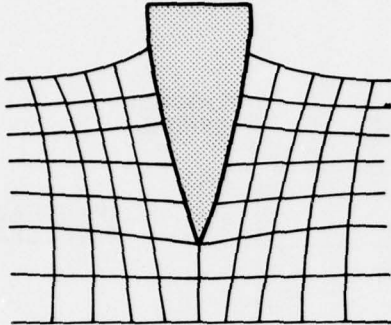


SIDE VIEW OF TEST SETUP FOR DNA PPSA TESTS

FIG. 3

Analysis of penetration dynamics

PHASE I:

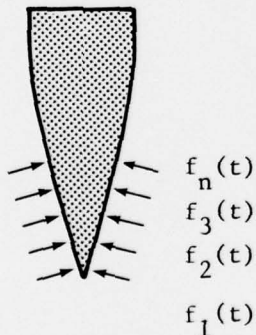


Penetrator is assumed to be a rigid body having same mass and shape as the actual projectile.

This assumption is justified when the distortions of the projectile during penetration are elastic and so small that they do not significantly affect the penetration dynamics.

From the Phase I analysis, the forces on the projectile surface during penetration are determined (as functions of time and position along the surface).

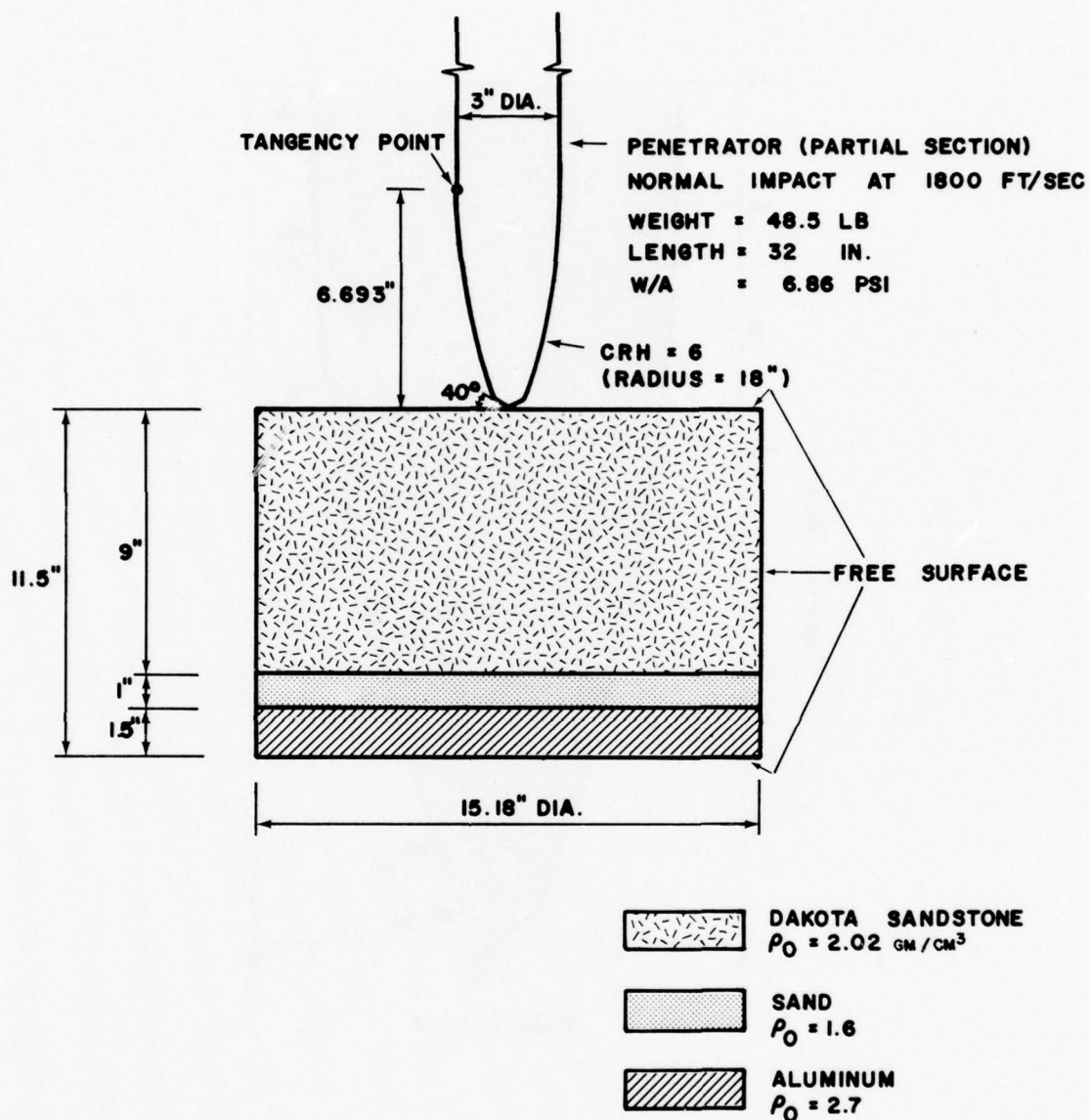
PHASE II:



Analysis of dynamic structural response

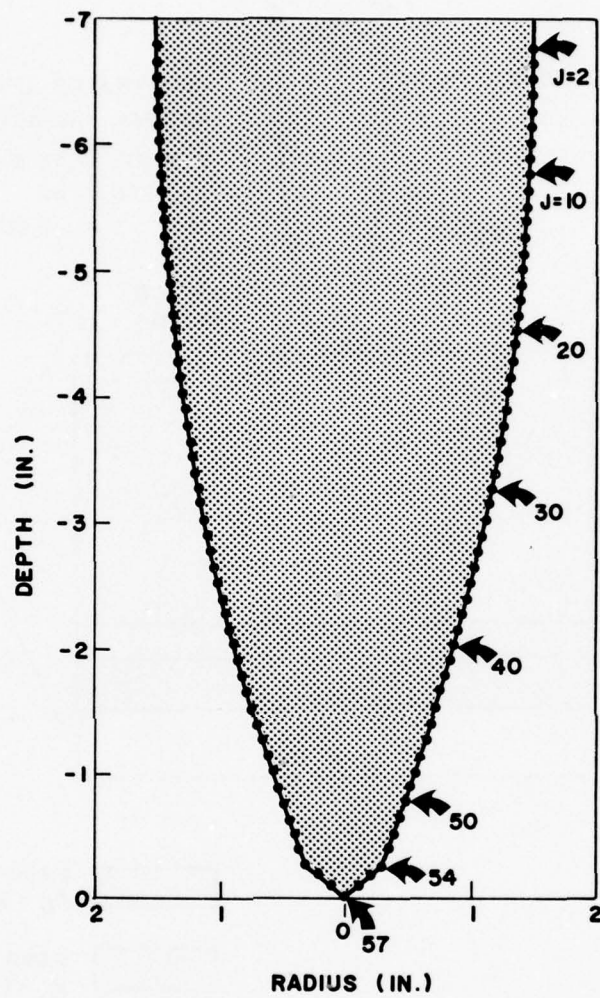
Penetrator is now assumed to be a deformable body, in accordance with the actual configuration and properties of its materials. The response of the projectile and of its internal components, as they are subjected to the surface force loading from Phase I, is determined.

Figure 4 Decoupled Approach for Making Analyses of Penetration and Response Dynamics of Earth Penetrators



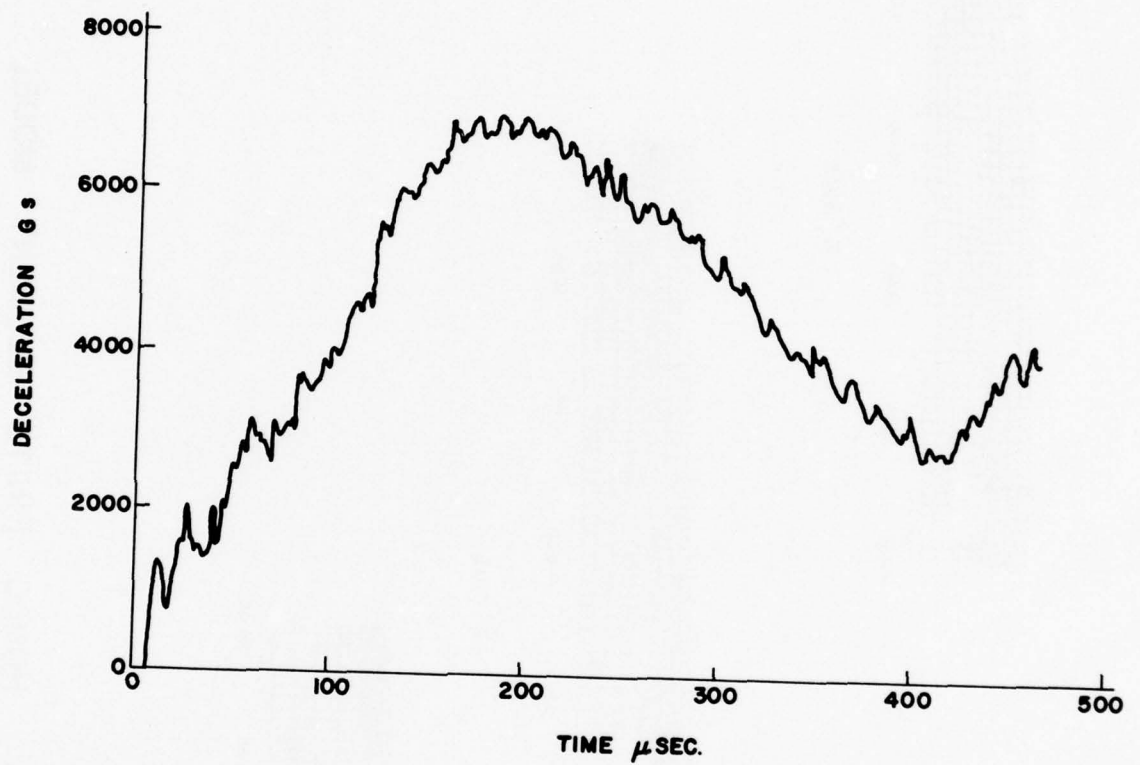
MODEL FOR WAVE - L CALCULATION BY CRT

FIG. 5



NODAL POINTS FOR WAVE - L CALCULATION

FIG. 6



PENETRATOR DECELERATION VS. TIME

FIG. 7

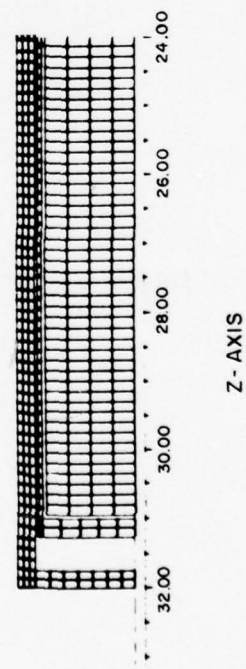
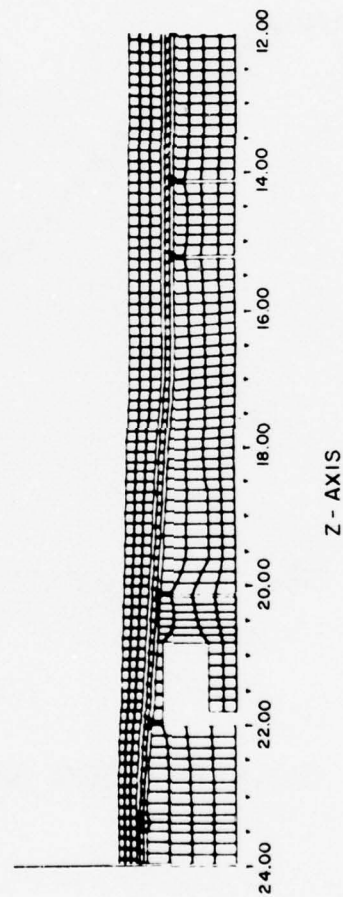
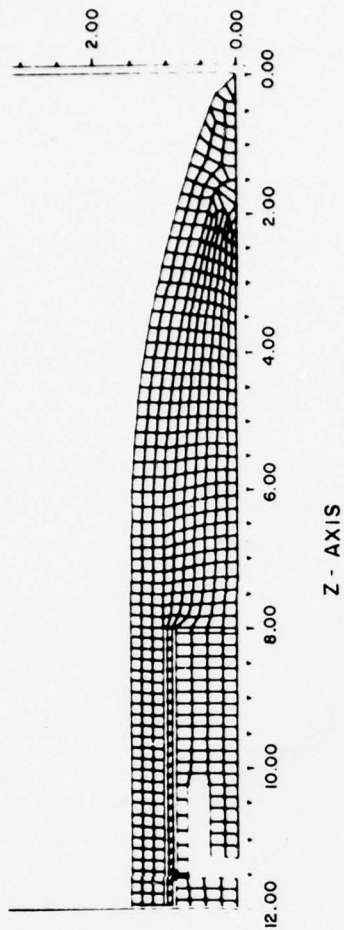


FIG. 8 HONDO FINITE ELEMENT MODEL

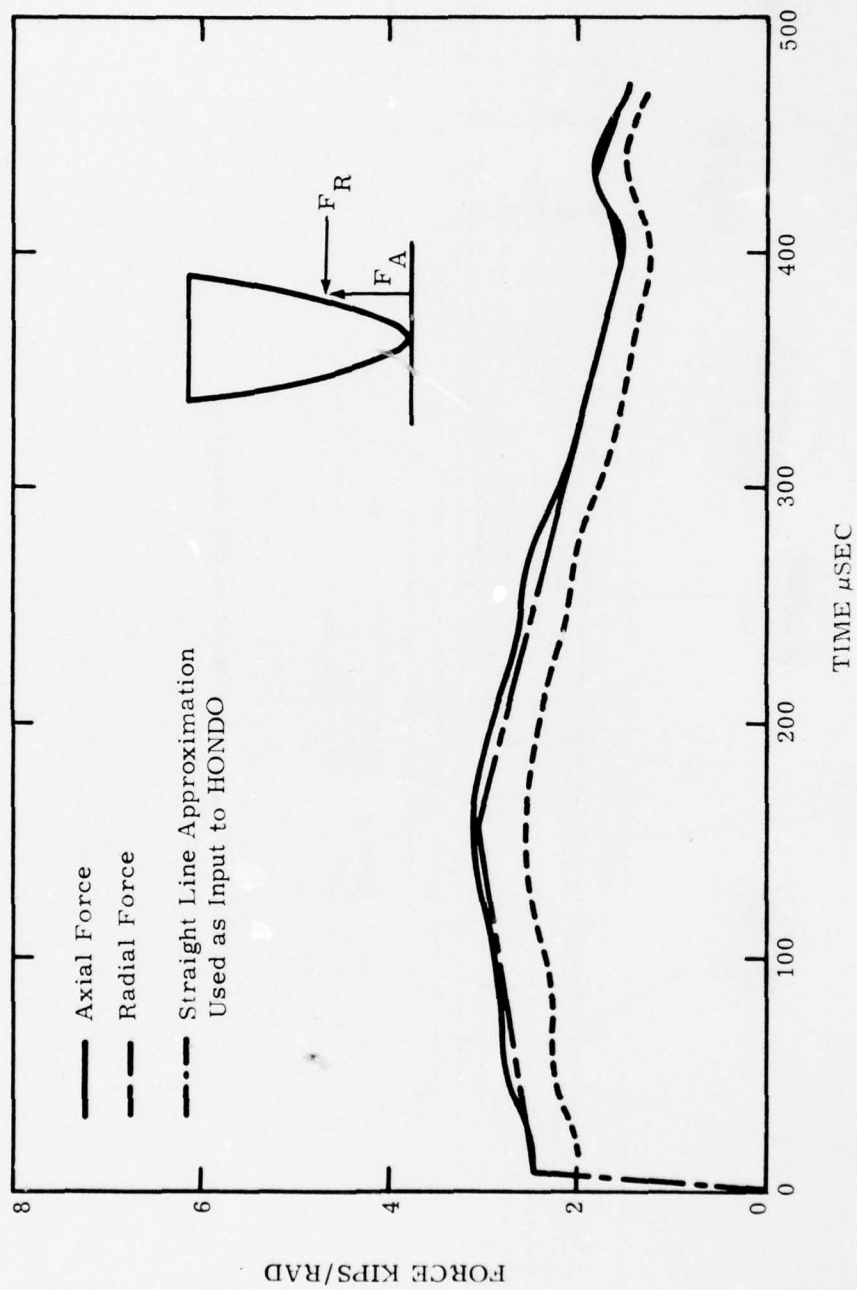
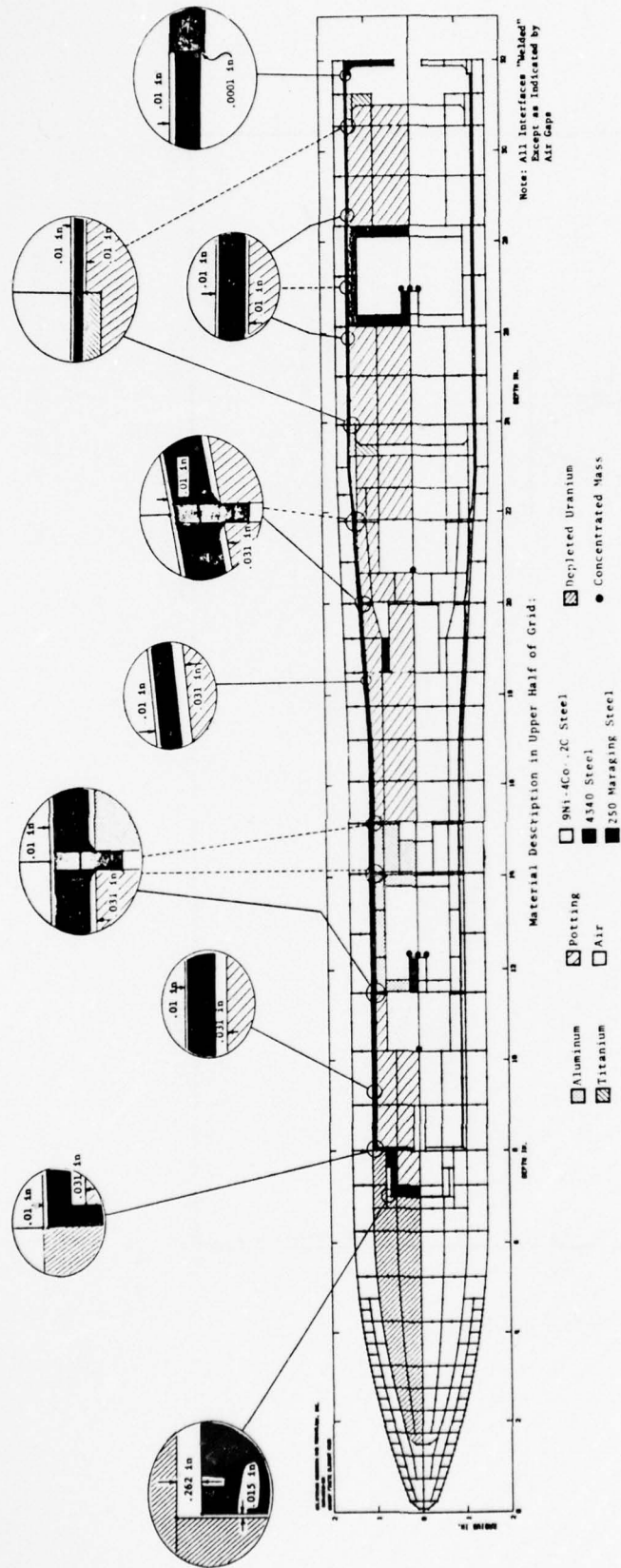


Figure 9 Smoothed Force Time Histories for Projectile Surface Segment

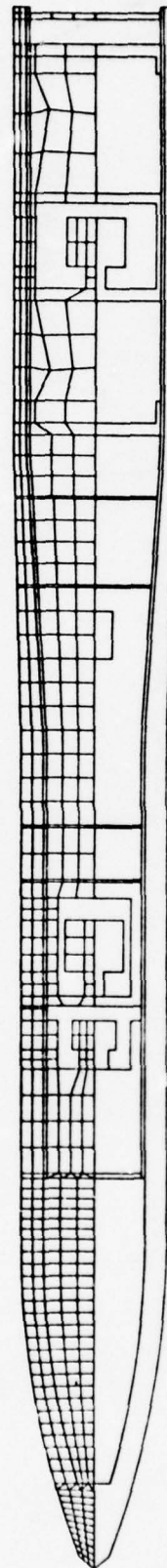


NONSAP Finite-Element Model of RBT Penetrator

FIG. 10

COMPUTER MODEL OF
EARTH PENETRATOR
FOR LLL DTVIS 2
CALCULATION

FIG. 11



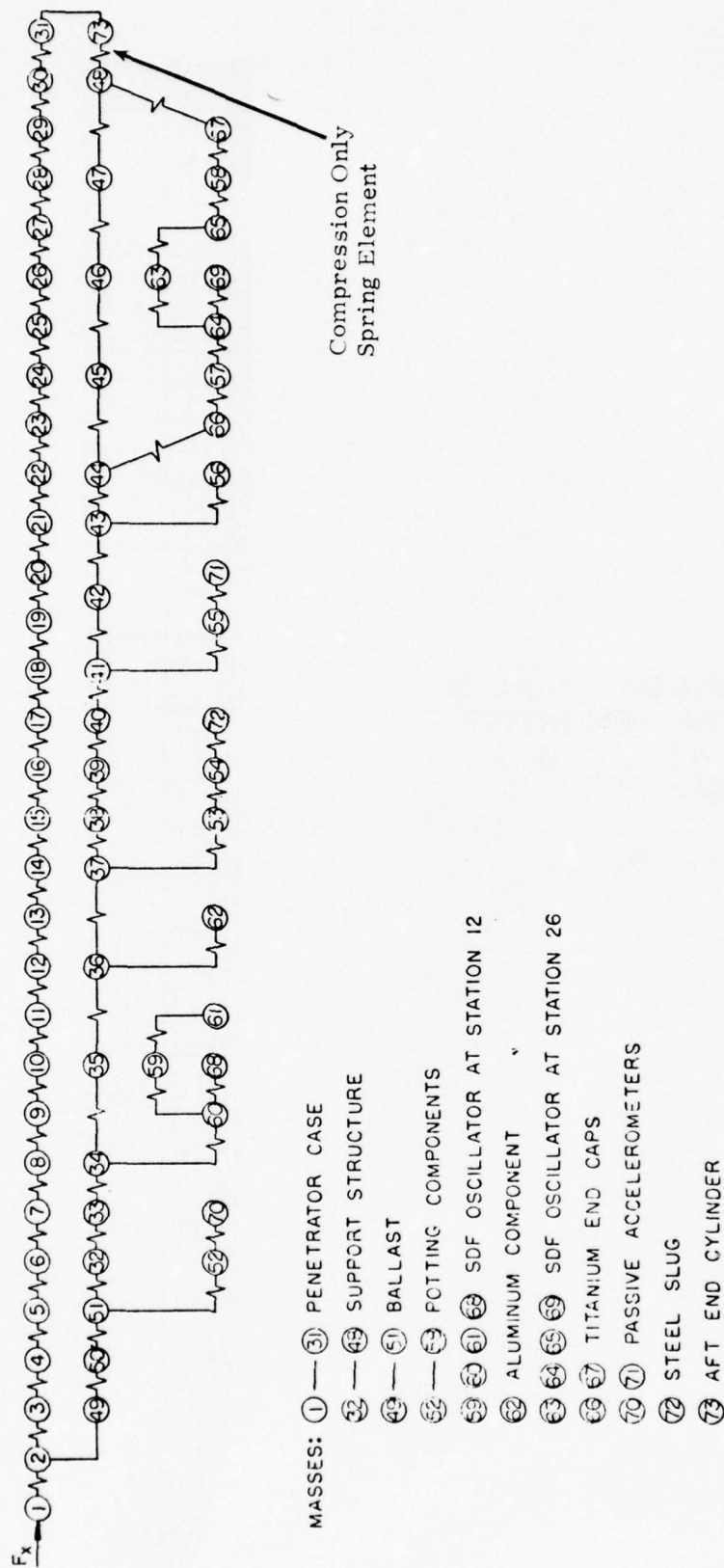


FIGURE 12 SHELL-SHOCK LUMPED PARAMETER MODEL

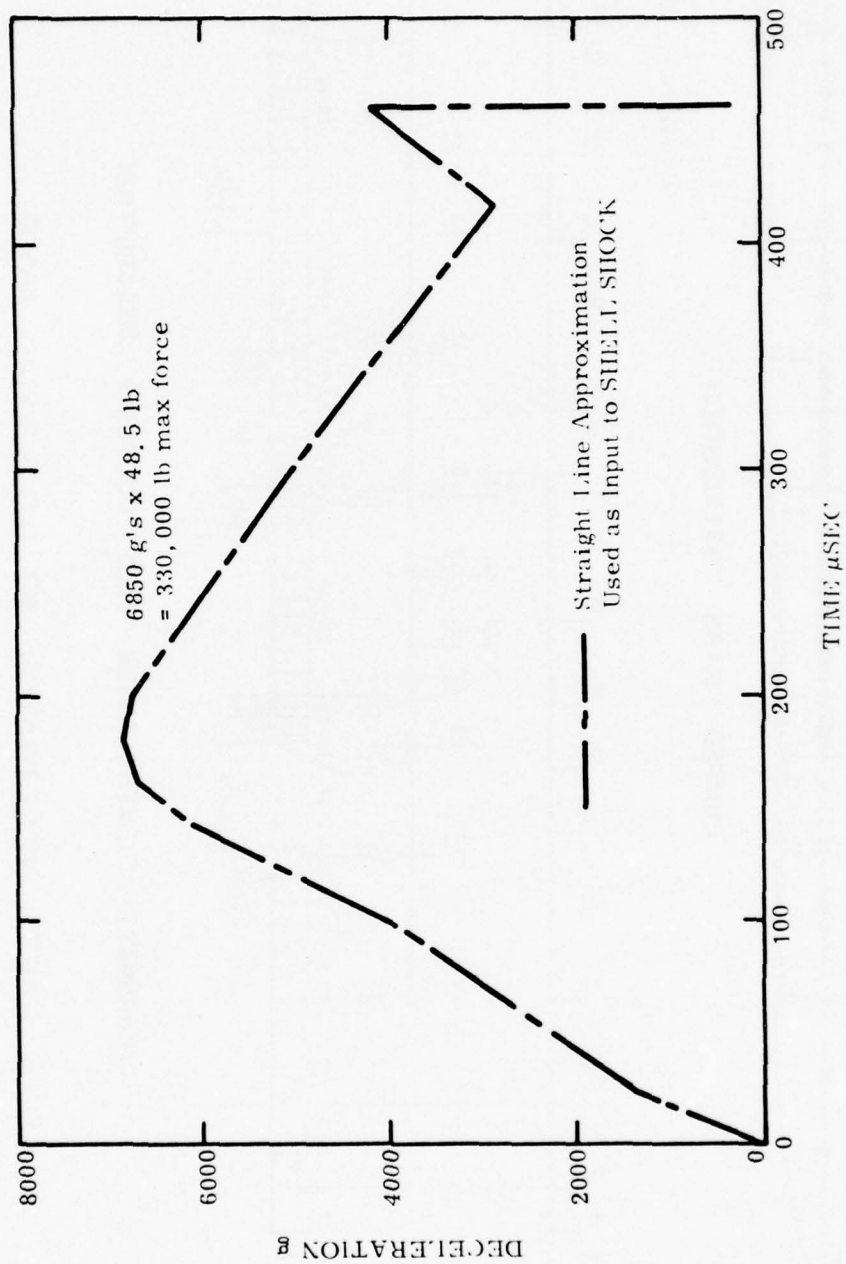
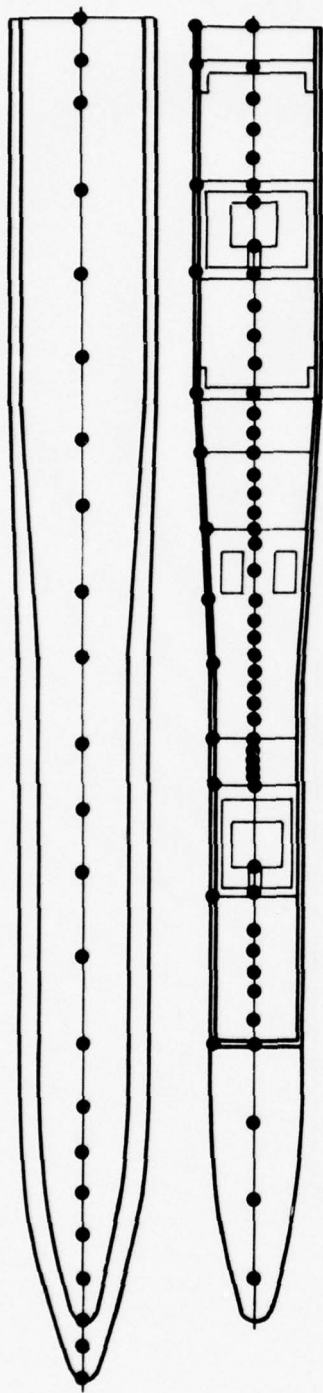
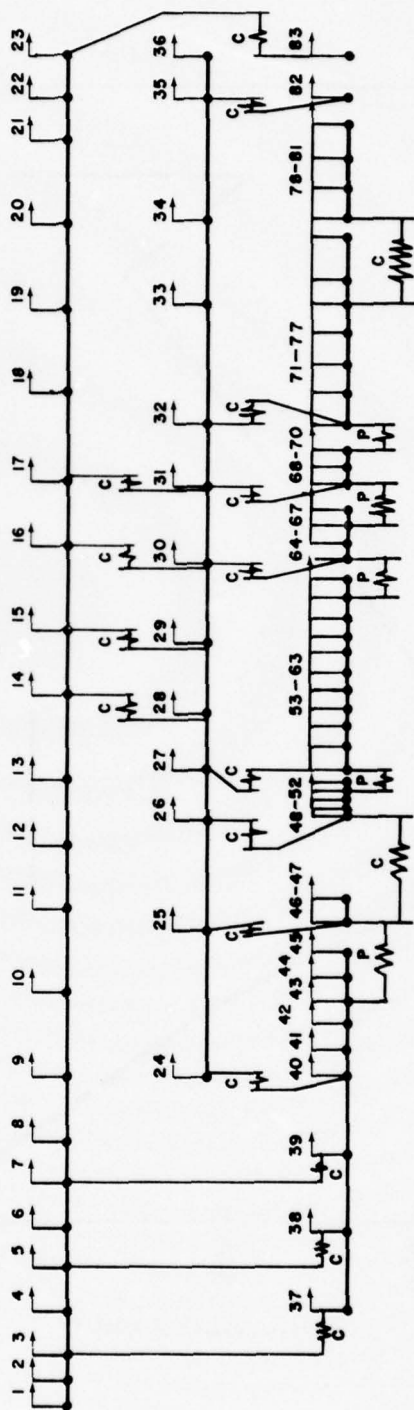


Figure 13 Penetrator Deceleration vs Time



LUMPED MASS DISTRIBUTION

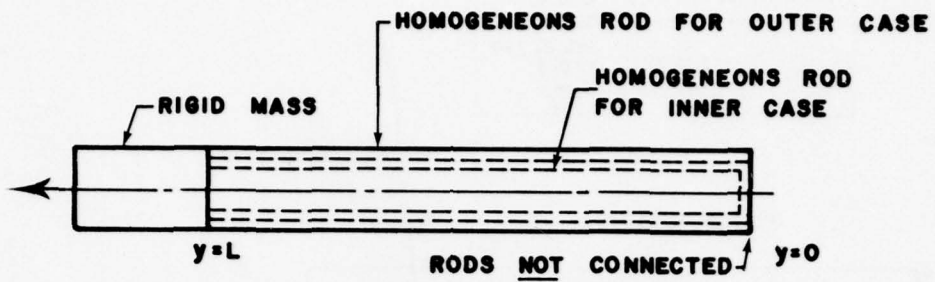
C - COUPLING SPRING
P - PRETENSION COUPLING



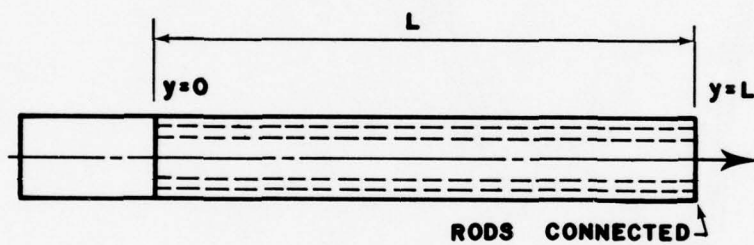
COORDINATE IDENTIFICATION AND COUPLING DESCRIPTION

DNA EARTH PENETRATOR 83 D.O.F AXIAL MODEL

FIG. 14



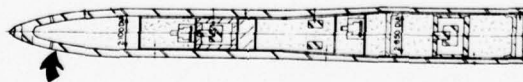
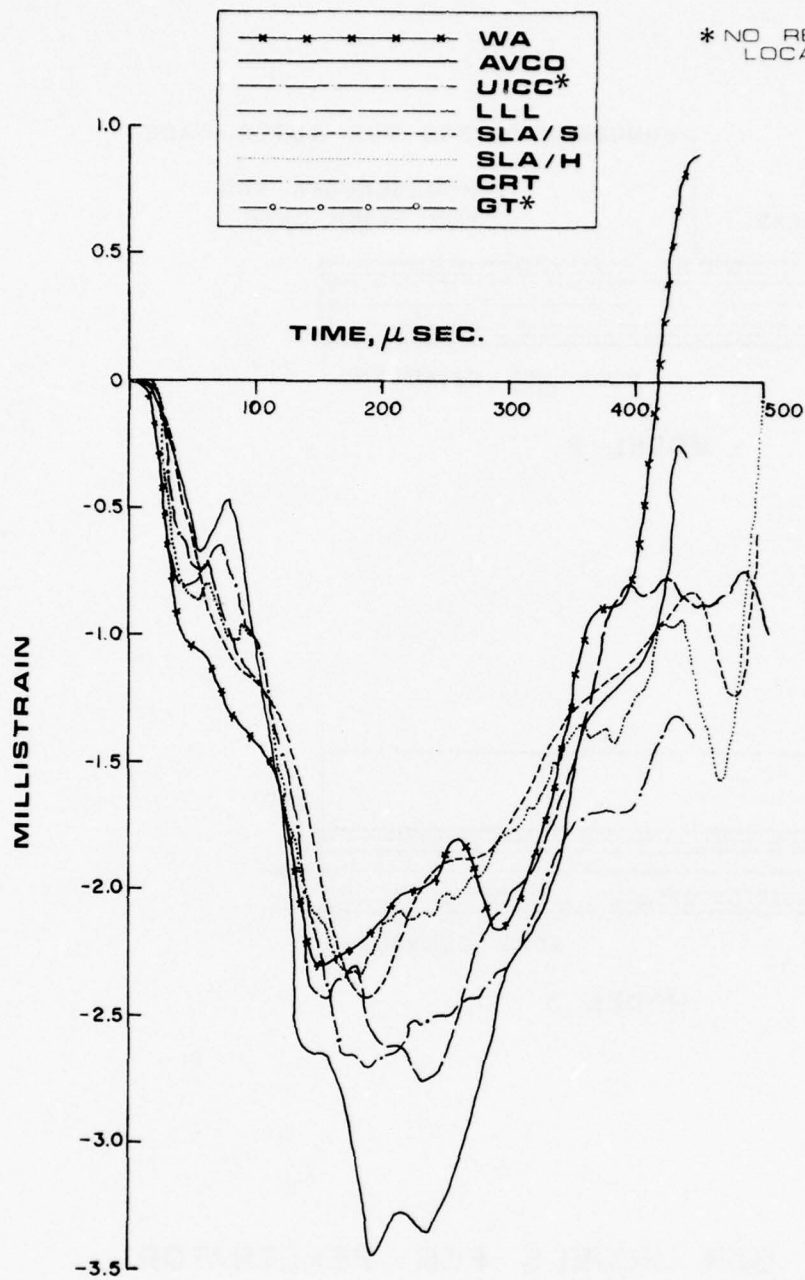
MODEL 2



MODEL 3

PARALLEL BAR MODELS FOR PENETRATOR
BY BELYTSCHKO.

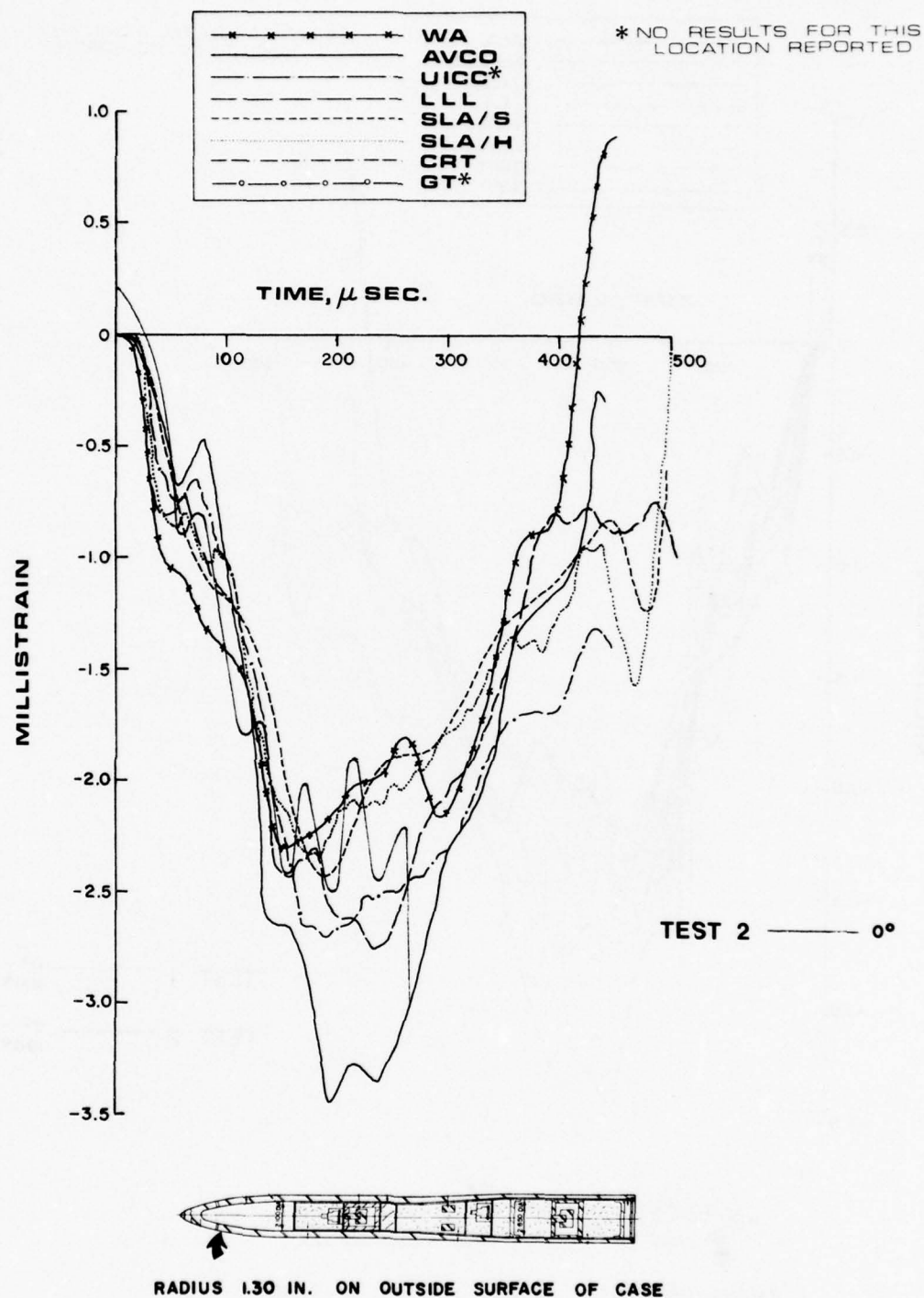
FIG. 15



RADIUS 1.30 IN. ON OUTSIDE SURFACE OF CASE

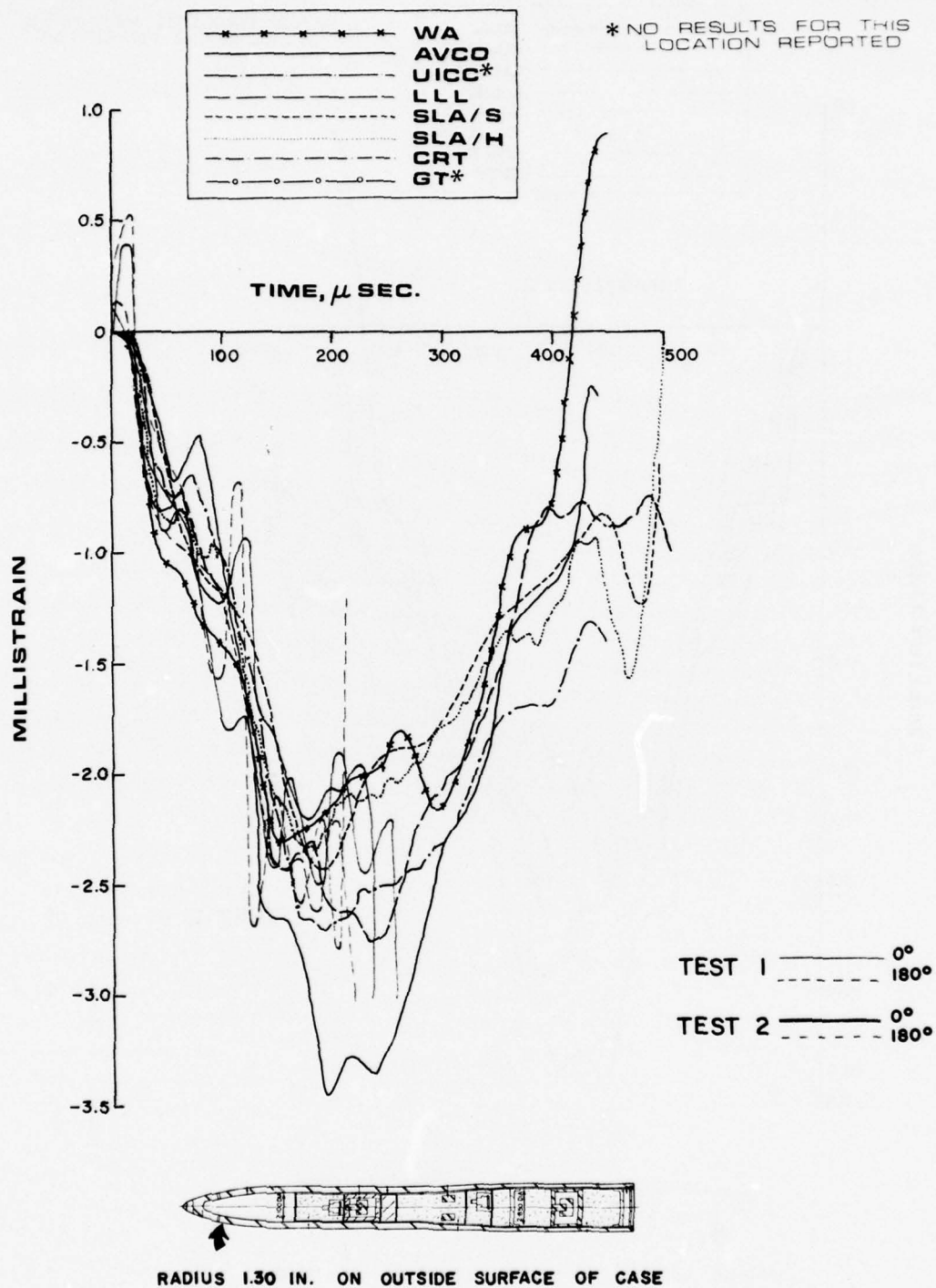
COMPARISON OF THEORETICAL RESULTS AT STATION 4, AXIAL

FIG. 16



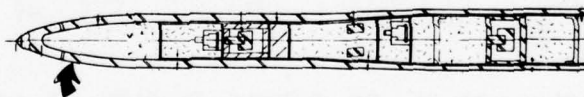
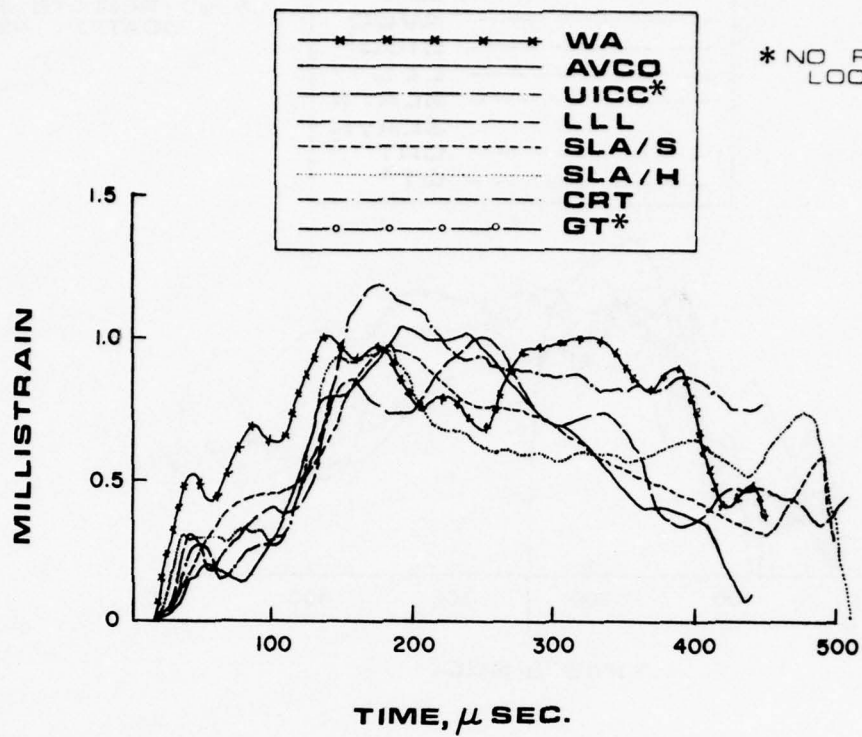
COMPARISON OF THEORETICAL RESULTS WITH A TYPICAL
EXPERIMENTAL TEST AT STATION 4, AXIAL

FIG. 17



COMPARISON OF THEORETICAL RESULTS WITH EXPERIMENTAL
TESTS 1 & 2 (0° & 180°) AT STATION 4, AXIAL

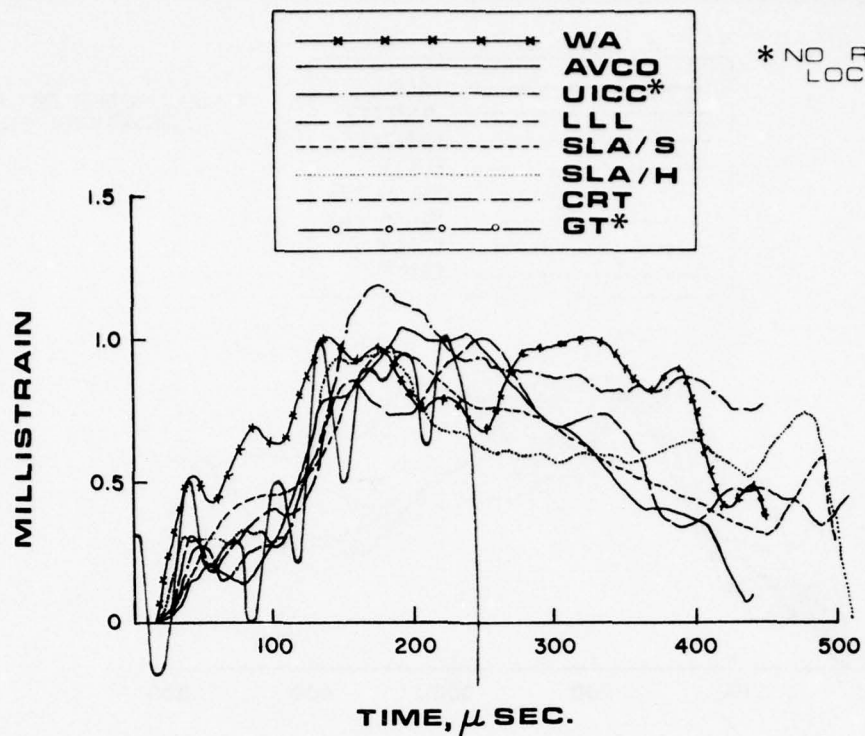
FIG. 18



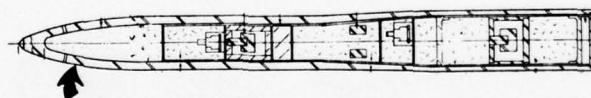
RADIUS 1.30 IN. ON OUTSIDE SURFACE OF CASE

COMPARISON OF THEORETICAL RESULTS AT STATION 4, HOOP

FIG. 19



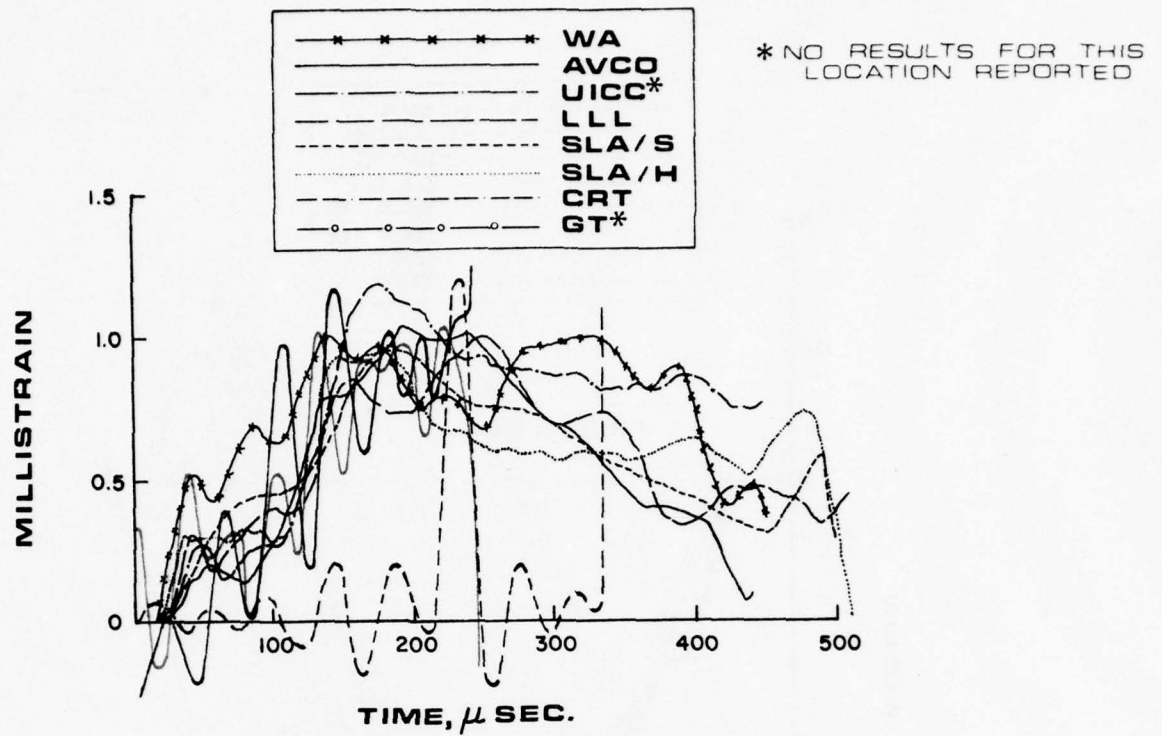
TEST 1 ——— 0°



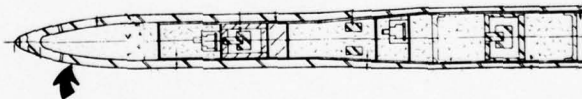
RADIUS 1.30 IN. ON OUTSIDE SURFACE OF CASE

COMPARISON OF THEORETICAL RESULTS WITH A TYPICAL
EXPERIMENTAL TEST AT STATION 4, HOOP

FIG. 20



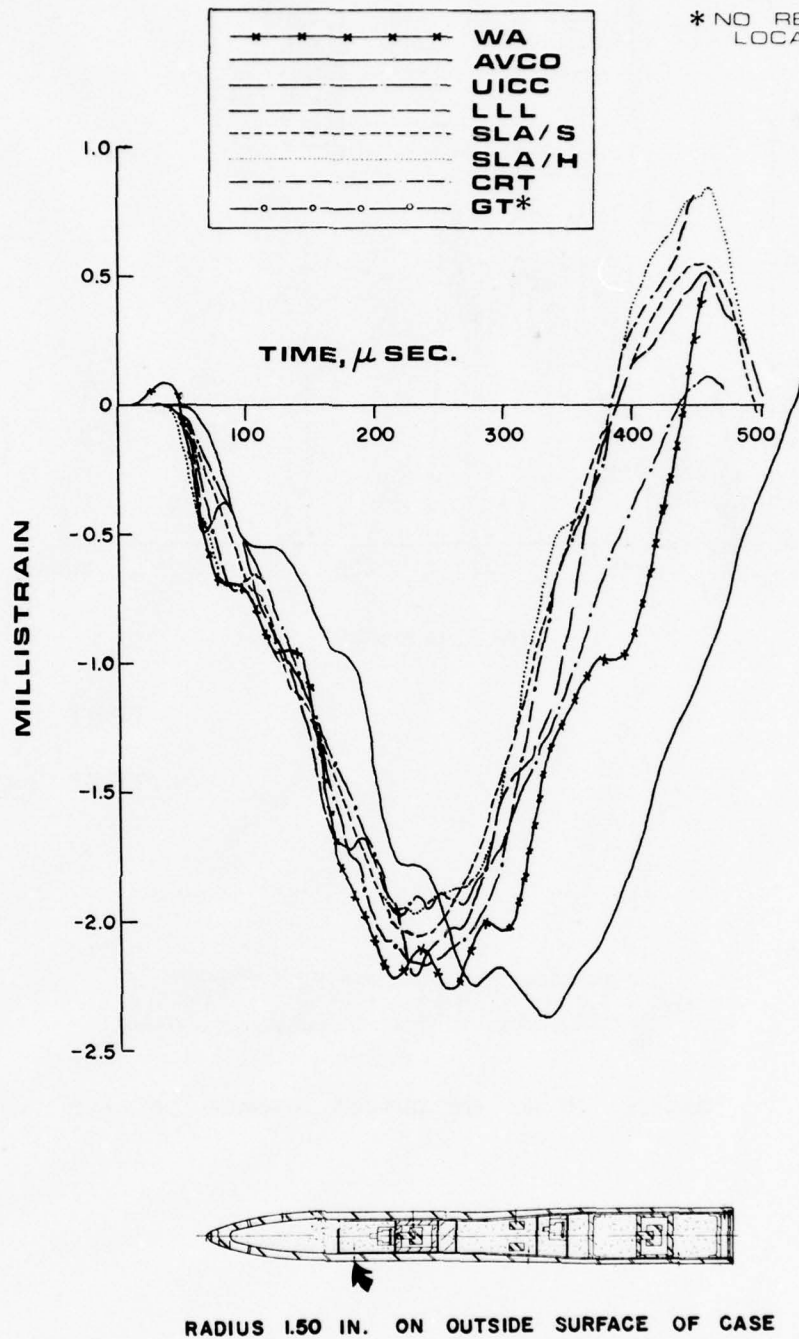
TEST 1 ——— 0°
 TEST 2 ——— 0°
 - - - 180°



RADIUS 1.30 IN. ON OUTSIDE SURFACE OF CASE

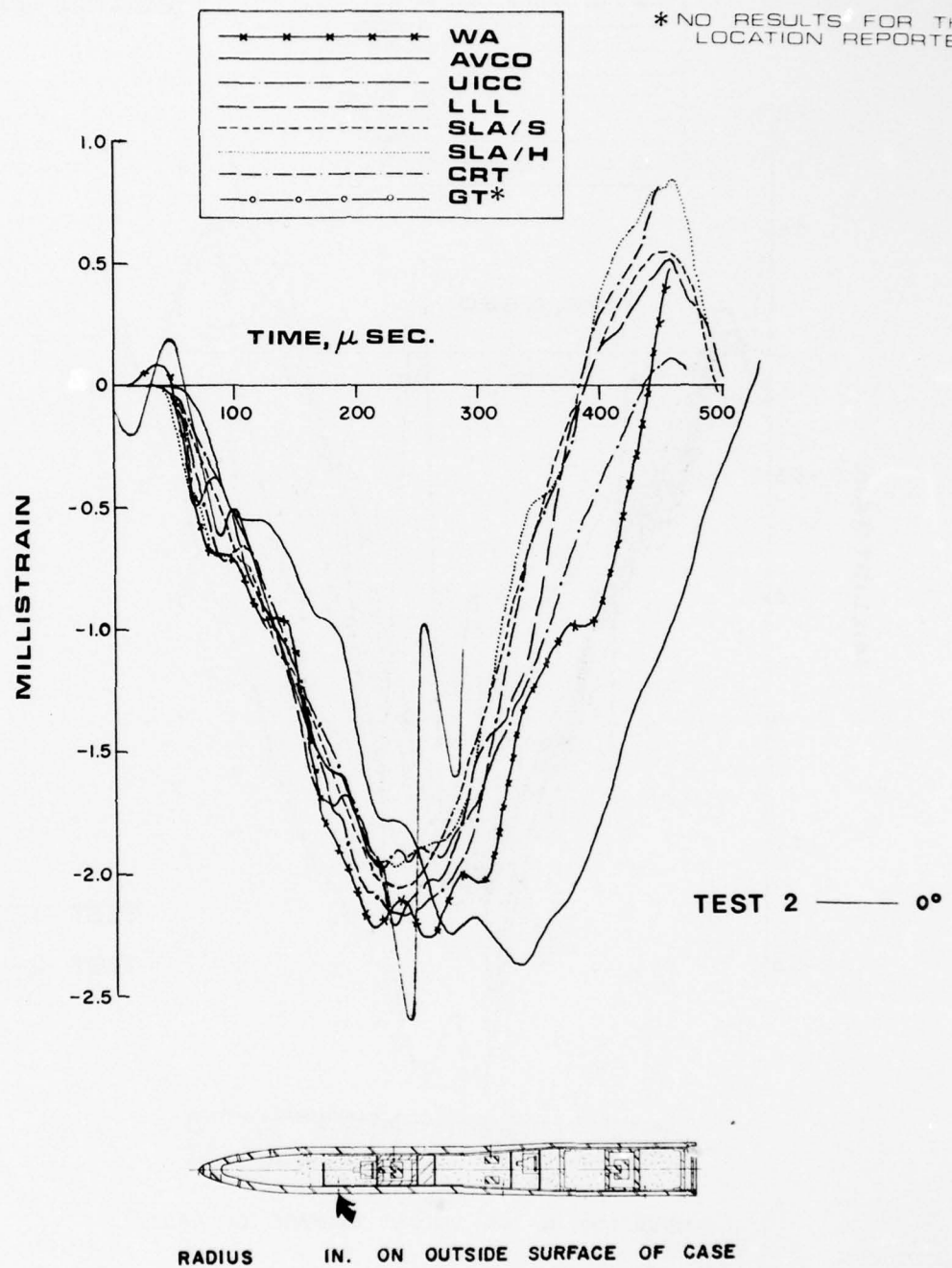
COMPARISON OF THEORETICAL RESULTS WITH EXPERIMENTAL
 TEST 1 & 2 (0° & 180°) AT STATION 4, HOOP

FIG. 21



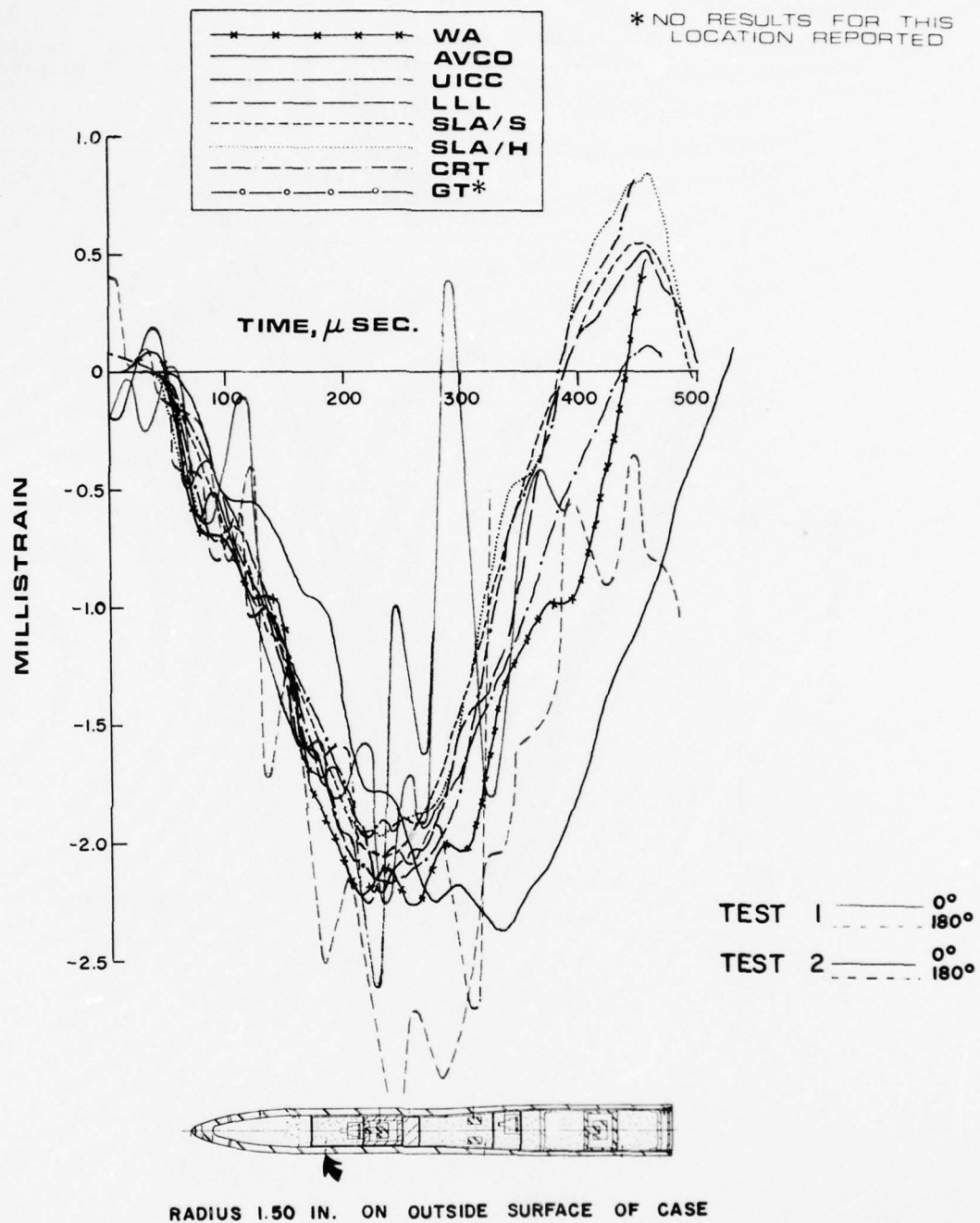
COMPARISON OF THEORETICAL RESULTS AT STATION 9, AXIAL

FIG. 22



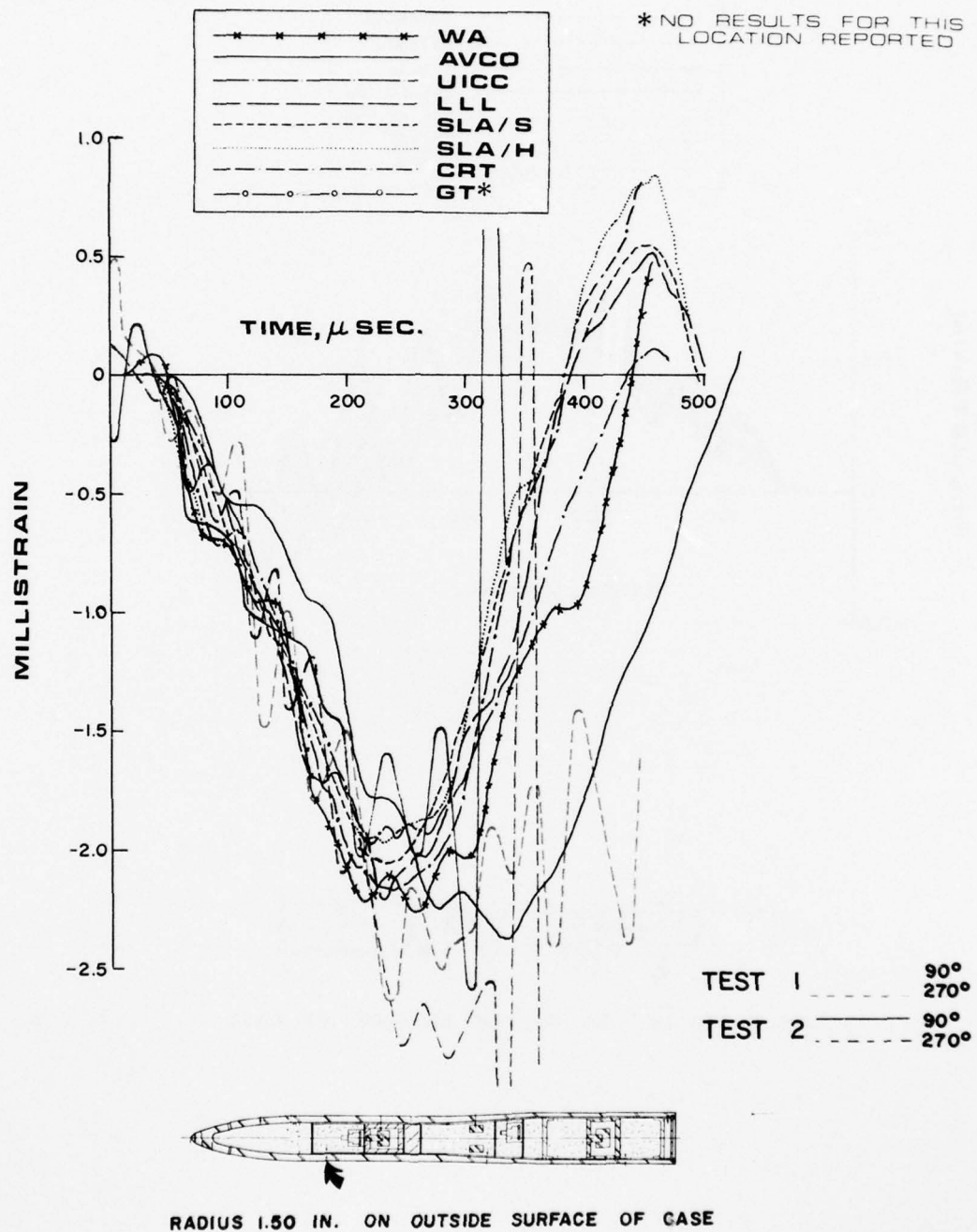
COMPARISON OF THEORETICAL RESULTS WITH A TYPICAL
EXPERIMENTAL TEST AT STATION 9, AXIAL

FIG. 23



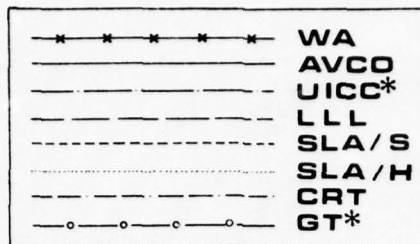
COMPARISON OF THEORETICAL RESULTS WITH EXPERIMENTAL
TESTS 1 & 2 (0° AND 180°) AT STATION 9, AXIAL

FIG. 24

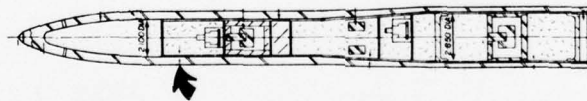
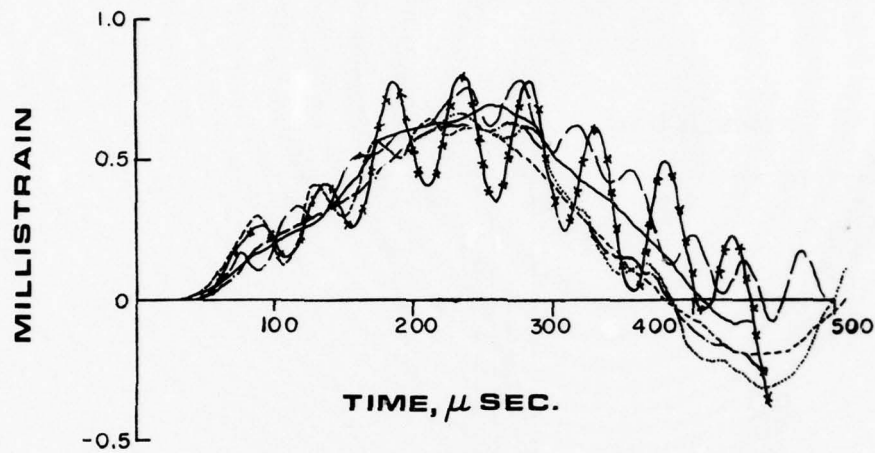


COMPARISON OF THEORETICAL RESULTS WITH EXPERIMENTAL TESTS 1 AND 2 (90° & 270°) AT STATION 9, AXIAL

FIG. 25



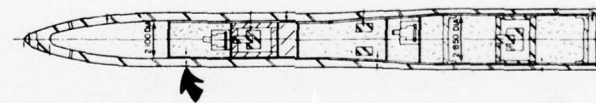
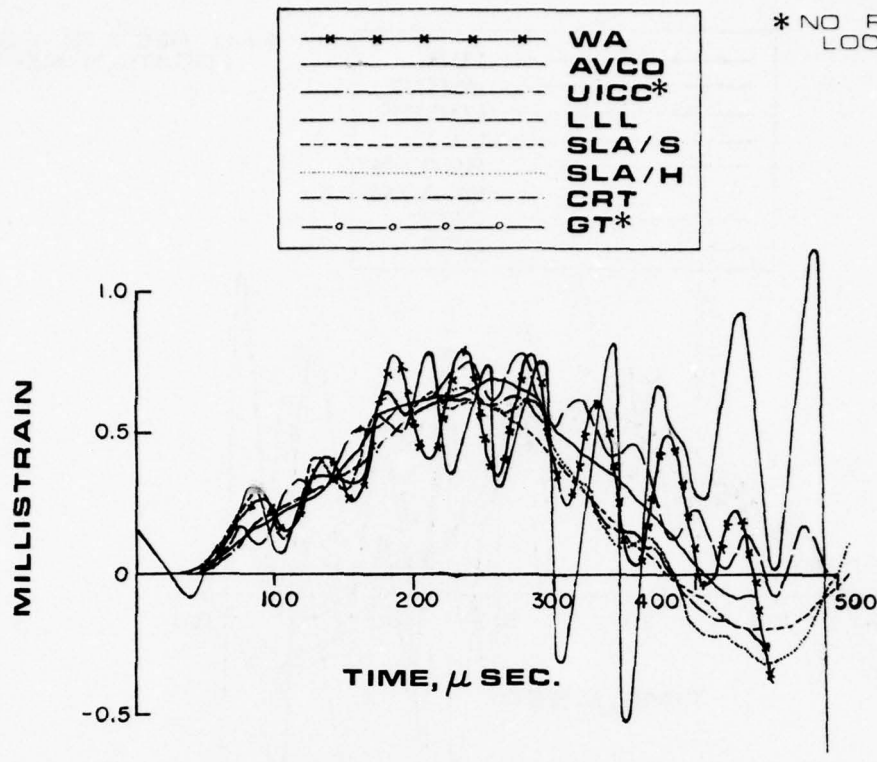
* NO RESULTS FOR THIS
LOCATION REPORTED



RADIUS 1.50 IN. ON OUTSIDE SURFACE OF CASE

COMPARISON OF THEORETICAL RESULTS AT STATION 9, HOOP

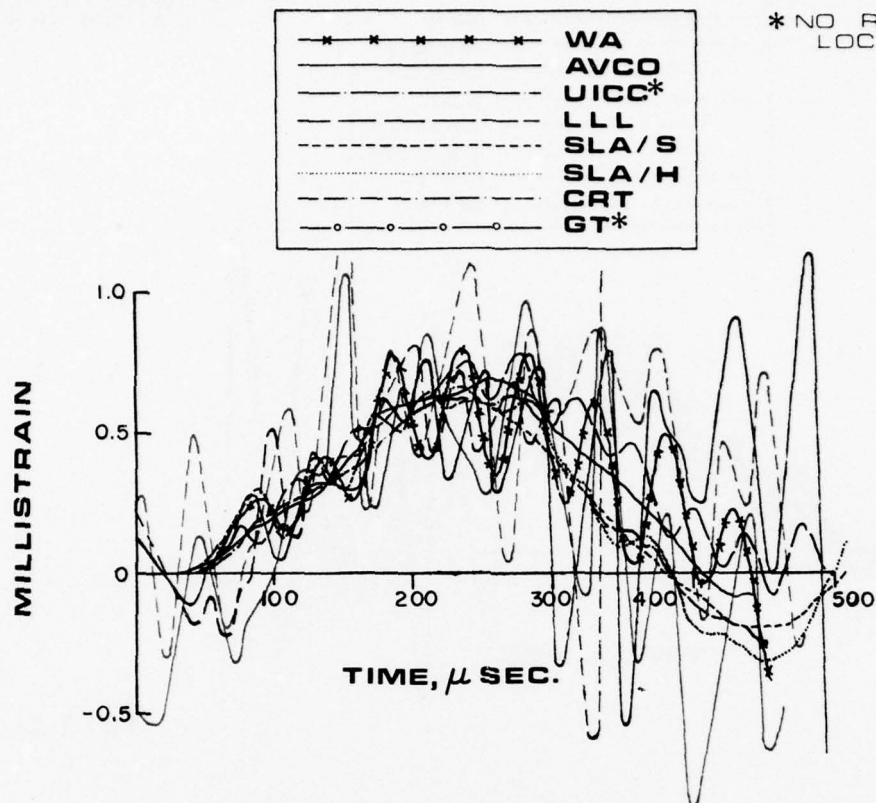
FIG. 26



RADIUS 1.50 IN. ON OUTSIDE SURFACE OF CASE

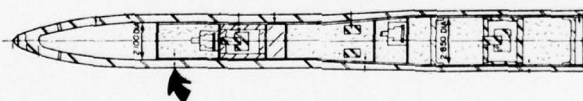
COMPARISON OF THEORETICAL RESULTS WITH A TYPICAL
EXPERIMENTAL TEST AT STATION 9, HOOP

FIG. 27



TEST 1 ——— 0°
 TEST 1 - - - 180°

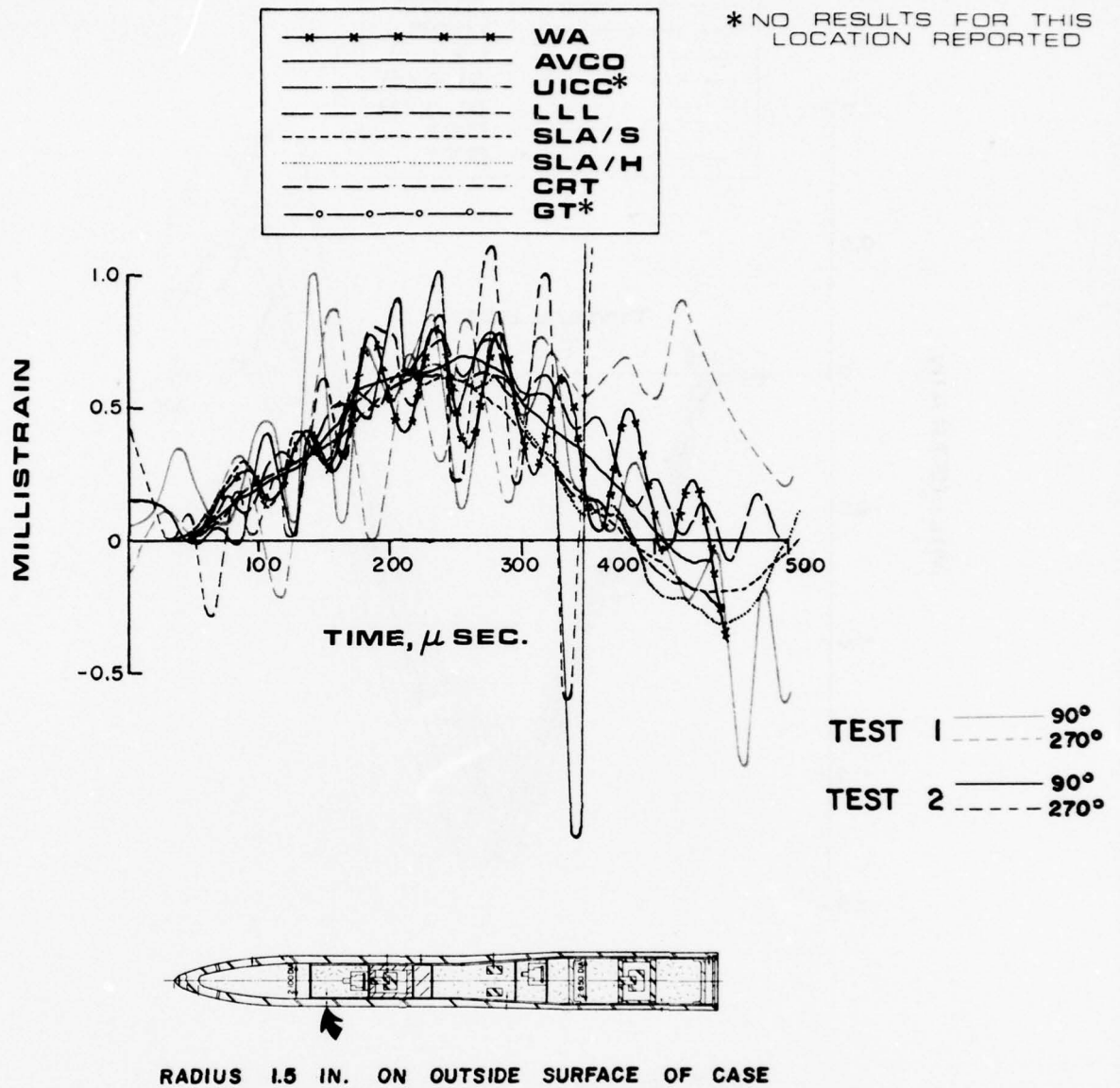
TEST 2 ——— 0°
 TEST 2 - - - 180°



RADIUS 1.50 IN. ON OUTSIDE SURFACE OF CASE

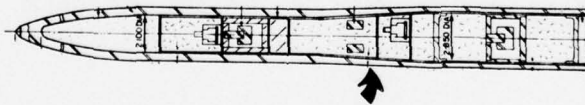
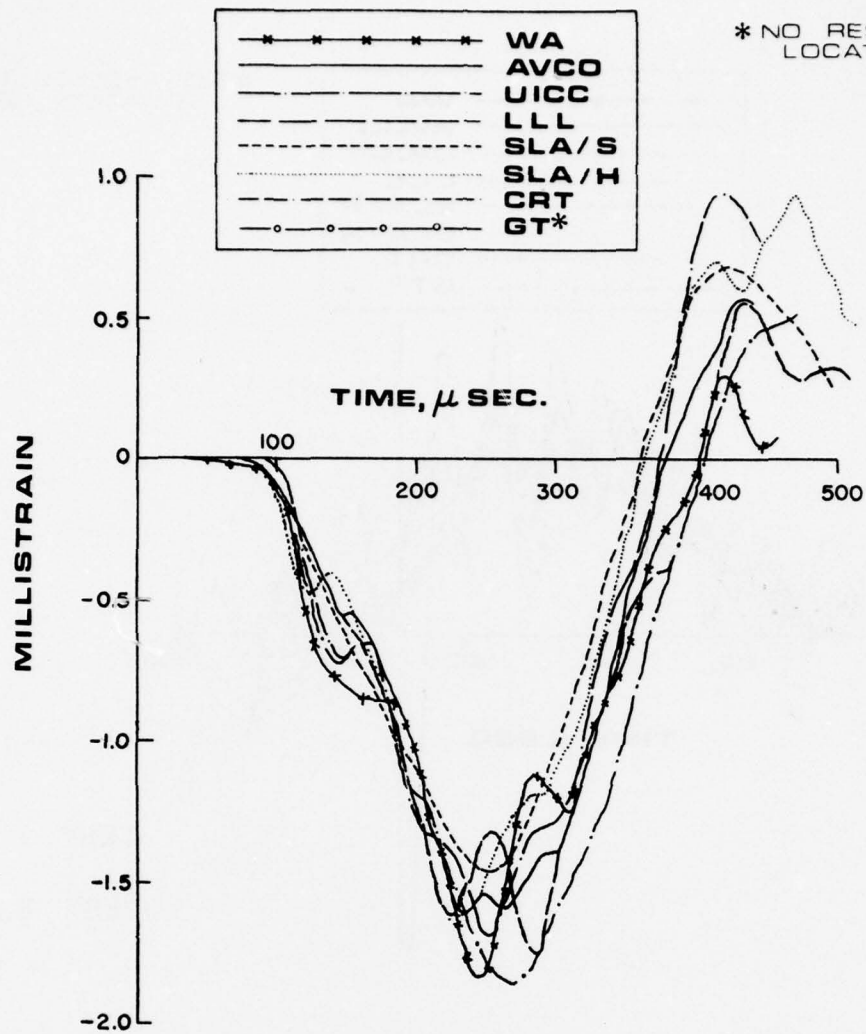
COMPARISON OF THEORETICAL RESULTS WITH EXPERIMENTAL
 TESTS 1 & 2 (0° AND 180°) AT STATION 9, HOOP

FIG. 28



COMPARISON OF THEORETICAL RESULTS WITH EXPERIMENTAL
TESTS 1 AND 2 (90° & 270°) AT STATION 9, HOOP

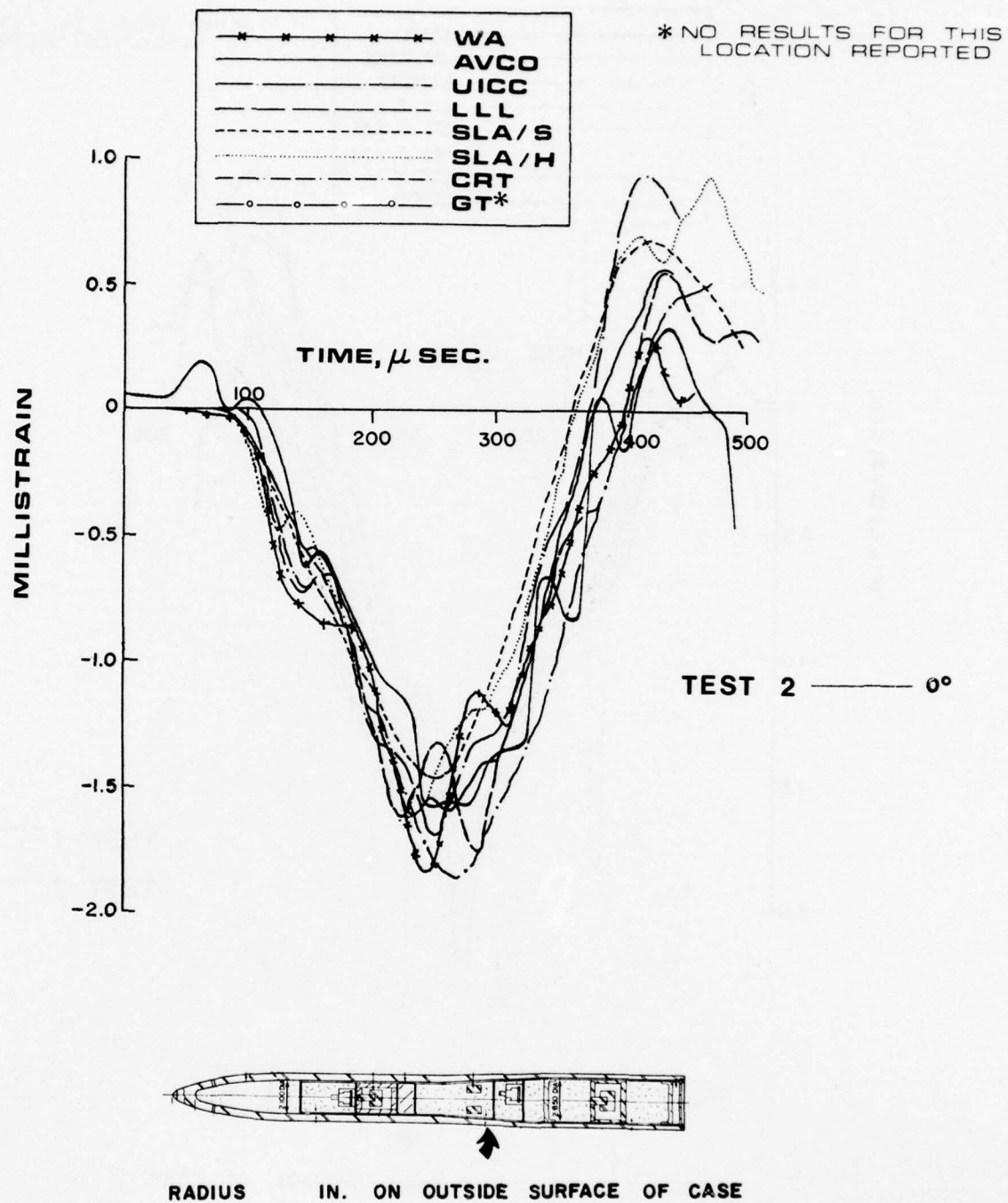
FIG. 29



RADIUS 1.57 IN. ON OUTSIDE SURFACE OF CASE

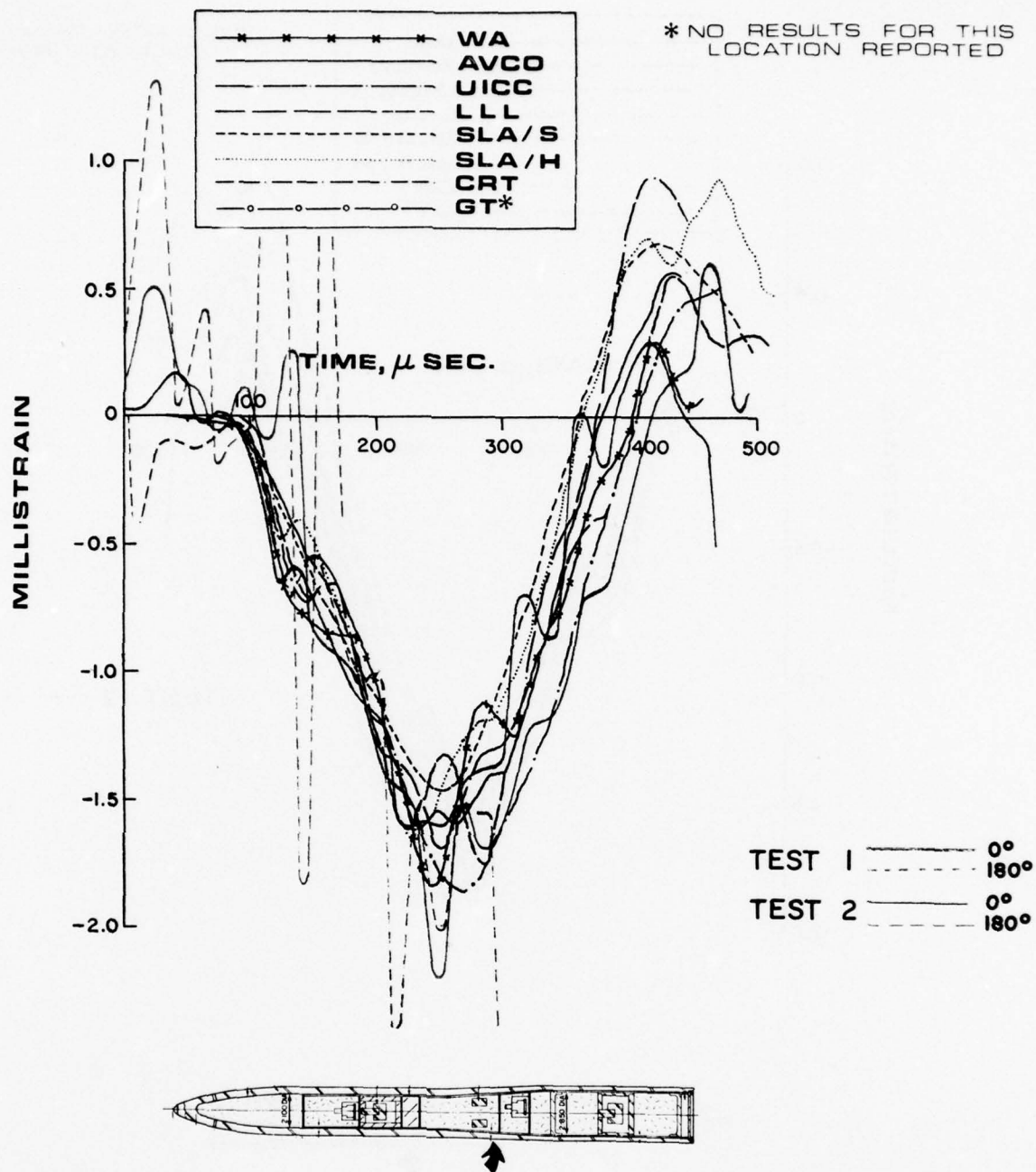
COMPARISON OF THEORETICAL RESULTS AT STATION 19.5
AXIAL

FIG. 30



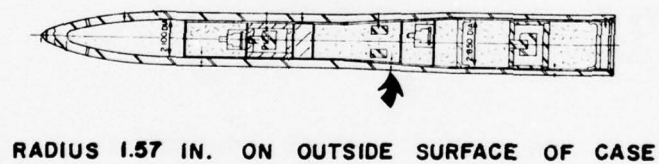
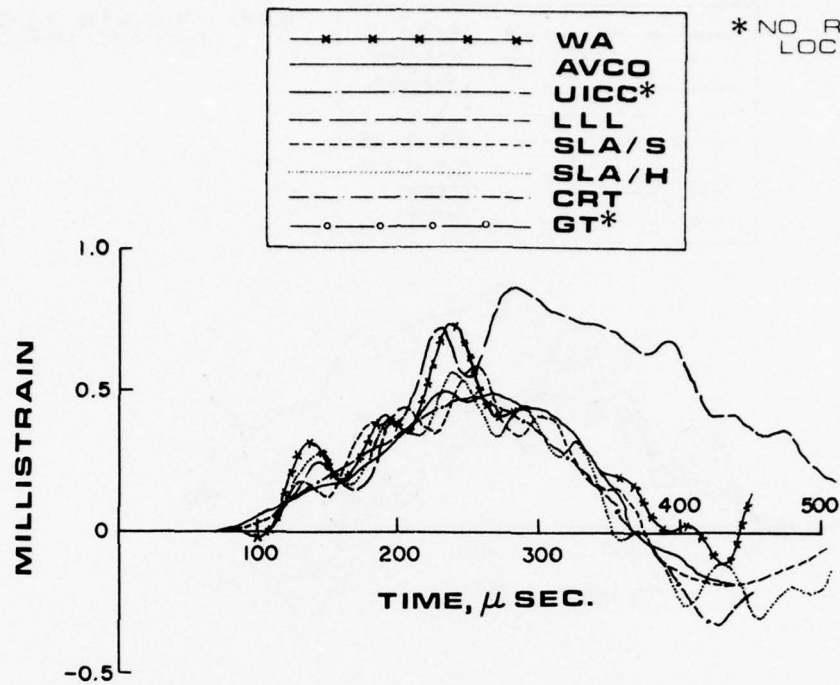
COMPARISON OF THEORETICAL RESULTS WITH A TYPICAL
EXPERIMENTAL TEST AT STATION 19.5 AXIAL

FIG. 31



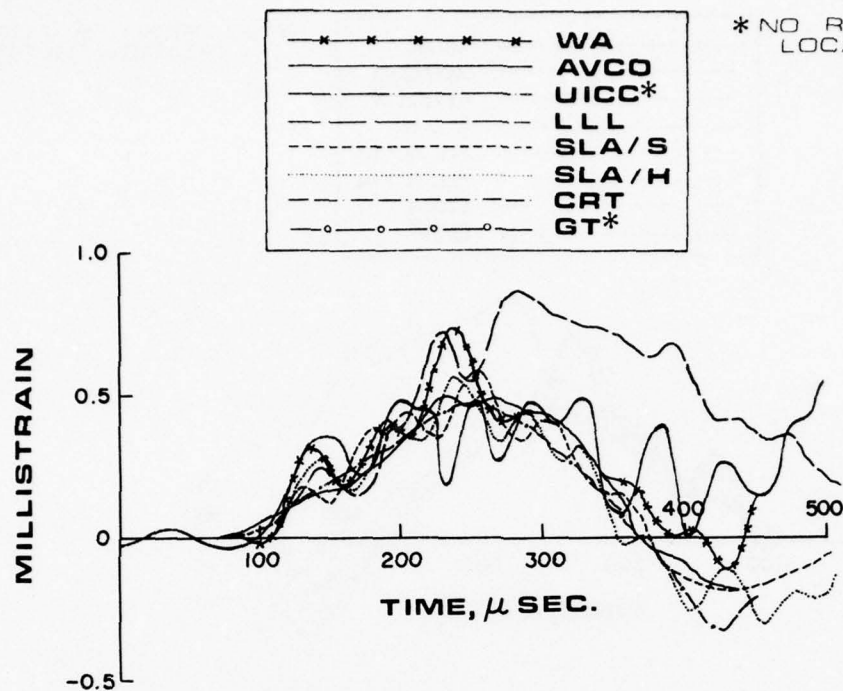
COMPARISON OF THEORETICAL RESULTS WITH EXPERIMENTAL
TESTS 1 & 2 (0° AND 180°) AT STATION 19.5 AXIAL

FIG. 32

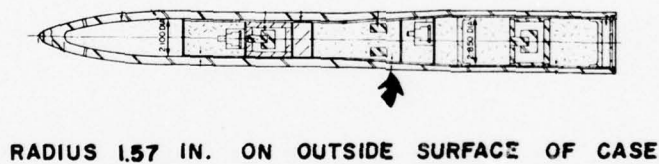


COMPARISON OF THEORETICAL RESULTS AT STATION 19.5, HOOP

FIG. 33

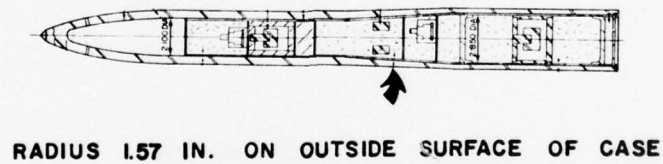
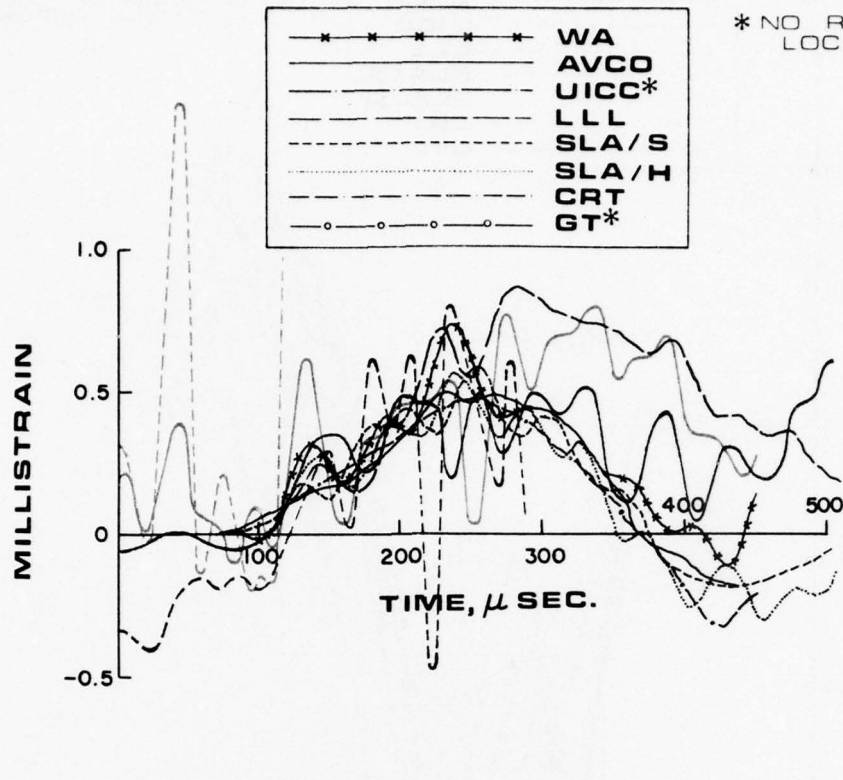


TEST 2 — 0°



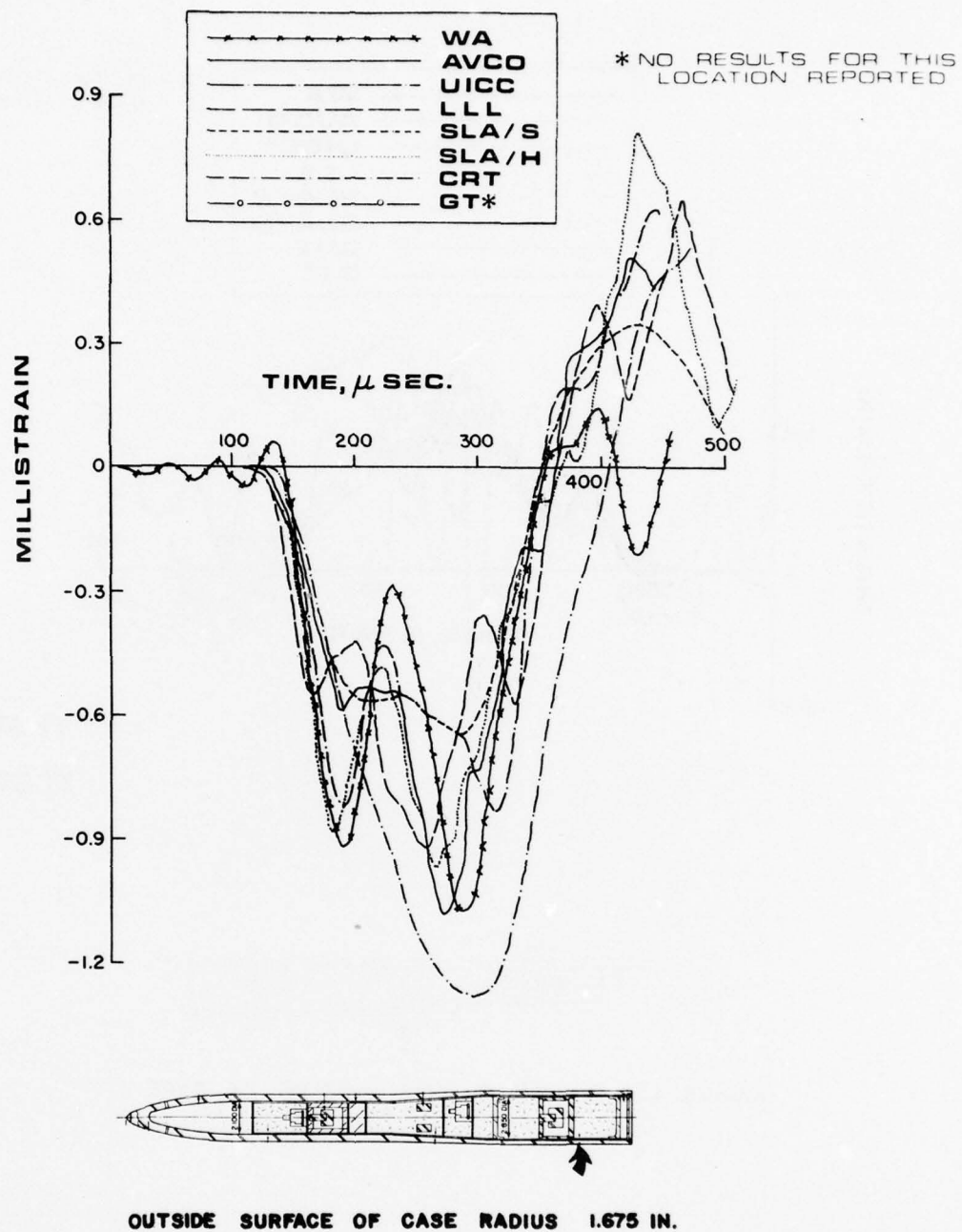
COMPARISON OF THEORETICAL RESULTS WITH A TYPICAL
EXPERIMENTAL TEST AT STATION 19.5, HOOP

FIG. 34



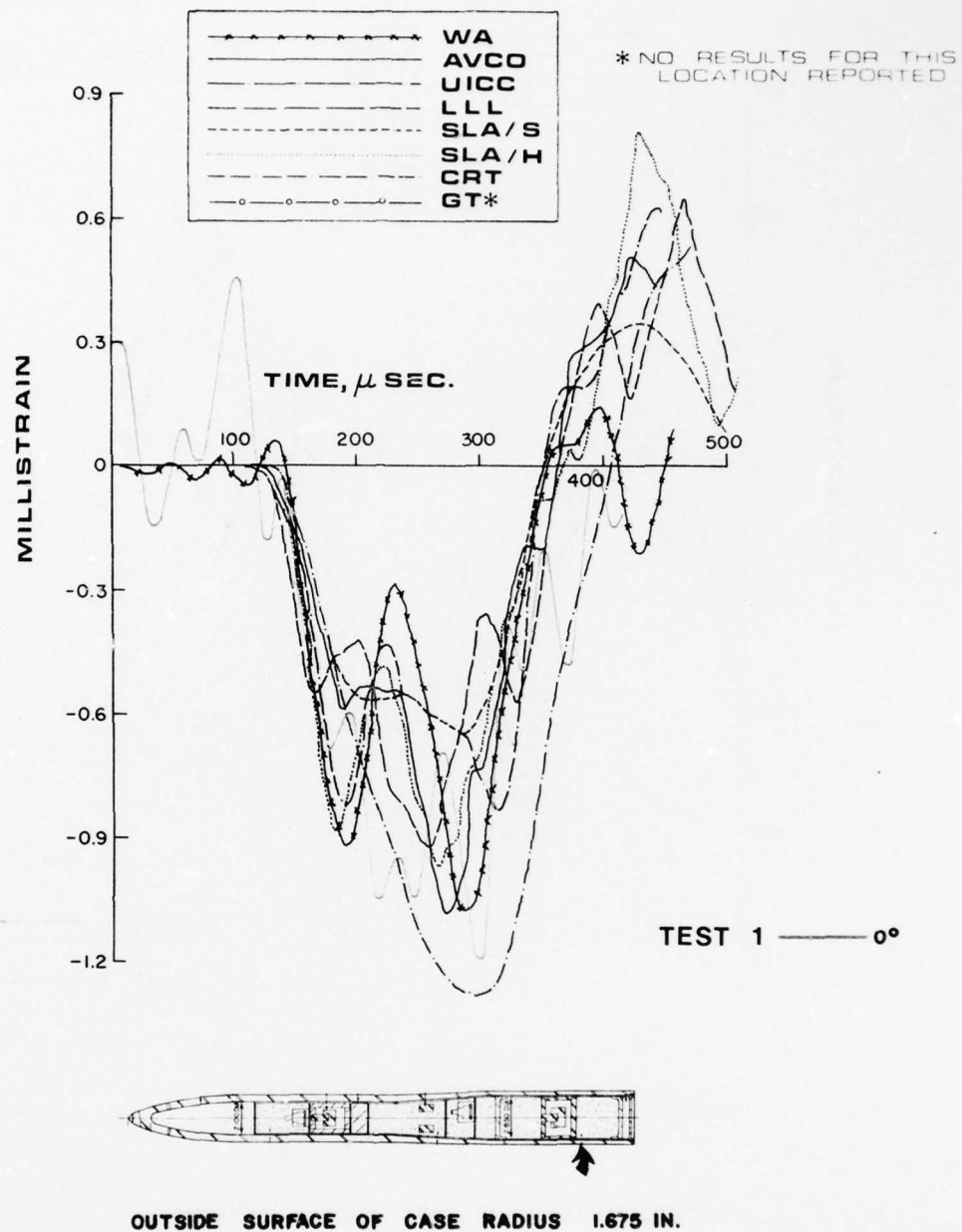
COMPARISON OF THEORETICAL RESULTS WITH EXPERIMENTAL
TESTS 1 & 2 (0° AND 180°) AT STATION 19.5, HOOP

FIG. 35



COMPARISON OF THEORETICAL RESULTS AT STATION 27.3 AXIAL

FIG. 36



COMPARISON OF THEORETICAL RESULTS WITH A TYPICAL
EXPERIMENTAL TEST AT STATION 27.3, AXIAL

FIG. 37

AD-A058 364

WEIDLINGER ASSOCIATES NEW YORK

F/G 19/4

COMPARISON OF PRE-SHOT RESPONSE PREDICTIONS WITH AVCO REVERSE B--ETC(U)

NOV 77 J M MCCORMICK

DNA001-76-C-0353

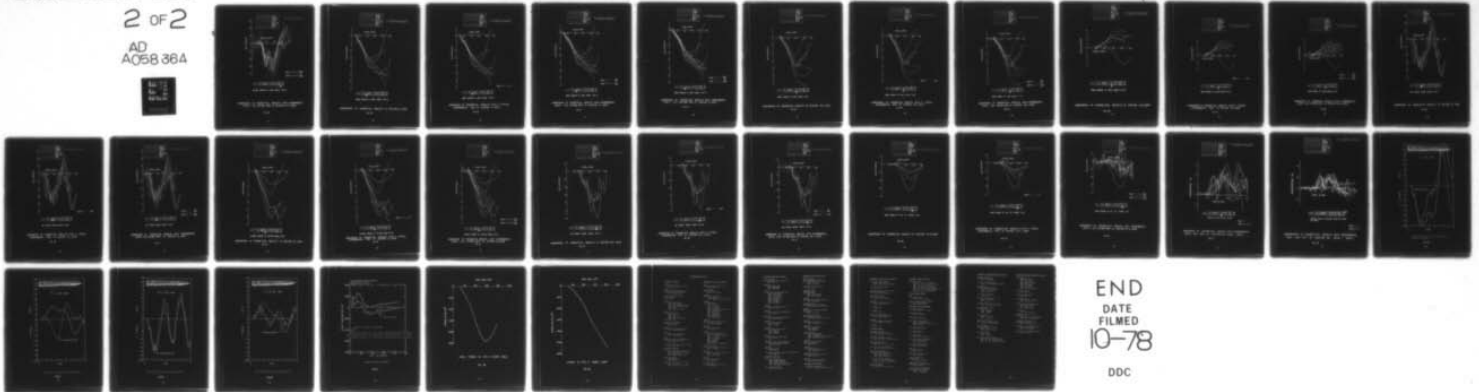
UNCLASSIFIED

DNA-4482T

NL

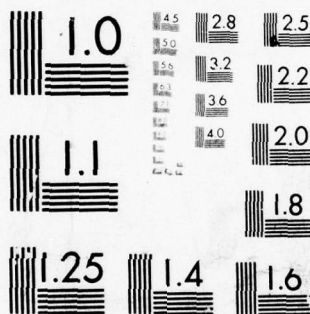
2 OF 2

AD
A058 364

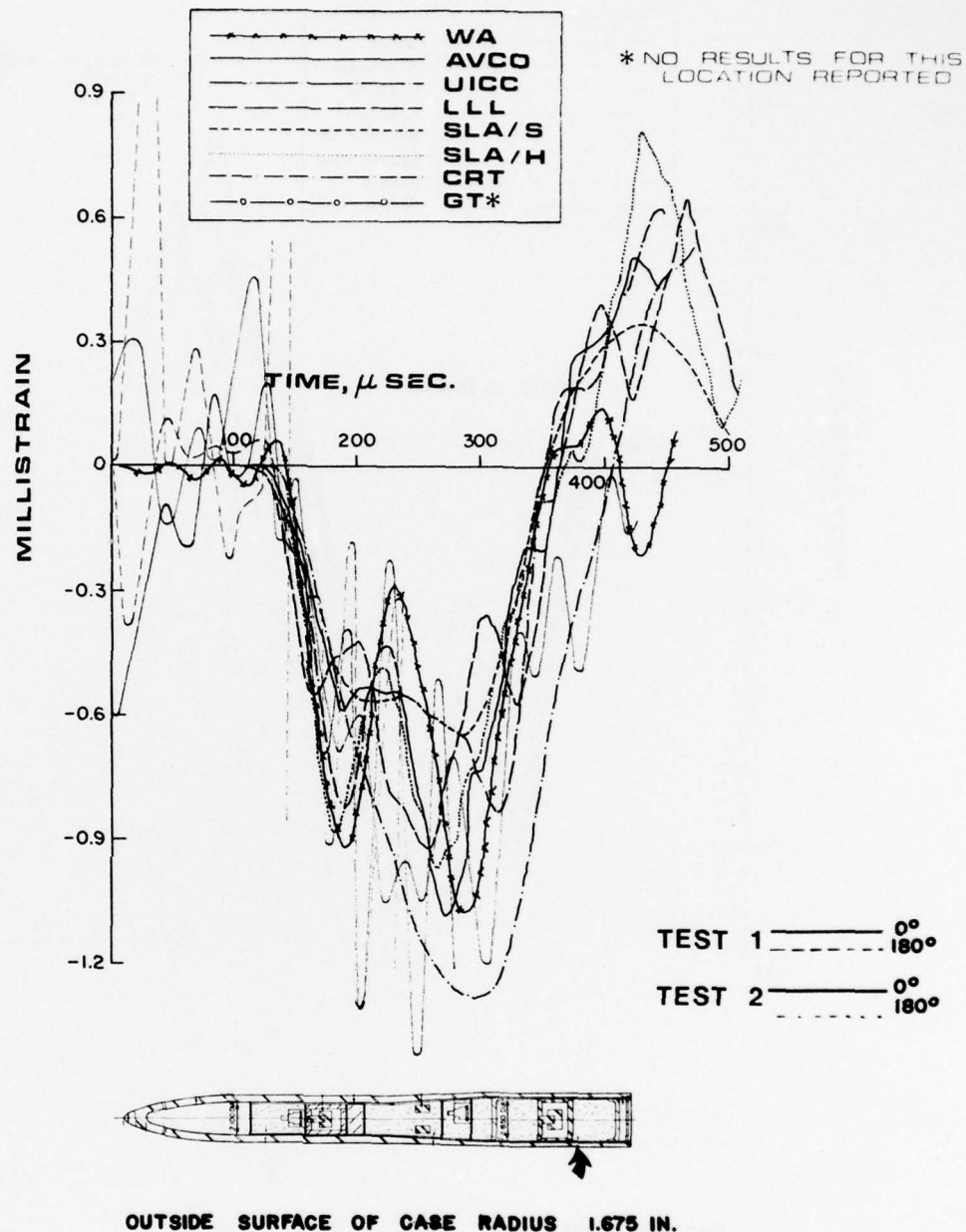


END
DATE
FILMED
10-78

DDC

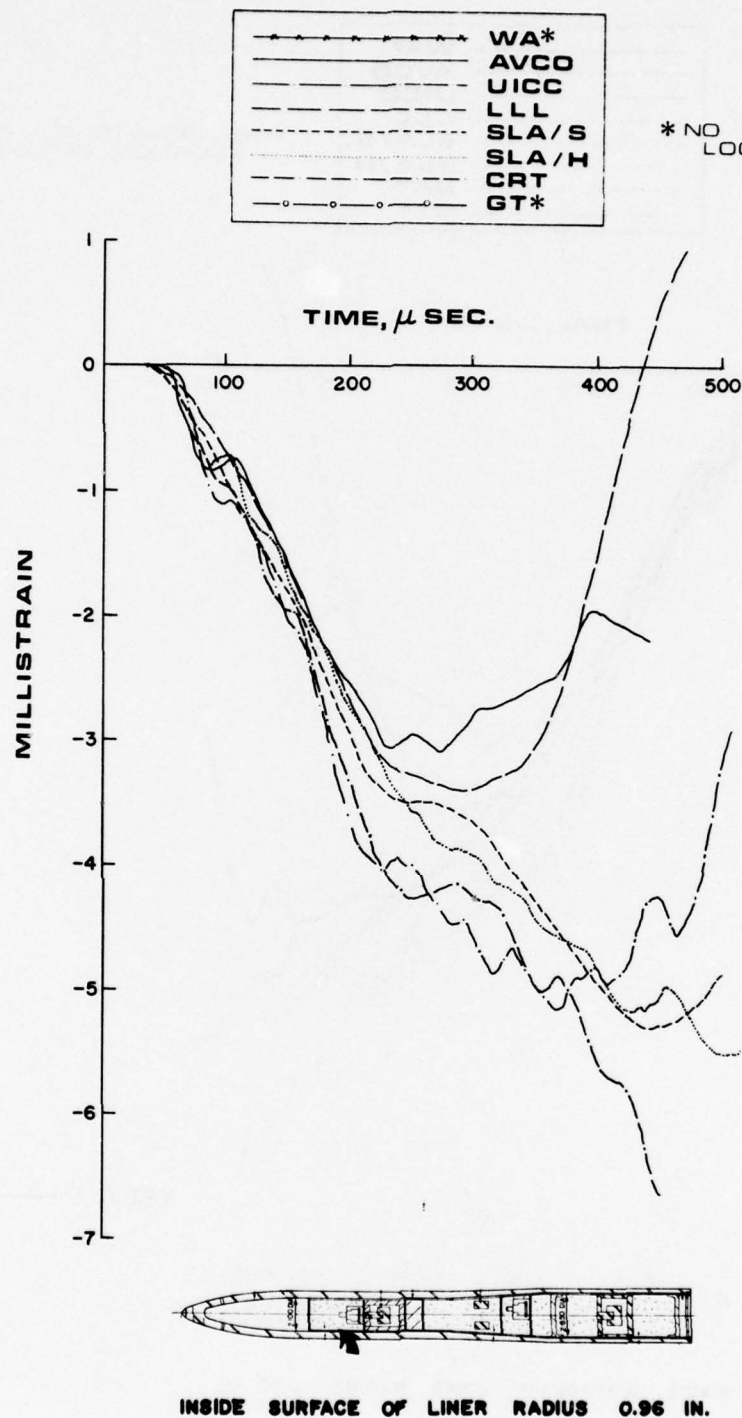


MICROCOPY RESOLUTION TEST CHART
NATIONAL BUREAU OF STANDARDS-1963-A



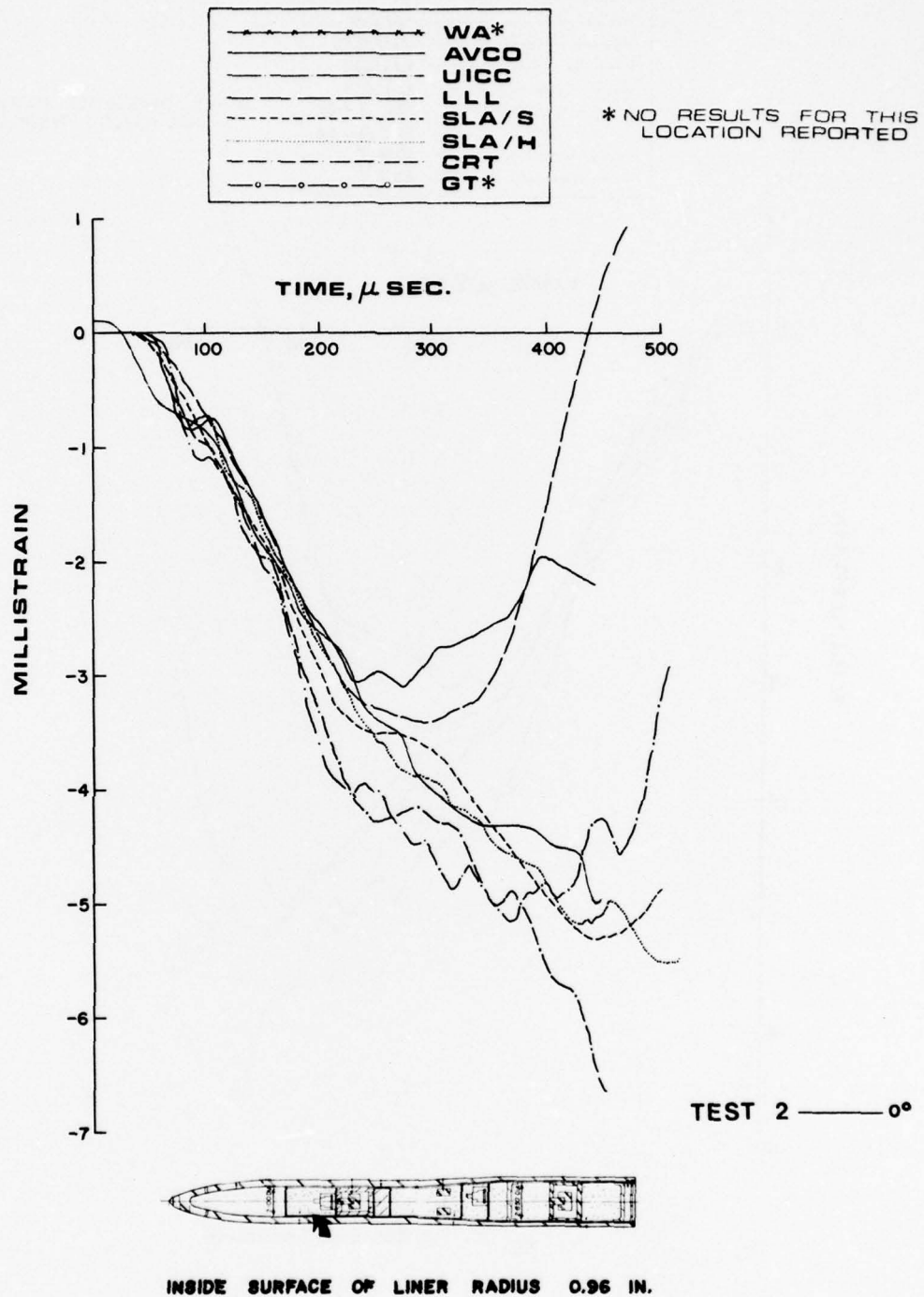
COMPARISON OF THEORETICAL RESULTS WITH EXPERIMENTAL
 TESTS 1 & 2 (0° AND 180°) AT STATION 27.3, AXIAL

FIG. 38



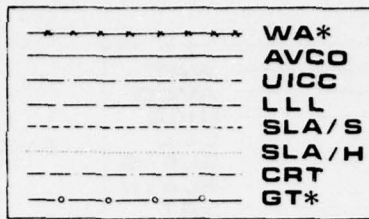
COMPARISONS OF THEORETICAL RESULTS AT STATION 9, AXIAL

FIG. 39

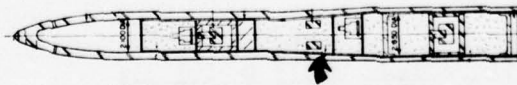
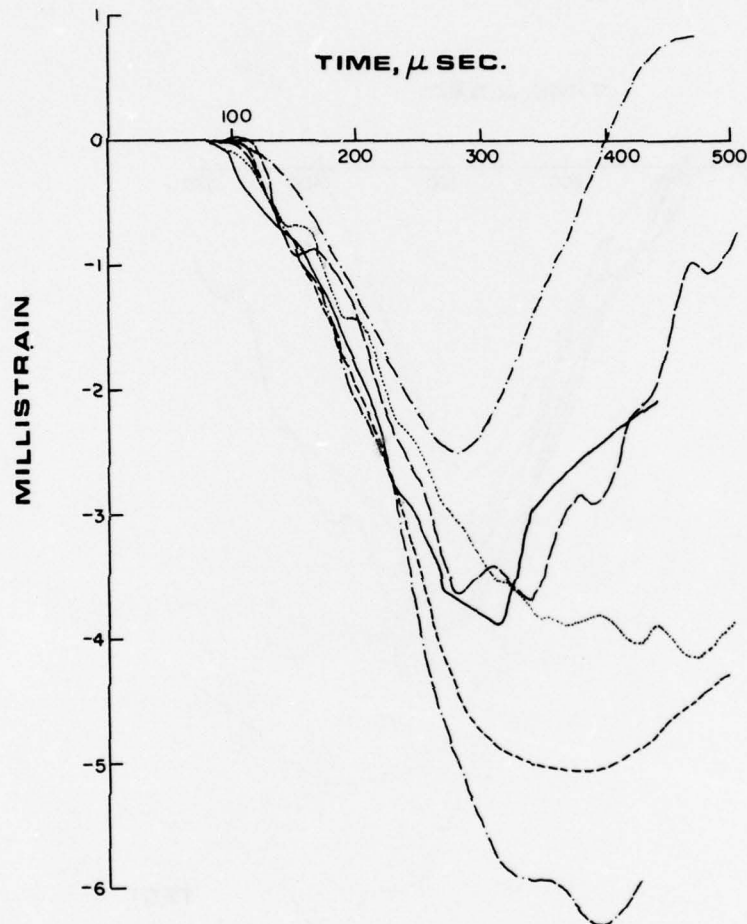


COMPARISON OF THEORETICAL RESULTS WITH A TYPICAL
EXPERIMENTAL TEST AT STATION 9, AXIAL

FIG. 40

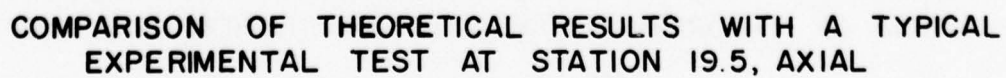


* NO RESULTS FOR THIS LOCATION REPORTED

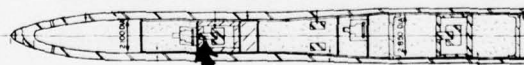
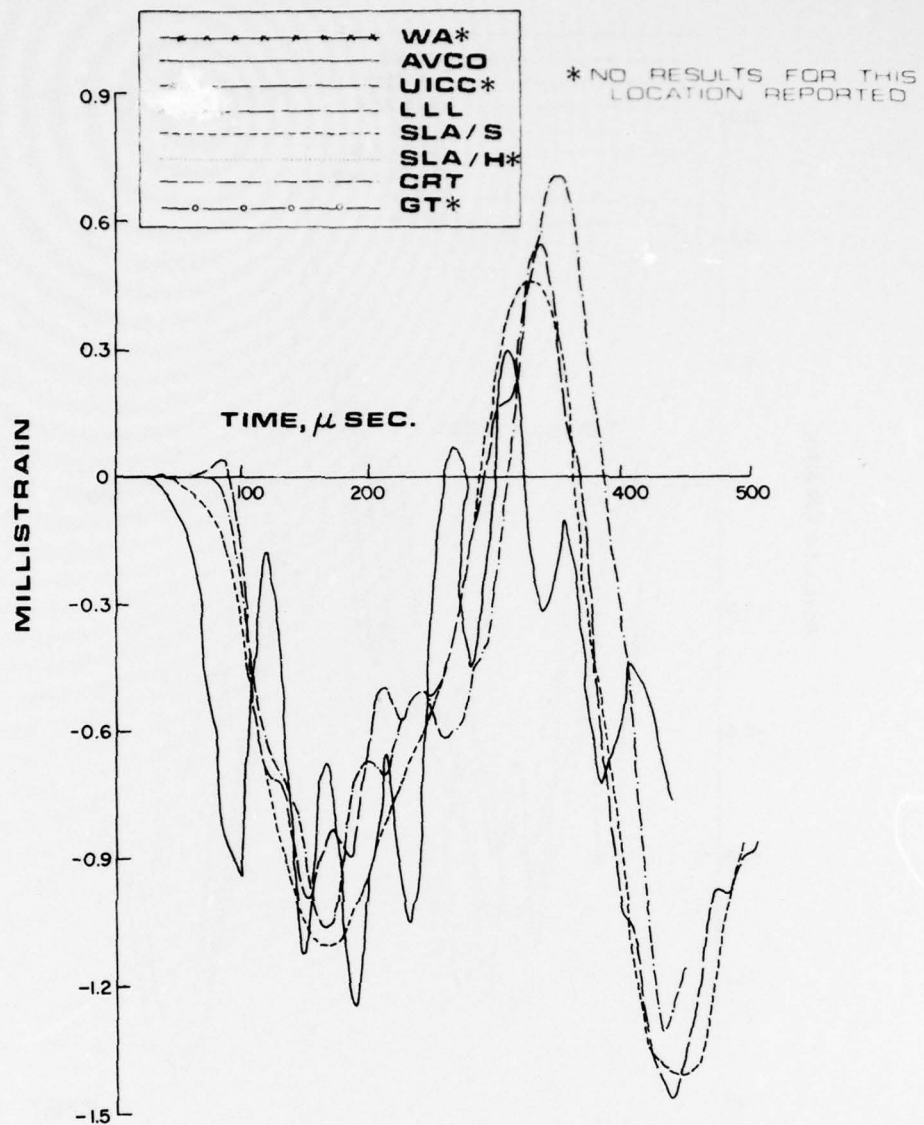


INSIDE SURFACE OF LINER RADIUS 1.10 IN.

COMPARISON OF THEORETICAL RESULTS AT STATION 19.5, AXIAL
FIG. 43



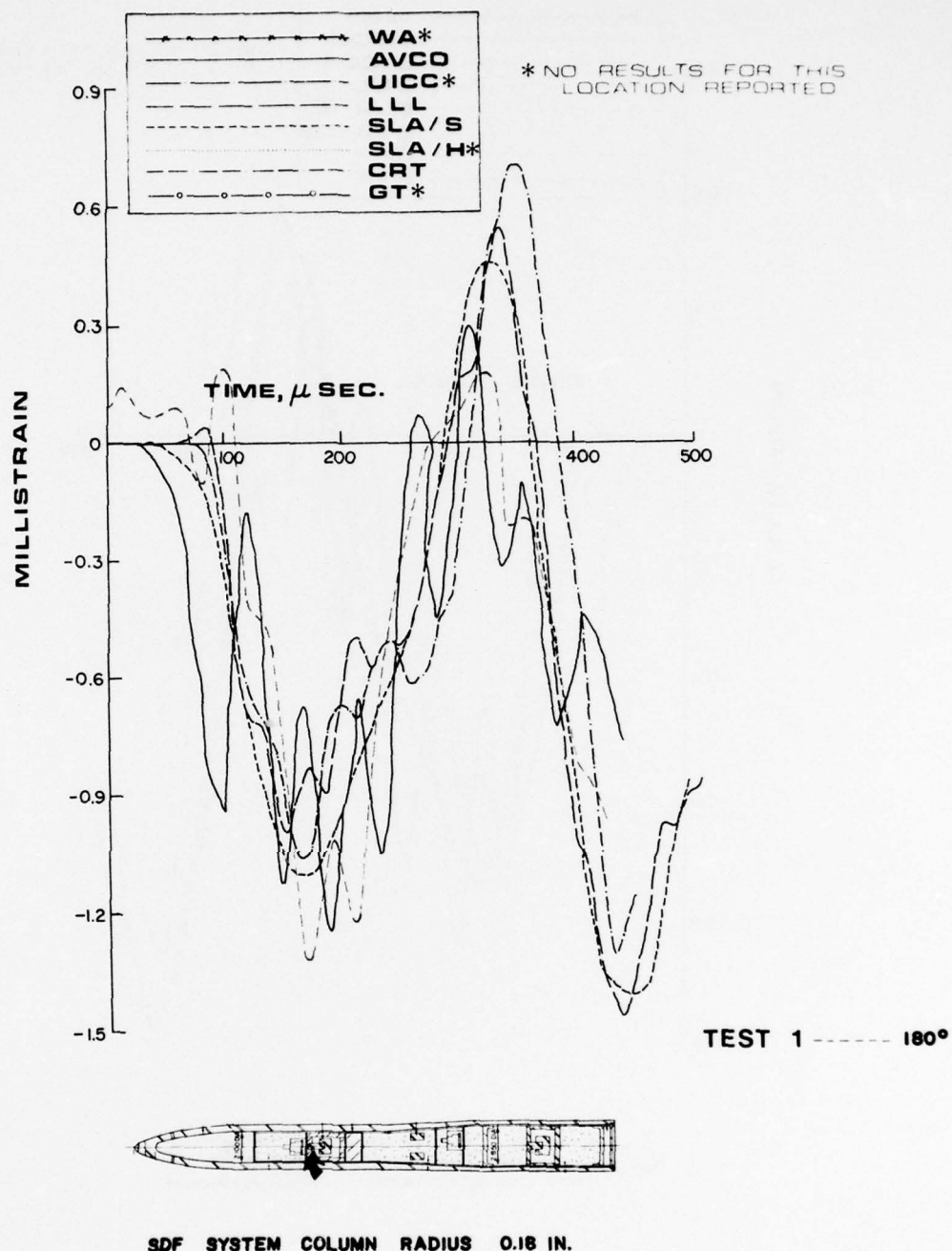
100



SDF SYSTEM COLUMN RADIUS 0.18 IN.

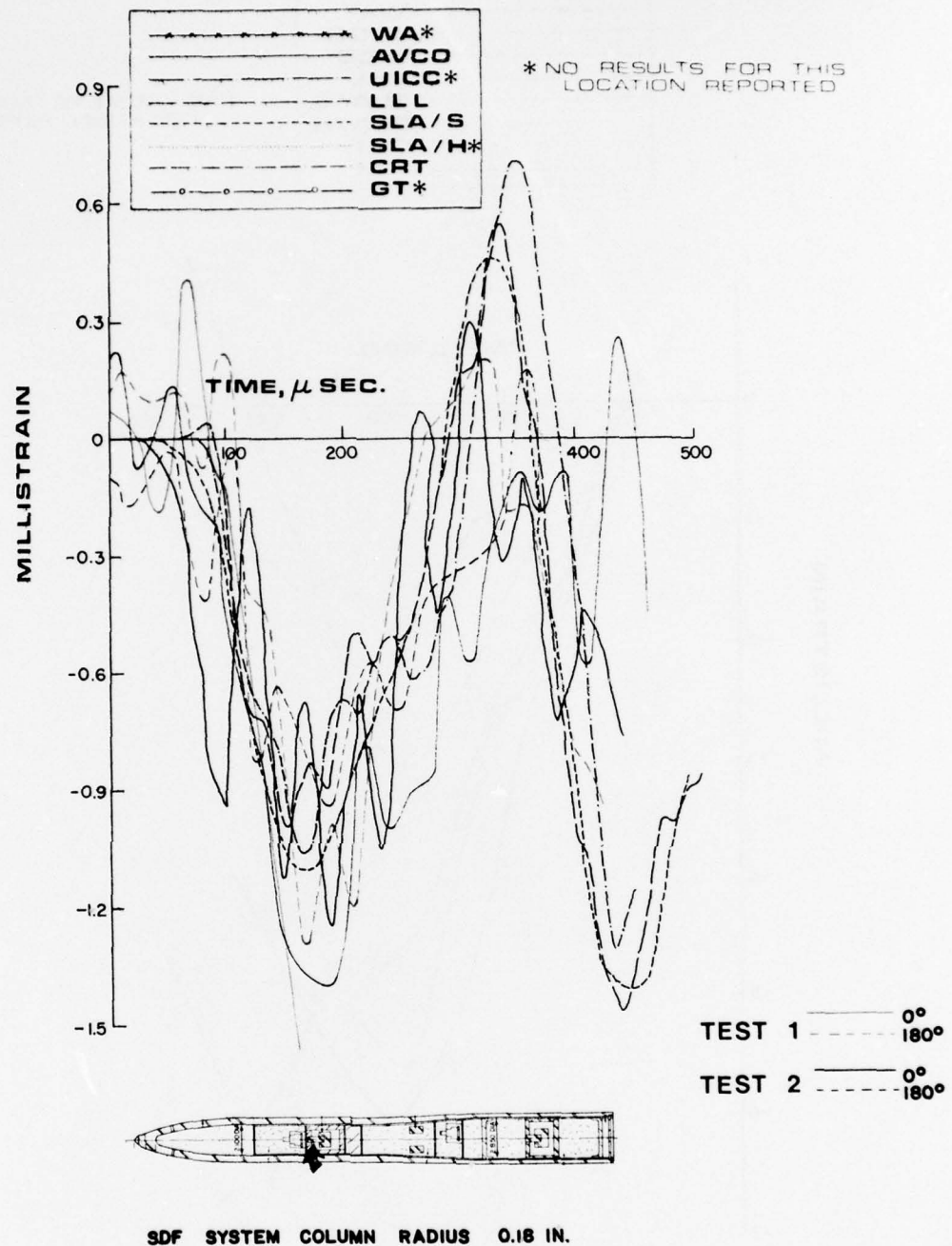
COMPARISON OF THEORETICAL RESULTS AT STATION 12, AXIAL

FIG. 49



COMPARISON OF THEORETICAL RESULTS WITH A TYPICAL
EXPERIMENTAL TEST AT STATION 12, AXIAL

FIG. 50



COMPARISON OF THEORETICAL RESULTS WITH EXPERIMENTAL
TESTS 1 & 2 (0° AND 180°) AT STATION 12, AXIAL

FIG. 51

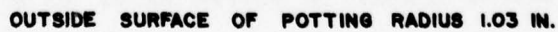
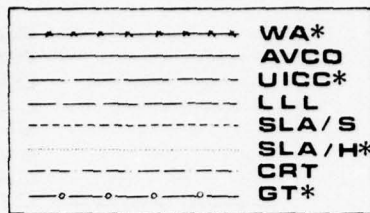
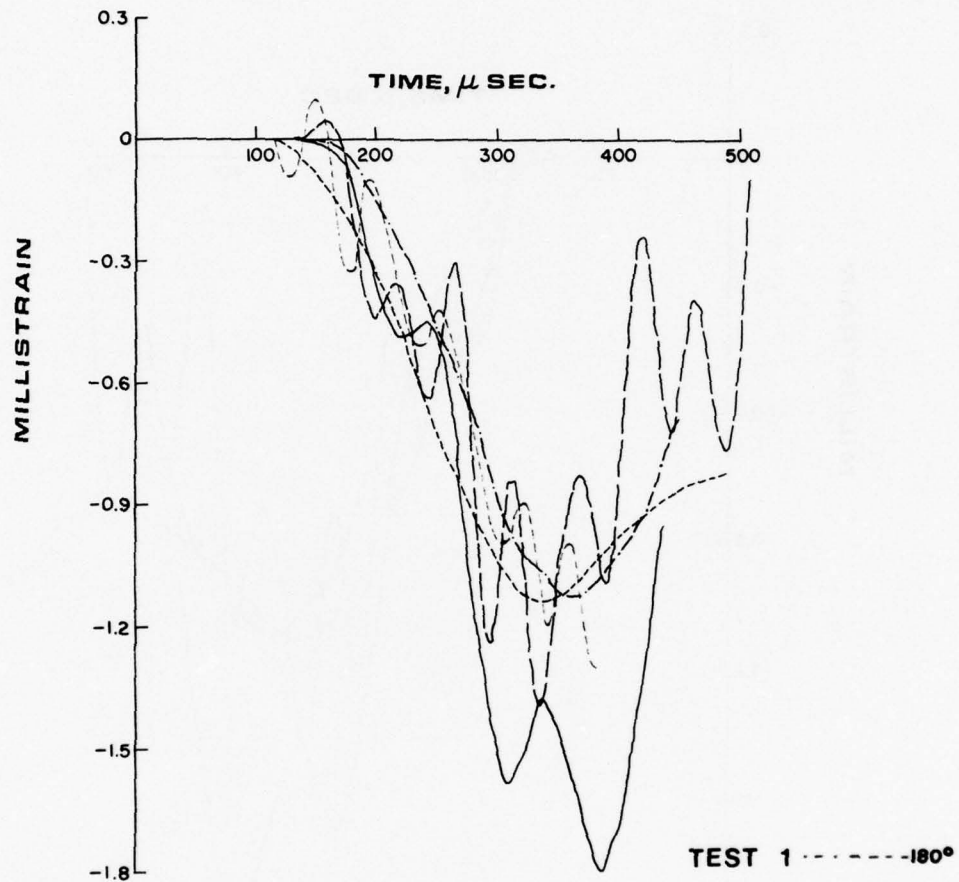


FIG. 53



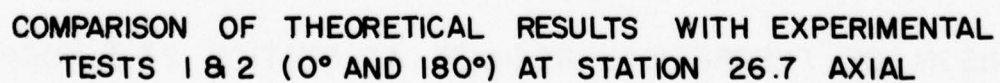
* NO RESULTS FOR THIS LOCATION REPORTED



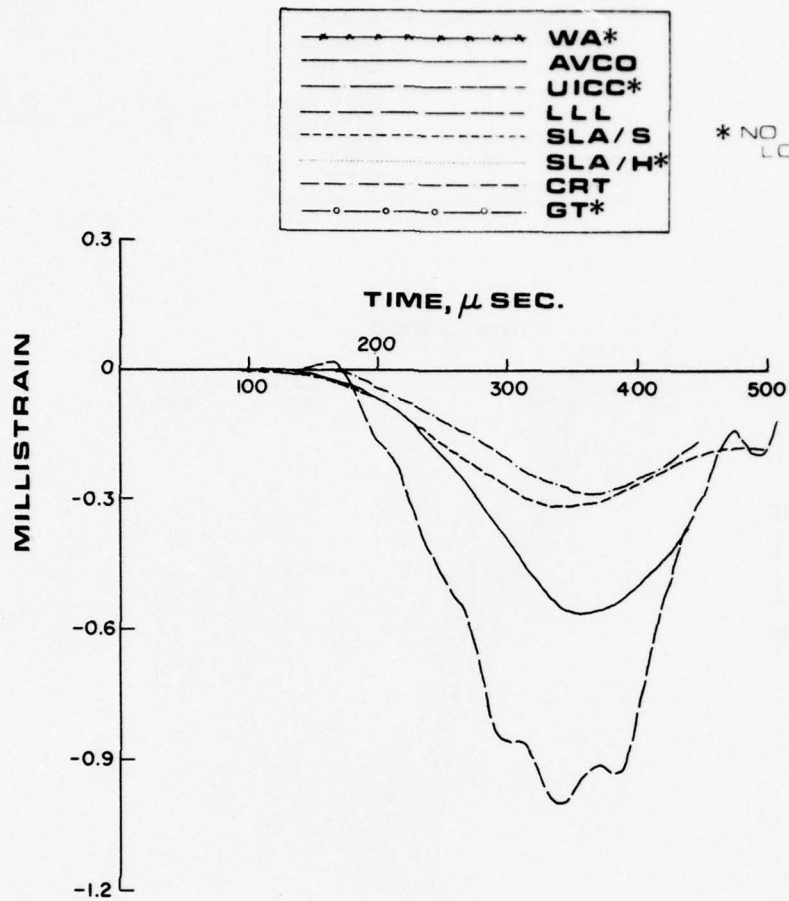
SDF SYSTEM COLUMN RADIUS 0.19 IN.

COMPARISON OF THEORETICAL RESULTS WITH A TYPICAL
EXPERIMENTAL TEST AT STATION 26.7, AXIAL

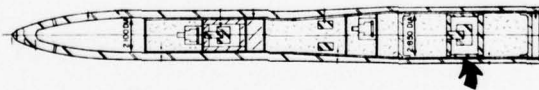
FIG. 56



113



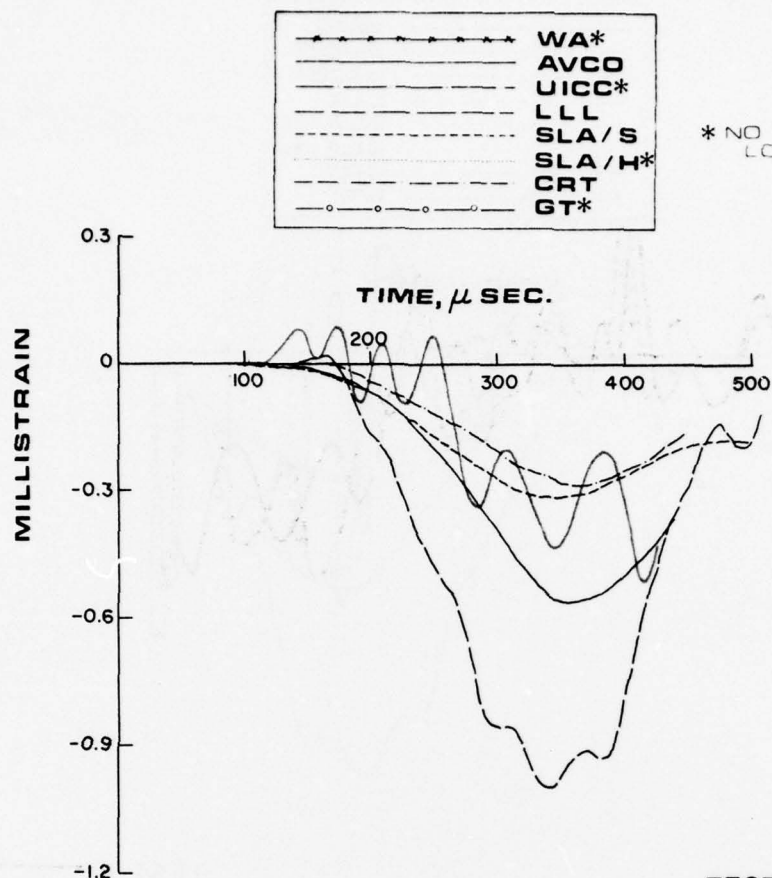
* NO RESULTS FOR THIS LOCATION REPORTED



INSIDE SURFACE OF STL. CYL. RADIUS 1.15 IN.

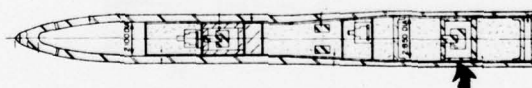
COMPARISON OF THEORETICAL RESULTS AT STATION 27.3, HOOP

FIG. 58



* NO RESULTS FOR THIS LOCATION REPORTED

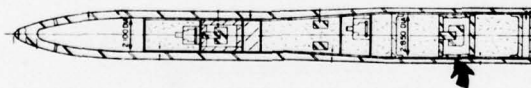
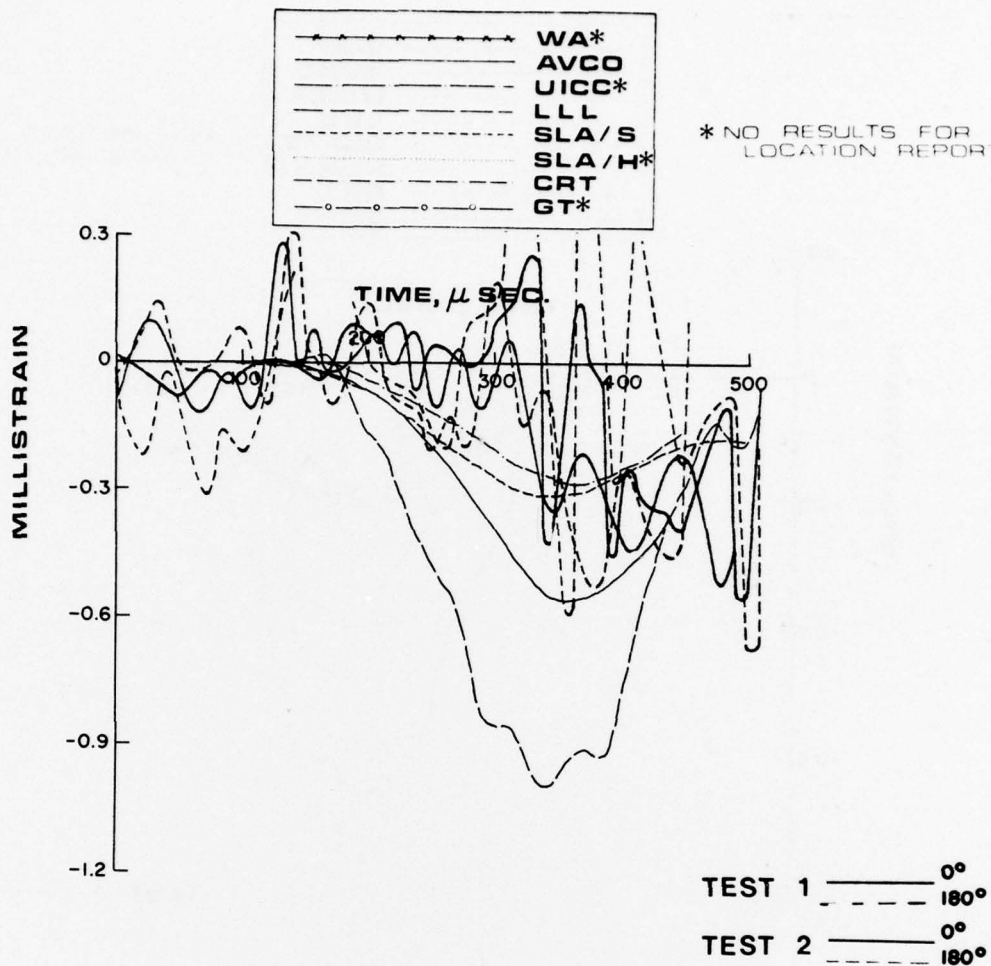
TEST 1 — 0°



INSIDE SURFACE OF STL. CYL. RADIUS 1.15 IN.

COMPARISON OF THEORETICAL RESULTS WITH A TYPICAL
EXPERIMENTAL TEST AT STATION 27.3, HOOP

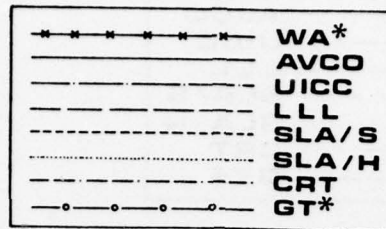
FIG. 59



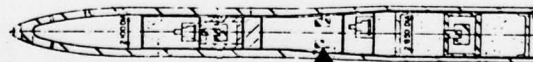
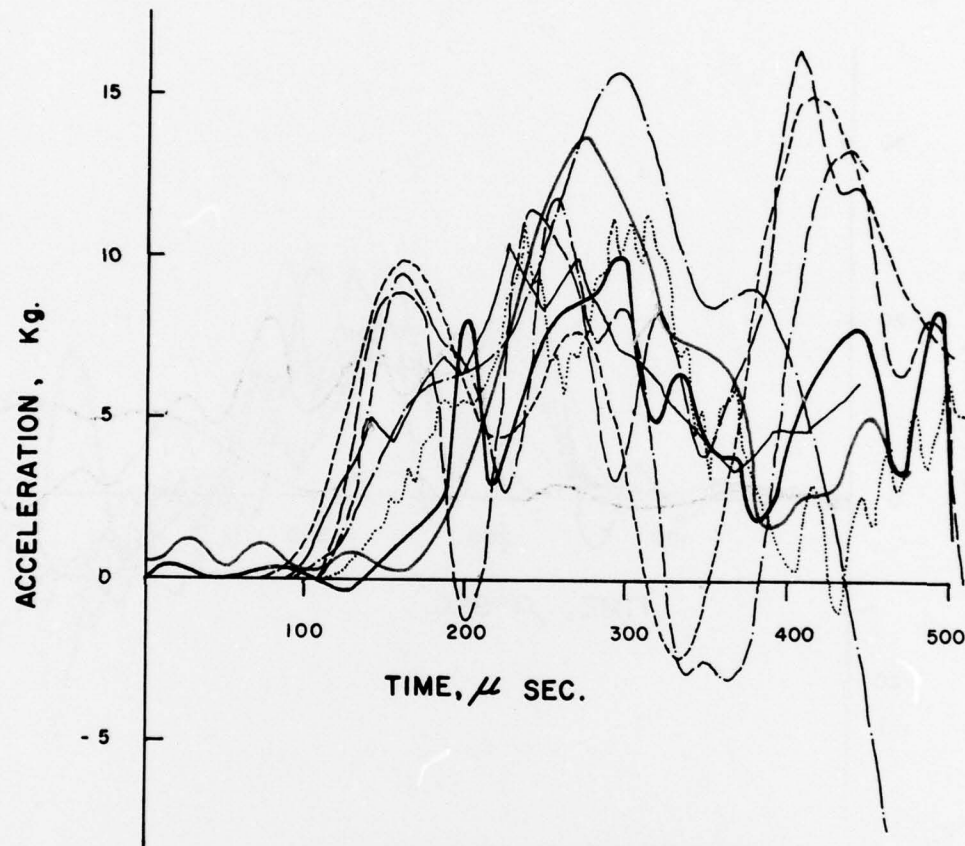
INSIDE SURFACE OF STL. CYL. RADIUS 1.15 IN.

COMPARISON OF THEORETICAL RESULTS WITH EXPERIMENTAL
TESTS 1 & 2 (0° AND 180°) AT STATION 27.3, HOOP

FIG. 60



* NO RESULTS FOR THIS LOCATION REPORTED



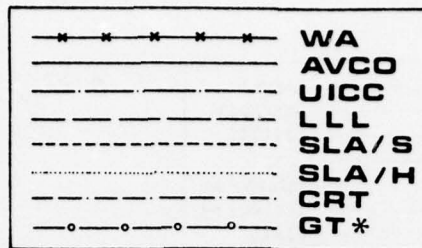
RADIUS 0.6 IN. ON STEEL BLOCK

TEST 1 ———

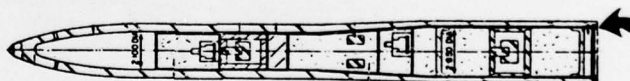
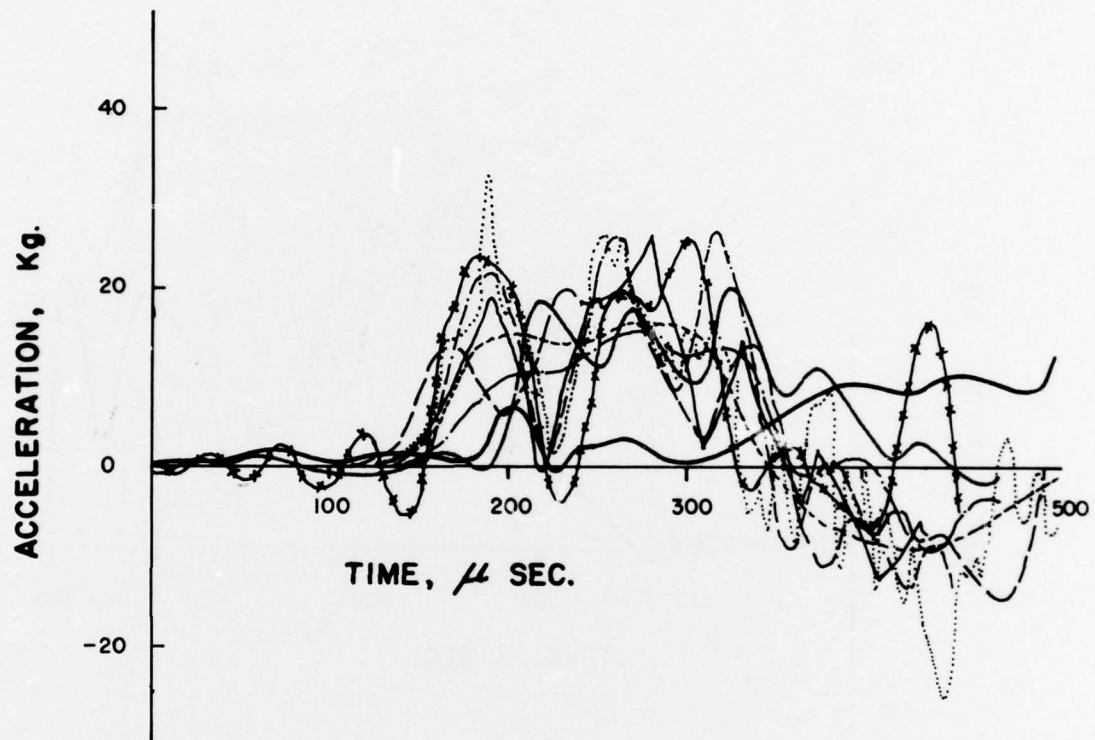
TEST 2 ———

COMPARISON OF THEORETICAL RESULTS WITH EXPERIMENTAL
TESTS 1 & 2 (90°) AT STATION 19.5 AXIAL - ACCEL.

FIG. 6I



* NO RESULTS FOR THIS LOCATION REPORTED

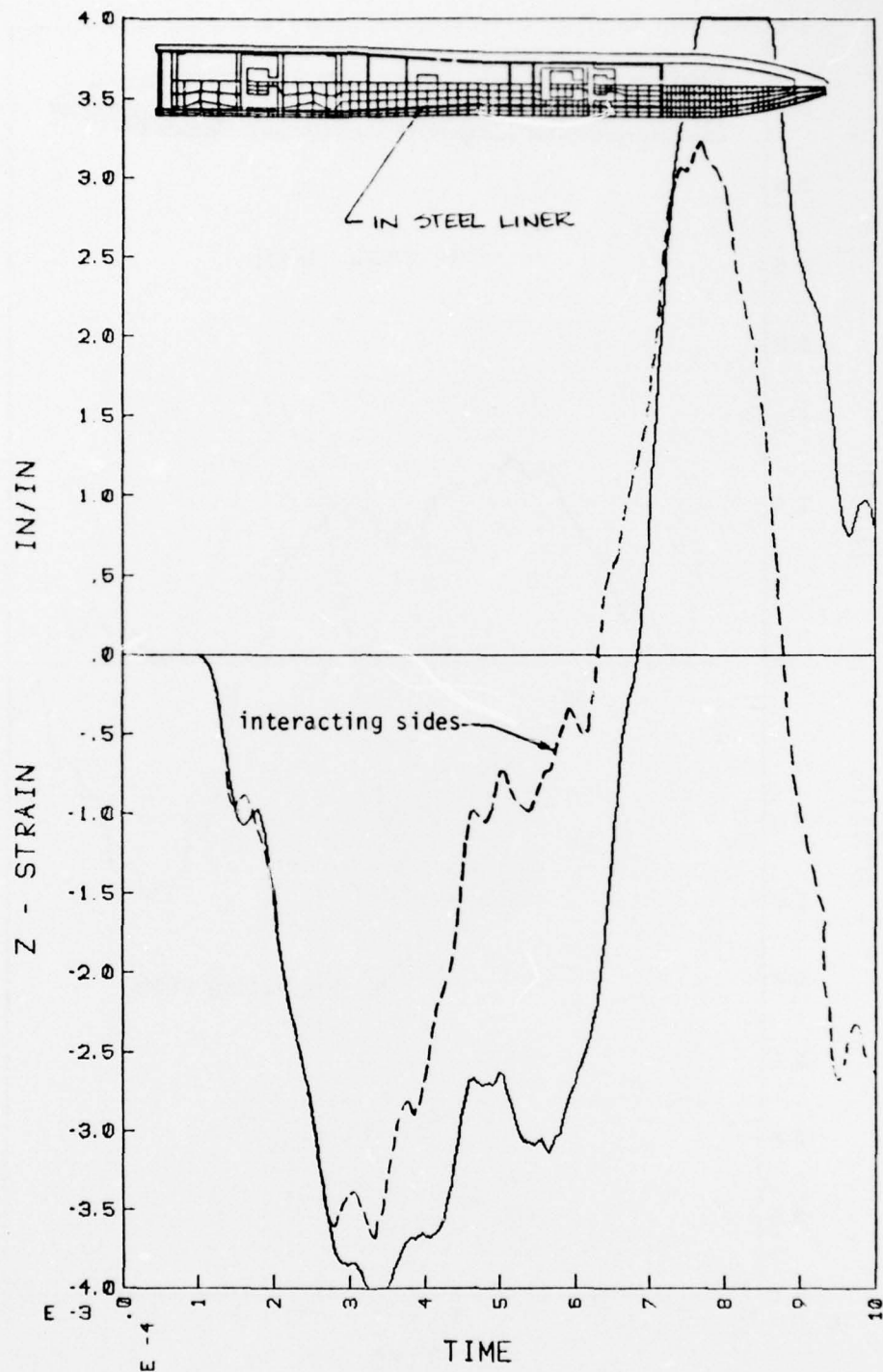


RADIUS 1.68 IN. AT OUTSIDE EDGE OF REAR OF CASE

TEST 1 —
TEST 2 —

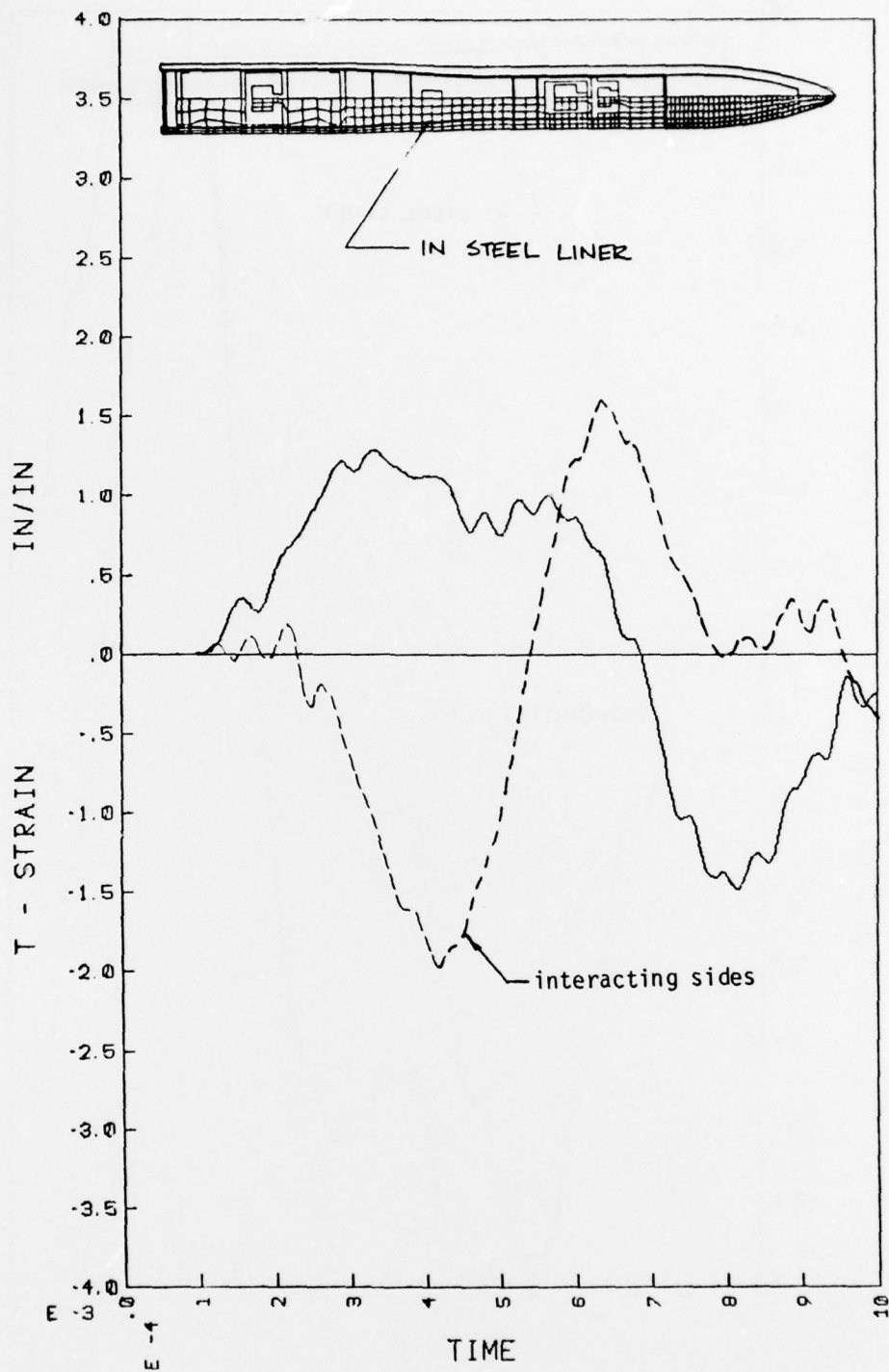
COMPARISON OF THEORETICAL RESULTS WITH EXPERIMENTAL
TEST 1 & 2 (0°) AT STATION 32, AXIAL - ACCEL.

FIG. 62



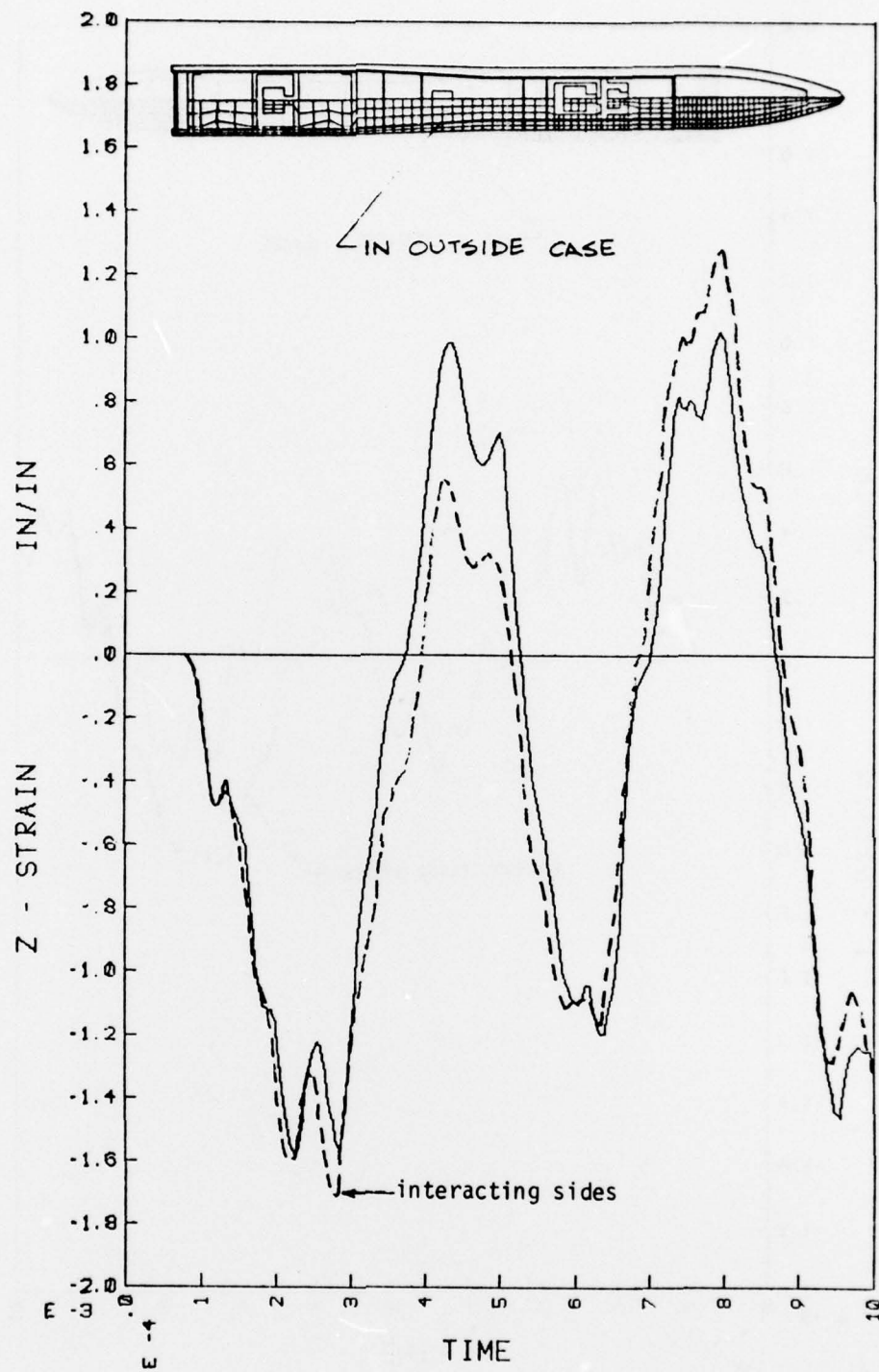
Axial strain in steel liner at Station 19.50
from LLL calculation

FIG. 63



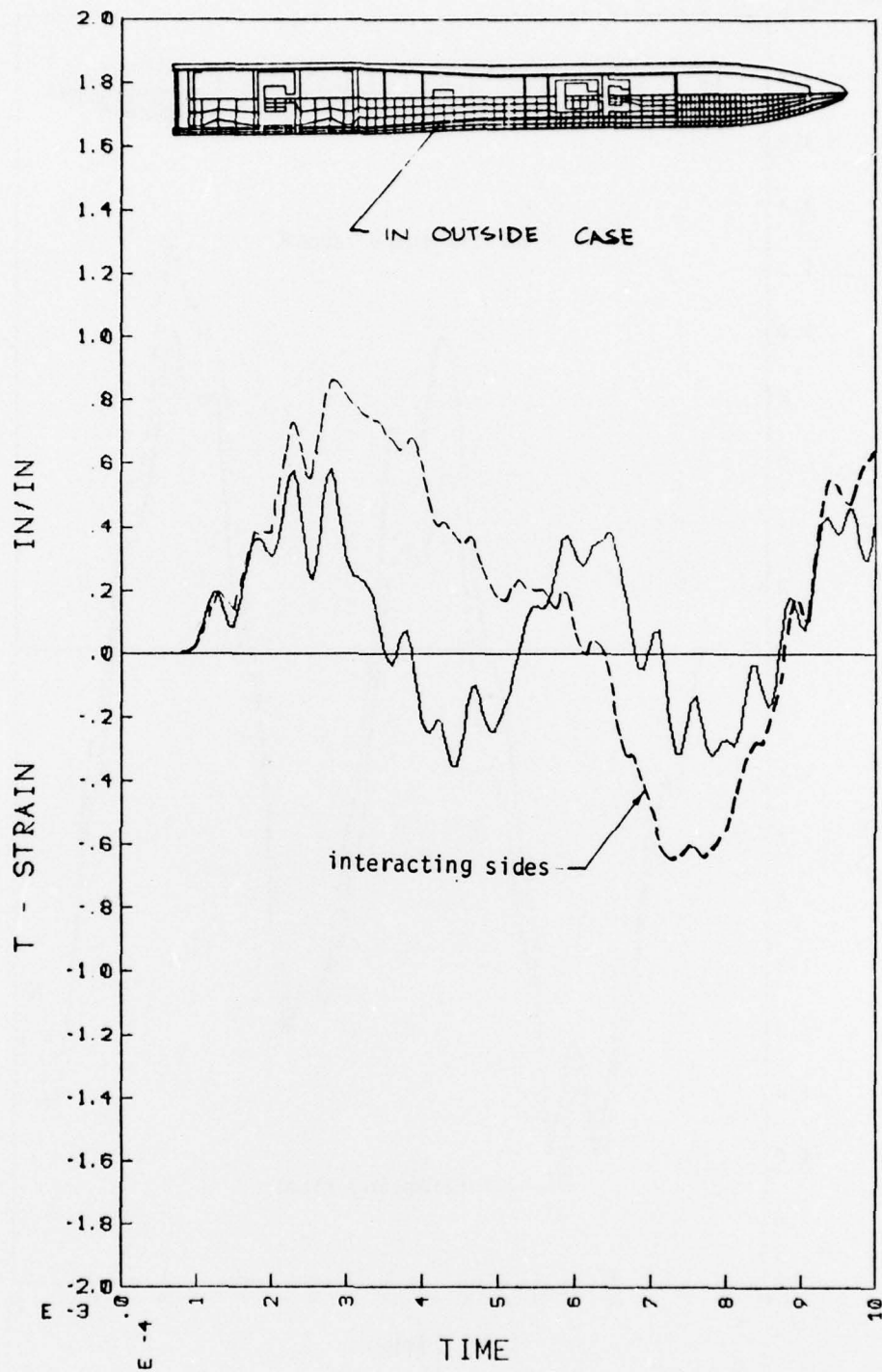
Hoop strain in steel liner at Station 19.50.

FIG. 64



Axial strain in steel case at Station 19.50

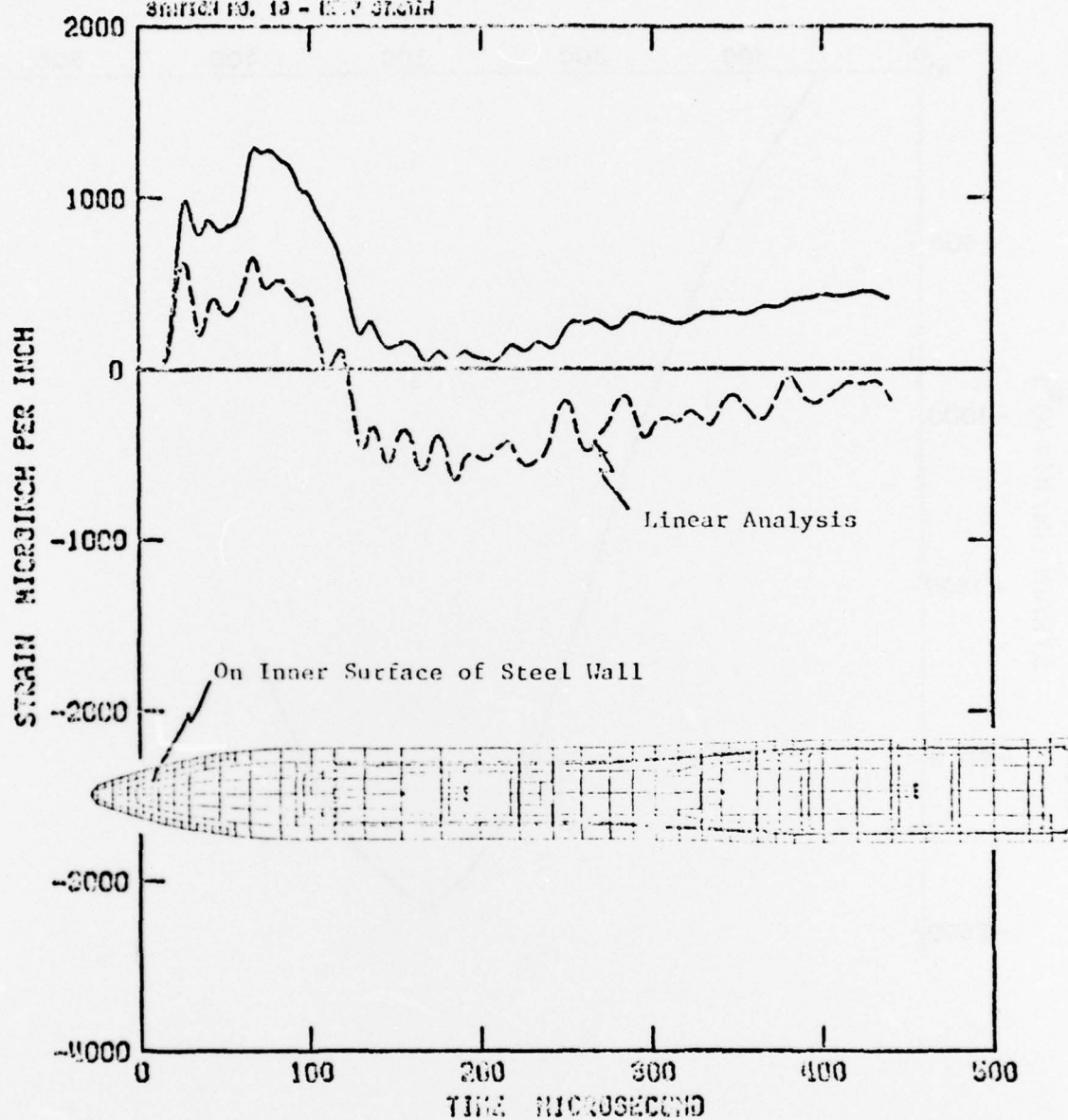
FIG. 65



Hoop strain in steel case at Station 19.50

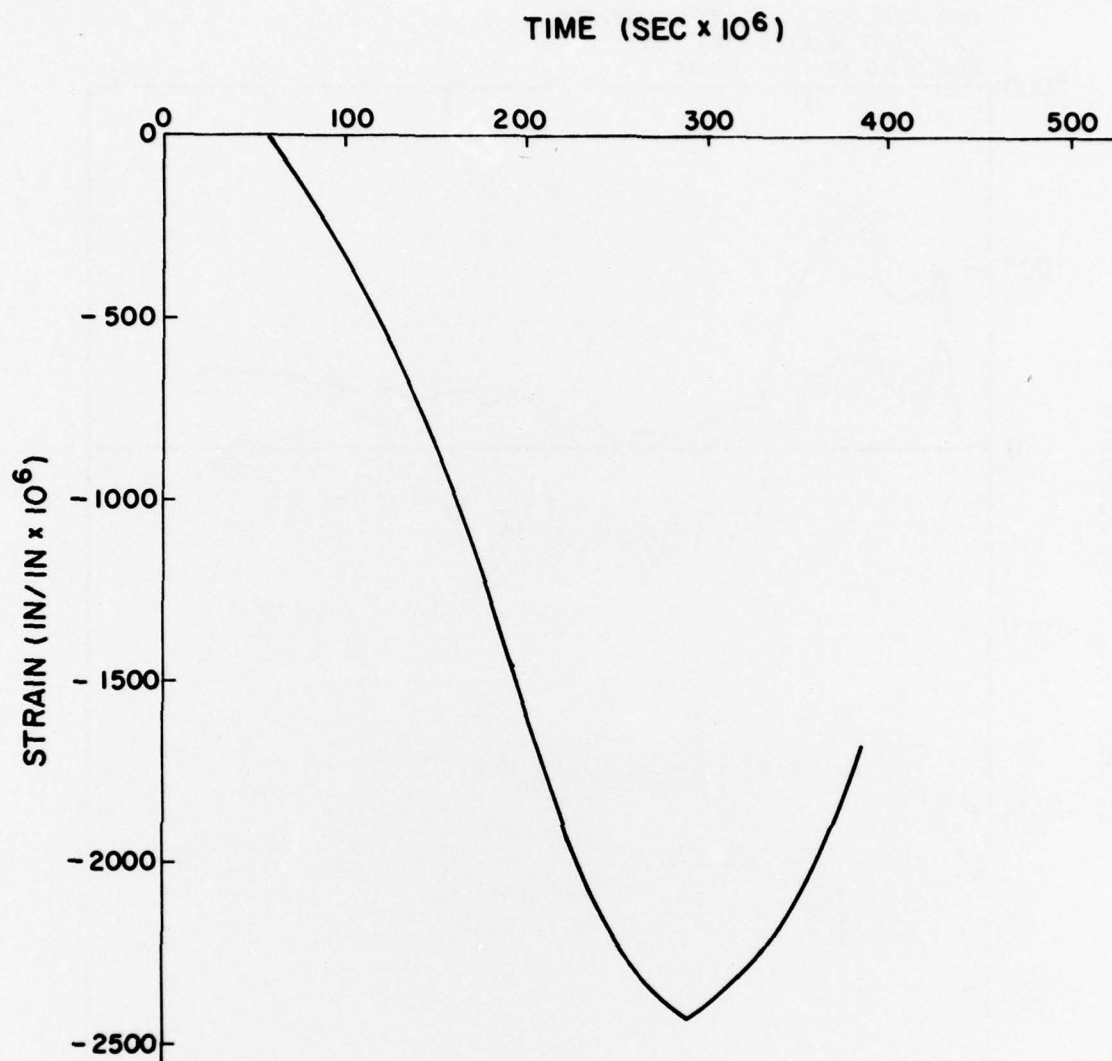
FIG. 66

CALIFORNIA RESEARCH AND TECHNOLOGY, INC.
 4055 BOULDER BLVD. FULLERTON, CALIF. 92631
 SECTION NO. 13 - IMP. STAIN



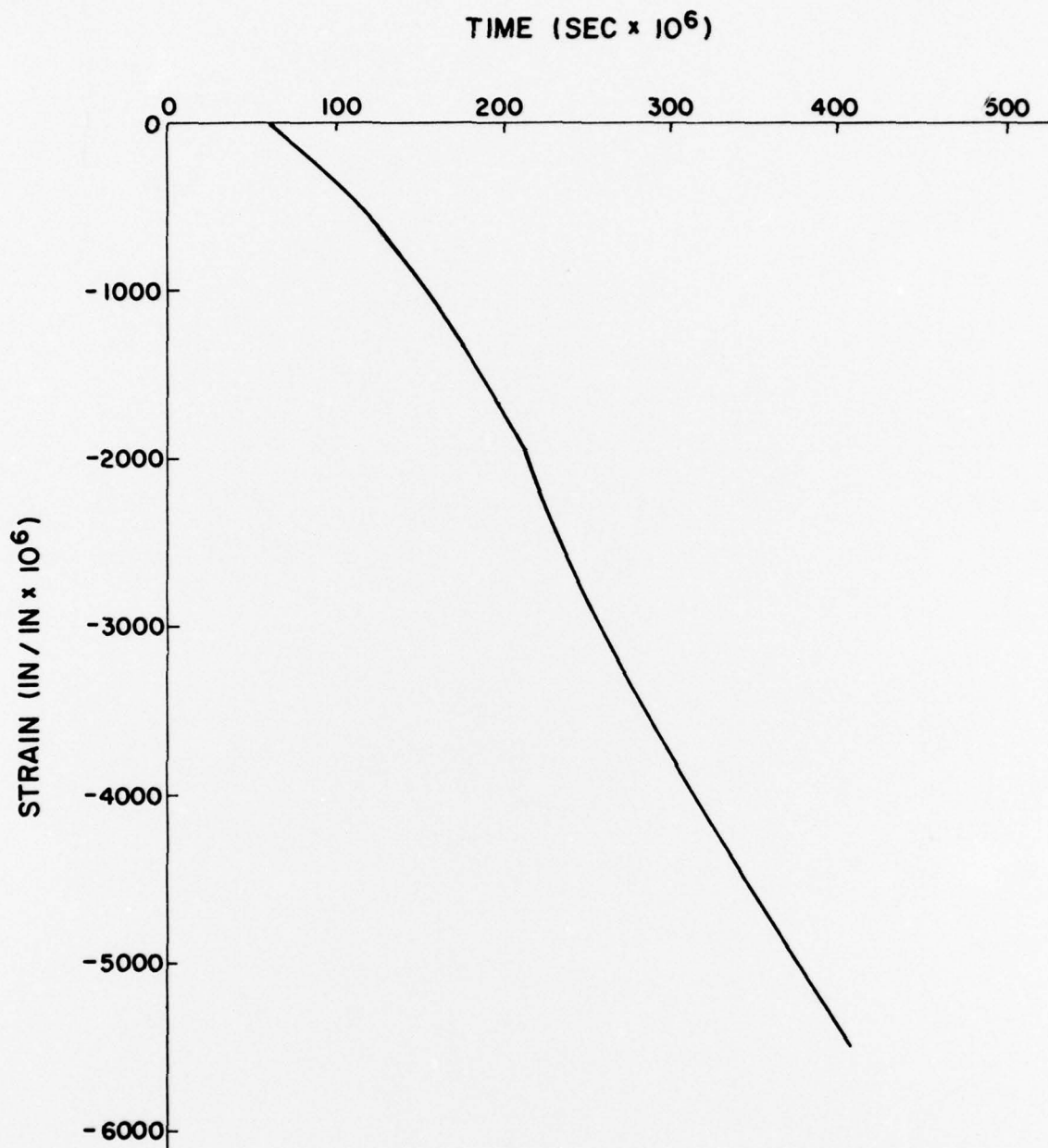
Results from CRT calculation

FIG. 67



AXIAL STRAIN AT STA. 9 OUTER SHELL

FIG. 68



STRAIN AT STA. 9 INNER LINER

FIG. 69

DISTRIBUTION LIST

DEPARTMENT OF DEFENSE

Director
Defense Advanced Rsch. Proj. Agency
ATTN: Tech. Lib.

Director
Defense Civil Preparedness Agency
Assistant Director for Research
ATTN: Admin. Officer

Defense Documentation Center
Cameron Station
12 cy ATTN: TC

Director
Defense Intelligence Agency
ATTN: Tech. Library
ATTN: DB-4C, Edward O'Farrell
ATTN: DT-2, Wpns. & Sys. Div.
ATTN: DI-7E
ATTN: Charles A. Fowler

Director
Defense Nuclear Agency
ATTN: SPAS
ATTN: TISI Archives
ATTN: DDST
3 cy ATTN: TITL, Tech. Library
5 cy ATTN: SPSS

Commander, Field Command
Defense Nuclear Agency
ATTN: FCPR

Director
Interservice Nuclear Weapons School
ATTN: Document Control

Director
Joint Strat. Tgt. Planning Staff
ATTN: STINFO Library

Chief
Livermore Division, Field Command, DNA
Lawrence Livermore Laboratory
ATTN: FCPRL

Under Secretary of Def. for Rsch. & Engrg.
ATTN: S&SS (OS)

DEPARTMENT OF THE ARMY

Dep. Chief of Staff for Rsch. Dev. & Acq.
ATTN: DAMA-CSM-N, LTC G. Ogden
ATTN: Tech. Library
ATTN: DAMA(CS), MAJ A. Gleim

Chief of Engineers
2 cy ATTN: DAEN-RDM
2 cy ATTN: DAEN-MCE-D

Deputy Chief of Staff for Ops. & Plans
ATTN: Tech. Lib.
ATTN: Dir. of Chem. & Nuc. Ops.

DEPARTMENT OF THE ARMY (Continued)

Chief
Engineer Strategic Studies Group
ATTN: DAEN-FES

Project Manager
Gator Mine Program
ATTN: E. J. Lindsey

Commander
Harry Diamond Laboratories
ATTN: DELHD-NP
ATTN: DELHD-RBH, James H. Gwaltney

Commander
Picatinny Arsenal
ATTN: Ray Moesner
ATTN: Tech. Lib.
ATTN: P. Angelloti
ATTN: Ernie Zimpo
ATTN: B. Shulman, DR-DAR-L-C-FA
ATTN: SMUPA-AD-D-A-7
ATTN: Paul Harris
ATTN: Jerry Pental
ATTN: SMUPA-AD-D-A
ATTN: SMUPA-AD-D-M
ATTN: Marty Margolin

Commander
Redstone Scientific Information Ctr.
U.S. Army Missile Command
ATTN: Chief, Documents

Commander
U.S. Army Armament Command
ATTN: Tech. Lib.

Director
U.S. Army Ballistic Research Labs.
ATTN: A. Ricchiazzi
ATTN: J. H. Keefer, DRDAR-BLE
ATTN: G. Grabarek
ATTN: J. W. Apgar
ATTN: G. Roecker
ATTN: DRXBR-TB
ATTN: DRXBR-X
2 cy ATTN: Tech. Lib., Edward Baicy

Commander and Director
U.S. Army Cold Region Res. Engr. Lab.
ATTN: G. Swinzow

Commander
U.S. Army Comb. Arms Combat Dev. Acty.
ATTN: LTC Pullen
ATTN: LTC G. Steger

Commander
U.S. Army Engineer Center
ATTN: ATSEN-SY-L

Division Engineer
U.S. Army Engineer Div., Huntsville
ATTN: HNDED-SR

DEPARTMENT OF THE ARMY (Continued)

Division Engineer
U.S. Army Engineer Div., Missouri Rvr.
ATTN: Tech. Lib.

Commandant
U.S. Army Engineer School
ATTN: ATSE-CTD-CS
ATTN: ATSE-TEA-AD

Director
U.S. Army Engr. Waterways Exper. Sta.
ATTN: Behzad Rohani
ATTN: John N. Strange
ATTN: D. K. Butler
ATTN: Guy Jackson
ATTN: William Flathau
ATTN: P. Hadala
ATTN: Leo Ingram
ATTN: Tech. Lib.

Commander
U.S. Army Mat. & Mechanics Rsch. Ctr.
ATTN: Tech. Lib.

Commander
U.S. Army Materiel Dev. & Readiness Cmd.
ATTN: Tech. Lib.

Director
U.S. Army Materiel Sys. Analysis Acty.
ATTN: Joseph Sperazza

Commander
U.S. Army Missile Command
ATTN: F. Fleming
ATTN: W. Jann

Commander
U.S. Army Mobility Equip. R&D Ctr.
ATTN: Tech. Lib.
ATTN: STSFB-XS
ATTN: STSFB-MW

Commander
U.S. Army Nuclear & Chemical Agency
ATTN: Library

Commander
U.S. Army Training and Doctrine Comd.
ATTN: LTC Auveduti, COL Enger
ATTN: LTC J. Foss

Commandant
U.S. Army War College
ATTN: Library

U.S. Army Mat. Cmd. Proj. Mngr. for Nuc. Munitions
ATTN: DRCPM-NUC

DEPARTMENT OF THE NAVY

Chief of Naval Operations
ATTN: Op-982, CAPT Toole
ATTN: Op-982, LCDR Smith
ATTN: Op-982, Lt Col Dubac
ATTN: Code 604C3, Robert Piacesi

Chief of Naval Research
ATTN: Tech. Library

DEPARTMENT OF THE NAVY (Continued)

Officer-in-Charge
Civil Engineering Laboratory
Naval Construction Battalion Center
ATTN: Tech. Lib.
ATTN: R. J. Odello

Commandant of the Marine Corps
ATTN: POM

Commanding General
Development Center
Fire Support Branch
ATTN: Capt Hartneady
ATTN: Lt Col Gapenski

Commander
Naval Air Systems Command Headquarters
ATTN: F. Marquardt

Commanding Officer
Naval Explosive Ord. Disposal Fac.
ATTN: Code 504, Jim Petrousky

Commander
Naval Facilities Engineering Command
Headquarters
ATTN: Tech. Lib.

Superintendent (Code 1424)
Naval Postgraduate School
ATTN: Code 2124, Tech. Rpts. Lib.

Director
Naval Research Laboratory
ATTN: Code 2600, Tech. Lib.

Commander
Naval Sea Systems Command
ATTN: ORD-033
ATTN: SEA-9931G

Officer-in-Charge
Naval Surface Weapons Center
ATTN: M. Kleinerman
ATTN: Code WA501, Navy Nuc. Prgms. Off.
ATTN: Code WX21, Tech. Lib.

Commander
Naval Surface Weapons Center
Dahlgren Laboratory
ATTN: Tech. Lib.

Commander
Naval Weapons Center
ATTN: Code 533, Tech. Lib.
ATTN: Carl Austin

Commanding Officer
Naval Weapons Evaluation Facility
ATTN: Tech. Lib.

Director
Strategic Systems Project Office
ATTN: NSP-43, Tech. Lib.

DEPARTMENT OF THE AIR FORCE

AF Institute of Technology, AU
ATTN: Library AFIT, Bldg. 640, Area B

DEPARTMENT OF THE AIR FORCE (Continued)

AF Armament Laboratory, AFSC
ATTN: Masey Valentine
3 cy ATTN: John Collins, AFATL/DLYV

AF Weapons Laboratory, AFSC
ATTN: SUL

Assistant Secretary of the Air Force
Research and Development
ATTN: Col R. E. Steere

Deputy Chief of Staff
Research and Development
ATTN: Col J. L. Gilbert

Commander
Foreign Technology Division, AFSC
ATTN: NICD Library

Hq. USAF/IN
ATTN: INATA

Hq. USAF/RD
ATTN: RDPM

Oklahoma State University
Fld. Off. for Wpns. Effectiveness
ATTN: Edward Jackett

Commander
Rome Air Development Center, AFSC
ATTN: EMILD, Doc. Library

SAMSO/RS
ATTN: RSS

DEPARTMENT OF ENERGY

Department of Energy
Albuquerque Operations Office
ATTN: Doc. Con. for Tech. Lib.

Department of Energy
Division of Headquarters Services
ATTN: Doc. Con. for Class. Tech. Lib.

Department of Energy
Nevada Operations Office
ATTN: Doc. Con. for Tech. Lib.

Division of Military Application
ATTN: Doc. Con. for Test Office

University of California
Lawrence Livermore Laboratory
ATTN: Mark Wilkins, L-504
ATTN: Tech. Info. Dept., L-3
ATTN: Jerry Goudreau

Los Alamos Scientific Laboratory
ATTN: Doc. Con. for Reports Lib.
ATTN: Doc. Con. for Tom Dowler

Sandia Laboratories
Livermore Laboratory
ATTN: Doc. Con. for Tech. Lib.

DEPARTMENT OF ENERGY (Continued)

Sandia Laboratories
ATTN: Doc. Con. for W. Altsmeirer
ATTN: Doc. Con. for William Patterson
ATTN: Doc. Con. for John Colp
ATTN: Doc. Con. for William Caudle
ATTN: Doc. Con. for 3142, Sandia Rpt. Coll.
ATTN: Doc. Con. for Walter Herrmann
ATTN: Doc. Con. for John Keizur

OTHER GOVERNMENT AGENCIES

NASA
Ames Research Center
ATTN: Robert W. Jackson

Office of Nuclear Reactor Regulation
Nuclear Regulatory Commission
ATTN: Lawrence Shad

DEPARTMENT OF DEFENSE CONTRACTORS

Aerospace Corporation
ATTN: Tech. Info. Services

Agbabian Associates
ATTN: M. Agbabian

Applied Theory, Inc.
2 cy ATTN: John G. Trulio

Avco Research & Systems Group
ATTN: David Henderson
ATTN: Research Lib., A830, Rm. 7201
ATTN: Pat Grady

Battelle Memorial Institute
ATTN: Tech. Lib.

The BDM Corporation
ATTN: Tech. Lib.

The Boeing Company
ATTN: Aerospace Library

California Research & Technology Inc.
ATTN: Ken Kreyenhagen
ATTN: Tech. Lib.

Civil/Nuclear Systems Corp.
ATTN: Robert Crawford

EG&G, Inc.
Albuquerque Division
ATTN: Tech. Lib.

Engineering Societies Library
ATTN: Ann Mott

General Dynamics Corp.
Pomona Division
ATTN: Keith Anderson

General Electric Company
TEMPO-Center for Advanced Studies
ATTN: DASAC

Georgia Institute of Technology
Georgia Tech Research Institute
ATTN: L. W. Rehfield
ATTN: S. V. Hanagud

DEPARTMENT OF DEFENSE CONTRACTORS (Continued)

Honeywell Incorporated
Defense Systems Division
ATTN: T. N. Helvig

Institute for Defense Analyses
ATTN: IDA Librarian, Ruth S. Smith

Kaman Avidyne
Division of Kaman Sciences Corp.
ATTN: Norman P. Hobbs
ATTN: E. S. Criscione
ATTN: Tech. Lib.

Kaman Sciences Corporation
ATTN: Library

Lockheed Missiles & Space Co., Inc.
ATTN: Tech. Library
ATTN: M. Culp

Lockheed Missiles & Space Co., Inc.
ATTN: Tech. Info. Ctr., D/Coll.

Martin Marietta Corporation
Orlando Division
ATTN: H. McQuaig
ATTN: M. Anthony
ATTN: Al Cowen

Merritt CASES, Inc.
ATTN: J. L. Merritt
ATTN: Tech. Lib.

University of New Mexico
Dept. of Campus Security & Police
ATTN: G. E. Triandafalidis

Nathan M. Newmark
Consulting Engineering Services
ATTN: W. Hall
ATTN: Nathan M. Newmark

Pacifica Technology
ATTN: G. Kent
ATTN: R. Bjork

Physics International Company
ATTN: Doc. Con. for Dennis Orphal
ATTN: Doc. Con. for Tech. Lib.
ATTN: Doc. Con. for Larry A. Behrmann

DEPARTMENT OF DEFENSE CONTRACTORS (Continued)

R&D Associates
ATTN: Henry Cooper
ATTN: Tech. Lib.
ATTN: Cyrus P. Knowles
ATTN: Harold L. Brode
ATTN: Paul Rausch
ATTN: Arlen Fields
ATTN: J. G. Lewis
ATTN: William B. Wright, Jr.

The Rand Corporation
ATTN: Tech. Lib.

Science Applications, Inc.
ATTN: Tech. Lib.

SRI International
ATTN: George R. Abrahamson
ATTN: Jim Colton

Systems, Science and Software, Inc.
ATTN: Robert Sedgewick
ATTN: Tech. Lib.
ATTN: Edward Gaffney

Terra Tek, Inc.
ATTN: Tech. Library

TRW Defense & Space Sys. Group
One Space Park
ATTN: Tech. Info. Center/S-1930
ATTN: Peter K. Dai, RI/2170

TRW Defense & Space Sys. Group
San Bernardino Operations
ATTN: E. Y. Wong, 527/712

Weidlinger Assoc. Consulting Engineers
ATTN: Melvin L. Baron
ATTN: J. M. McCormick

Weidlinger Assoc. Consulting Engineers
ATTN: J. Isenberg

ED
78